

**Post-filling Modeling  
of  
Vacuum Assisted Resin Transfer Molding  
Using  
Finite Element Method  
and  
Material Characterization Data**

**by  
Barış ÇAĞLAR**

**A Thesis Submitted to the  
Graduate School of Engineering  
in Partial Fulfillment of the Requirements for  
the Degree of**

**Master of Science  
in  
Mechanical Engineering**

**Koc University**

**August 2012**

Koc University  
Graduate School of Sciences and Engineering

This is to certify that I have examined this copy of a master's thesis by

Bariř Çaęlar

and have found that it is complete and satisfactory in all respects,  
and that any and all revisions required by the final  
examining committee have been made.

Committee Members:

---

E. Murat Sözer, Ph. D.

---

Demircan Canadıncı, Ph. D.

---

Rıza Kızılel, Ph. D.

Date:

29.08.2012

---

## ABSTRACT

Large composite parts are produced using Vacuum Assisted Resin Transfer Molding (VARTM) process; however, the major challenge in VARTM is to fill the mold completely with acceptable dimensional tolerances in the part. Simulation codes based on Darcy law are commonly used for flow modeling in Resin Transfer Molding (RTM) in which the thickness and permeability are fixed, i.e., do not vary with time. However, both thickness and permeability vary spatially and with time in VARTM due to the flexible vacuum bag used as the upper mold part. VARTM simulation codes should be incorporated with compaction models by coupling flow and fiber compaction. This also allows the simulation of post-filling stage of VARTM, where control actions are performed to exit the excess resin and minimize the variation in the part thickness.

The present study models the post-filling stage of VARTM using experimental material characterization data for permeability and compaction. Continuity equation is solved using Finite Element Method (FEM) with triangular elements. The coupled distributions of pressure, thickness and permeability are calculated at the end of complete mold filling by using an iterative scheme. The solution is validated with several case studies such as single inlet single exit boundary conditions resulting in a 1D flow, and inlet/exit combinations resulting in 2D flow. Global mass conservation is used for validating the solution algorithm by comparing inlet and exit flow rates.

Post-filling stage following a boundary condition update is simulated by starting from the simulated results of the end-of-mold-filling stage; and then applying the change in the boundary condition. The coupled distributions of pressure, thickness and permeability are calculated by using an explicit Eulerian time integration; and the stability of algorithm is ensured by modifying the time step size.

Modeling of mold-filling and verifying the simulations with experiments remain as future work.

## ÖZET

Büyük kompozit parçalar *Vakum Destekli Reçine Transfer Kalıplama* (VARTM) yöntemiyle üretilmektedir; ancak bu üretim yönteminde en sık karşılaşılan zorluklar ortaya çıkan üründe kabul edilebilir boyutsal toleransların elde edilememesi ve kalıbın boşluk kalmayacak şekilde doldurulamamasıdır. Kalınlık ve geçirgenliğin zamanla değişmediği *Reçine Transfer Kalıplama* (RTM) yönteminin akış modellemesi genellikle *Darcy Yasası* temelli simülasyon programlarıyla yapılır. VARTM yönteminde ise, üst kalıp esnek bir vakum torbası olduğu için; hem kalınlık hem de geçirgenlik zamana ve pozisyona bağlı olarak değişkenlik gösterir. Sıkıştırma modelleriyle birleştirilmiş VARTM simülasyon programları, fazla reçinenin kalıptan çıkarıldığı ve kalınlık farkının azaltıldığı kontrol aksiyonlarının yapıldığı dolun sonrası aşamaları modelleme açısından önemlidir.

Bu çalışmada, VARTM üretim yönteminin dolun sonrası aşaması; deneysel geçirgenlik ve kalınlık malzeme karakterizasyonu verileriyle modellenmiştir. Süreklilik denklemi *Sonlu Elemanlar Yöntemi*'nde (FEM) üçgen elemanlar kullanılarak çözülmüştür. Basınç, kalınlık ve geçirgenliğin kalıbın dolun anındaki *bağlaşık* dağılımları ardışık yaklaşımlar yoluyla çözülmüştür. Çözüm yöntemi, tek giriş ve tek çıkışın olduğu tek boyutlu akış örnekleri ve farklı giriş/çıkış kombinasyonlarının oluşturduğu iki boyutlu akış örnekleriyle doğrulanmıştır. Toplam kütle korunumu, giriş ve çıkıştaki akış miktarları karşılaştırılarak çözüm algoritmasının doğrulanması için kullanılmıştır.

Sınır koşullarındaki değişikliğin sebep olduğu dolun sonrası aşamanın simülasyonu, kalıbın dolun anındaki çözümün sonuçlarından başlayarak ve sınır koşullarındaki değişikliği bu sonuçlara uygulayarak yapılmıştır. Basınç, kalınlık, ve geçirgenliğin *bağlaşık* dağılımlarının zamanla değişimi *belirtik* bir yöntem kullanılarak çözülmüştür ve çözüm yönteminin kararlılığı zaman adımının büyüklüğü değiştirilerek sağlanmıştır.

Kalıp dolununun modellenmesi ve simülasyon sonuçlarının deneylerle karşılaştırılması gelecek çalışmalarda ele alınacaktır.

## ACKNOWLEDGEMENTS

I would like to thank Dr. E. Murat Sözer, my advisor, for his encouragement and wisdom. His guidance helped me many times throughout the years I have been a proud member of Composite Materials Manufacturing Laboratory (CMML). Alongside these, I am thankful to him for his endless support throughout my project and writing process.

I owe sincere and earnest thankfulness to other members of my thesis committee, Dr. Rıza Kızılel and Dr. Demircan Canadıncı for their critical reading and invaluable comments. I am thankful to Dr. Demircan Canadıncı also for his detailed and constructive advices.

I would like to thank TUBITAK (The Scientific and Technical Research Council of Turkey) for providing the funding which allowed me to undertake this research at Koc University, Istanbul, Turkey.

I must express my gratitude to Bekir Yenilmez for his support at each and every stage of this project. I wish to thank other members of CMML, Akif Yalçınkaya, Talha Akyol, Mustafa Habođlu and Ayşen Sariođlu for having the honor of working and spending time with them.

I would like to express my sincere gratitude to my father Ferhat, my mother Ruhan, my sisters Dilek and Nuran and my brother Hasan for their eternal and unequivocal love and support. Their respect and patience have always inspired me.

Completing this work would have been all the more difficult without the support and friendship of many, including Berkay Yarpuzlu, Arda Aytekin, Mehmet Ayyıldız, Berkay Gümüş, Utku Boz, Engin Çukurođlu, Güray Kuzu, Enis Sert, Mehmet Ali Yatbaz, Yusuf Sahilliođlu and many others.

# Table of Contents

ABSTRACT .....	iii
ÖZET .....	iv
ACKNOWLEDGEMENTS.....	v
List of Figures.....	viii
List of Tables.....	x
NOMENCLATURE.....	xi
Chapter 1 INTRODUCTION .....	1
1.1 Vacuum Assisted Resin Transfer Molding (VARTM) .....	1
1.2 Compaction Characterization.....	3
1.3 Process Modeling of VARTM.....	4
1.4 Permeability Characterization.....	6
1.5 Method of Process Modeling .....	7
1.6 Contribution of this thesis .....	8
Chapter 2 FINITE ELEMENT METHOD .....	10
2.1 Linear Triangular Elements.....	10
2.2 Galerkin's Weighted Residual Method .....	13
Chapter 3 SIMULATIONS OF VARTM.....	15
3.1 Overview .....	15
3.2 Solution at the end of mold-filling for constant thickness and permeability .....	18
3.2.1 Case 1-a: 1D flow.....	18
3.2.2 Case 1-b: 2D flow.....	39
3.3 Solution at the end of mold-filling for constant thickness and variable permeability.....	41
3.3.1 Case 2-a: 1D flow.....	41
3.3.2 Case 2-b: 2D flow.....	50
3.4 Solution for variable thickness and variable permeability .....	52
3.4.1 Case 3-a: Solution at the end of mold-filling.....	52
3.4.2 Case 3-b: Evolution of solution with time due to change in boundary conditions.....	59
3.4.3 Case 3-c: Steady state solution for new boundary conditions .....	71

Chapter 4 SUMMARY AND CONCLUSIONS .....	73
BIBLIOGRAPHY .....	75
VITA .....	77
APPENDIX A Thickness and Permeability Distributions for Studied Cases .....	78
APPENDIX B MATLAB Code for Solution of Steady Cases .....	85
APPENDIX C MATLAB Code for Evolution of Solution with Time .....	89

## List of Figures

Figure 2.1 Typical triangular element.....	11
Figure 3.1 Dimensions of a typical part used for simulations.....	20
Figure 3.2 Global boundary conditions for the part.....	20
Figure 3.3 Unit normal vector of a triangular element at global boundary.....	23
Figure 3.4 Triangular element with convective boundary condition.....	27
Figure 3.5 Three elements with different convective boundaries.....	27
Figure 3.6 Convective boundary condition at the edge of an element.....	29
Figure 3.7 Four separate elements in the domain.....	30
Figure 3.8 The domain with mesh generated using initmesh function.....	32
Figure 3.9 Refined random triangular elements.....	33
Figure 3.10 Regular triangular elements.....	33
Figure 3.11 Pressure distribution in the mold.....	35
Figure 3.12 Pressure distribution along $y = 0.05$ m.....	36
Figure 3.13 Velocity field in the mold.....	39
Figure 3.14 Global boundary conditions for the part.....	40
Figure 3.15 Pressure distribution in the mold.....	40
Figure 3.16 Velocity field in the mold.....	41
Figure 3.17 Permeability distribution inside a triangular element.....	43
Figure 3.18 Global boundary conditions for the part.....	44
Figure 3.19 Pressure distribution in the mold.....	44
Figure 3.20 Pressure distribution along $y = 0.05$ m.....	45
Figure 3.21 Pressure distribution along $y = 0.05$ m.....	48
Figure 3.22 Effect of number of elements on flow rate.....	49
Figure 3.23 Effect of number of elements on error in pressure.....	49
Figure 3.24 Velocity field in the mold.....	50
Figure 3.25 Differential equation and global boundary conditions for the part.....	51
Figure 3.26 Pressure distribution in the mold.....	51
Figure 3.27 Velocity field in the mold.....	52
Figure 3.28 Global boundary conditions for the part.....	57



Figure 3.29 Pressure distribution in the mold .....	58
Figure 3.30 Velocity field in the mold.....	59
Figure 3.31 Global boundary conditions for the part.....	60
Figure 3.32 Pressure distribution at different instants .....	66
Figure 3.33 Pressure distribution at different instants from another angle.....	66
Figure 3.34 Pressure distribution in the mold at $t = 1200$ s.....	67
Figure 3.35 Positions of A, B, C, and D points.....	67
Figure 3.36 Evolution of pressure at A, B, C, and D points.....	68
Figure 3.37 Change of volume in and out of the mold by using 300 elements.....	69
Figure 3.38 Change of total volume by using 300 elements .....	70
Figure 3.39 Percentage error by using 300, 600, and 1200 elements .....	70
<b>Figure 3.40</b> Pressure distribution in the mold.....	72

## List of Tables

Table 3.1 Material data and boundary conditions in Case 1 .....	15
Table 3.2 Material data and boundary conditions in Case 2 .....	16
Table 3.3 Material data and boundary conditions in Case 3 .....	17

## NOMENCLATURE

$V_f$	fiber volume fraction	$\sigma(V_f)$	stress on fabric
$V_a$	theoretical maximum fiber volume fraction	$V_0$	fiber volume fraction at zero compaction pressure
$A_s$	spring constant	$k$	softening coefficient
$E$	fiber stiffness	$\rho$	density of fluid
$\vec{u}$	velocity vector	$f$	generation of mass per unit volume per unit time
$u, v, w$	velocity components	$\mu$	viscosity of liquid resin
$[K]$	permeability tensor of porous medium	$K_{xx}, K_{yy}$	permeability in principal directions
$P_i, P_j, P_k$	pressure at nodes of an element	$A$	area of the triangular element
$\alpha_i, \alpha_j, \alpha_k$	coefficients of linear triangular element	$S_i, S_j, S_k$	linear interpolation functions of the triangular element
$\beta_i, \beta_j, \beta_k$	coefficients of linear triangular element	$P^{(e)}(x, y)$	pressure in an element
$\delta_i, \delta_j, \delta_k$	coefficients of linear triangular element	$\phi(x, y)$	dependent field variable
$\Omega$	domain of problem	$\Gamma$	boundary of the domain
$\phi'$	approximation of field variable	$m$	total number of nodes
$R$	residual	$W_i$	weighting function
$h$	thickness	$P$	pressure
$L_x, L_y, L_z$	dimensions of the mold [m]	$P_c$	compaction pressure
$t$	time	$t_{fill}$	time at the end of mold-filling
$P_{inj}$	pressure at injection port [Pa]	$P_{vent}$	pressure at ventilation port
$\vec{n}$	unit normal vector to the boundary	$n_x, n_y$	components of unit normal vector
$C^{(e)}$	stiffness matrix of element	$[C]$	global stiffness matrix

$l_{ij}, l_{jk}, l_{ki}$	length of the edges of the triangular element	$q$	flux per unit volume per unit volume
$Q_{inj}$	flow rate at injection port	$Q_{vent}$	flow rate at exit port
$w, h$	width and height of the mold	$\{P\}$	column vector of nodal pressures
$\{F\}$	column vector of nodal flows (load vector)	$P_n$	nodal pressures at $n^{th}$ iteration
$K^{(e)}$	permeability at the centroid of the element	$[\dot{C}]$	global capacitance matrix
$\{\dot{P}\}$	column vector of time derivatives of nodal pressures	$\Delta t$	time step size
$\lambda_i$	eigenvalues of the system	$\{\Phi\}_i$	eigenvectors of the system
$V_{mold}$	volume of resin in the mold	$V_{out}$	volume of resin leaving the mold
$V_{tot}$	total volume of resin		

# Chapter 1

## INTRODUCTION

### 1.1 Vacuum Assisted Resin Transfer Molding (VARTM)

Liquid Composite Molding (LCM) is a class of composite material manufacturing processes. In these processes, fiber preform is placed in the mold cavity and it is saturated with resin flow induced by pressure difference between injection and ventilation ports. Mostly, a thermoset resin is preferred in these processes due to its low viscosity when compared to viscosity of thermoplastic resins. Impregnation with high viscosity resins requires high pressure and thus high investment cost in equipment, so use of high viscosity resins in LCM is limited. One other reason why thermoplastics are not used in LCM is that, even if high pressure is achieved with a robust injection machine, it causes fiber wash (movement of the fibers in the mold cavity). Resin Transfer Molding (RTM) and Vacuum Assisted Resin Transfer Molding (VARTM) are the two common LCM processes. VARTM is also known as Vacuum Infusion (VI) in the literature. In this study, a major issue (thickness variation) in VARTM will be investigated by using a process model based on conservation of mass within a control volume, and by solving it using Finite Element Method (FEM). Below, a brief descriptions of RTM and VARTM will be given. Modeling issues of VARTM, such as permeability and compaction are also studied later in this thesis.

In RTM, both sides of the mold are rigid, and the mold is closed after fabric is placed in the mold cavity. Resin is pressurized in an injection machine, and it is injected into the mold. It is crucial to fill the mold cavity completely before resin gelation; otherwise the extreme increase in resin viscosity will cause very high pressures. The part is demolded after it cures (partially or completely), i.e., after it toughens enough not to warp during or after the demolding.

VARTM is a modification of RTM process. In VARTM, layers of glass or carbon fabric are placed on a lower mold. Instead of using a rigid upper mold part as in RTM, a plastic film is used in VARTM. Sealing between upper and lower mold parts is ensured by using a sealant tape (which is called tacky tape). A vacuum pump is connected to the mold through one or more ventilation ports; and the resin is provided to the system through one or more injection ports. In RTM positive pressure difference; in VARTM vacuum pressure difference between ventilation and injection ports drives the resin through the empty spaces between the fibers of the preform.

VARTM is usually preferred for medium to large sized parts. Instead of machining a metallic upper mold part with low dimensional tolerances in RTM, using vacuum bag in VARTM decreases the initial investment cost significantly. On the other hand, pressure difference between injection and ventilation ports cannot exceed one atmospheric pressure, and this limits the flow rate and thus reduces the production rate in VARTM. Positions of injection and ventilation ports have to be designed ensuring that the part is completely wetted with resin. For complex part geometries, this task gets very challenging, not only for the nominal conditions, but also considering the variations in the material (fabric cutting, stacking and placement).

Two major challenges in VARTM are (1) to fill the mold cavity completely within a reasonable time that allows mass production rate; and (2) to keep the dimensional tolerances within acceptable tolerances depending on where the part is used. The former issue requires to model resin flow which is usually done using simulation codes based on Darcy law which is an empirical relation between the resin velocity and pressure gradient. The latter issue requires modeling the fabric compaction by relating the compaction pressure and the part thickness. Especially in VARTM, considering the control actions that are taken during and after the filling stage, one needs to couple the resin flow and fabric compaction. In this thesis, the distributions of pressure, thickness and permeability will be

solved at the end of the mold filling; and then the effect of post-filling control actions will be studied.

Thickness varies spatially and with time during infusion, and this variation is attributed to the following three main reasons in [1]

- change of compaction pressure originating from the change in resin pressure,
- fiber relaxation with time despite constant compaction pressure,
- equalization of resin pressure during resin bleeding (closing the gates and keeping the vents active under vacuum pressure).

## 1.2 Compaction Characterization

Characterization of compaction behavior has been studied and modeled by researchers with the aim of controlling the thickness variation in the part. Most of these are elastic models which assume that the fabric responds instantaneously when the compaction pressure changes. One of the mostly recognized elastic models is suggested by Gutowski et al. [2]. Relationship between compaction pressure and fiber volume fraction is modeled as follows

$$\sigma(V_f) = A_s \frac{\sqrt{\frac{V_f}{V_0} - 1}}{\left(\sqrt{\frac{V_a}{V_f} - 1}\right)^4} \quad (1.1)$$

where  $\sigma(V_f)$  is the stress on fabric in [Pa],  $V_f$  is the fiber volume fraction,  $V_a$  is the available fiber volume fraction (i.e., theoretical maximum fiber volume fraction),  $V_0$  is fiber volume fraction at zero compaction pressure, and  $A_s$  is the spring constant in [Pa]. Andersson et al. [3] modeled the compaction behavior using experimental results for dry and wetted fabrics as follows

$$\sigma(V_f) = kE(V_f^m - (V_{f_0} + \kappa)^m) \quad (1.2)$$

where  $k$  is the softening coefficient,  $E$  is fiber stiffness,  $\kappa$  and  $m$  are constants to be determined by curve-fitting the experimental data. Robitaille and Gauvin [4] and Joubaud et al. [5] used power law to relate the compaction pressure and fiber volume fraction as follows

$$V_f = a\sigma^b \quad (1.3)$$

where  $a$  and  $b$  are constants to be determined by curve-fitting the experimental data.

In elastic models, change of thickness in the fabric is as assumed to be instantaneous when compaction pressure changes. As shown in the experiments of [1], creep (i.e., change of strain or thickness with time) occurs at a constant compaction pressure. But, elastic compaction models cannot model this time-dependent response. There are various viscoelastic compaction models which account the time-dependent behavior of compaction response in the fabric. Some of these viscoelastic models are presented in [6, 7]. As demonstrated in [1], viscoelastic behavior becomes significant especially if compaction pressure drops below 40 kPa. Also, Govignon et al. [8] suggested that use of elastic modeling reduces the complexity of mechanical coupling between fiber volume fraction and compaction pressure.

### **1.3 Process Modeling of VARTM**

One major disadvantage of VARTM is that the process is labor-dependent, and an inconsistent material preparation may cause deviation of the flow propagation and thus incomplete mold filling. This causes serious loss of time and money. Competitive circumstances in manufacturing also require short production cycles with minimum cost. Thus, combining mathematical process models and simulation codes is important for meeting the demands of competitive industries while keeping the scrap at minimum.



In this work; (a) pressure distribution at the instant of mold filling ( $t = t_{\text{fill}}$ ), and (b) evolution of pressure distribution following a control action (modification at injection and/or ventilation pressures) are solved. In both cases, continuity equation must be satisfied. Continuity equation is

$$\frac{\partial \rho}{\partial t} + \nabla \cdot (\rho \vec{u}) = f \quad (1.4)$$

where  $\rho$  is density of fluid,  $\vec{u}$  is velocity vector and  $f$  is the generation of mass per unit volume per unit time. In both cases, there is no mass generation or mass loss, i.e.,  $f = 0$ ; hence Equation (1.4) takes the following form

$$\frac{\partial \rho}{\partial t} + \nabla \cdot (\rho \vec{u}) = 0 \quad (1.5)$$

Darcy's law describes the flow through a porous medium as follows:

$$\begin{Bmatrix} u \\ v \\ w \end{Bmatrix} = -\frac{1}{\mu} \begin{bmatrix} K_{xx} & K_{xy} & K_{xz} \\ K_{yx} & K_{yy} & K_{yz} \\ K_{zx} & K_{zy} & K_{zz} \end{bmatrix} \begin{Bmatrix} \partial P / \partial x \\ \partial P / \partial y \\ \partial P / \partial z \end{Bmatrix} \quad (1.6)$$

where,  $u$ ,  $v$ , and  $w$  are velocity components,  $\mu$  is the viscosity of liquid resin,  $[K]$  is the permeability tensor of porous medium. Darcy's law is used relating the velocity of resin and pressure gradient. It replaces the conservation of momentum equations, since use of conservation of momentum equations requires the determination of flow channels between fibers. The determination of channels is troublesome for a typical fabric preform used in LCM due to its complicated fiber structure; so use of Darcy's law instead of conservation of momentum equations reduces the complexity of modeling while estimating the macro flow in the porous medium.

Velocity vector in Equation (1.6) has three components, which corresponds to flow of resin in three principal axes. In most applications (parts with much smaller thickness than the in-plane dimensions), flow through thickness direction is negligible when compared to other two directions, and the flow is modeled as two-dimensional. For two-dimensional flow, Darcy's law can be re-written as

$$\begin{Bmatrix} u \\ v \end{Bmatrix} = -\frac{1}{\mu} \begin{bmatrix} K_{xx} & K_{xy} \\ K_{yx} & K_{yy} \end{bmatrix} \begin{Bmatrix} \partial P / \partial x \\ \partial P / \partial y \end{Bmatrix} \quad (1.7)$$

#### 1.4 Permeability Characterization

The goals of the LCM processes are to manufacture parts in short production cycles, and having end products with good quality. Mechanical properties (such as specific strength, stiffness and toughness) of composites usually determine the part quality. These properties increase as the fiber volume fraction increases by compacting the preform [9]. On the other hand, increasing fiber volume fraction means reducing the size of channels through which resin flows, and decreases permeability. So, increasing the fiber volume fraction leads to longer fill times and longer production cycles. The trade-off between mechanical properties and production times is crucial in production planning. To achieve these goals, one needs to understand and model the resin flow, which requires a reliable permeability data. Many researchers have addressed this issue, and either modeled or measured the permeability of fabrics.

One of the most renowned permeability models is known as Kozeny-Carman equation [10]. It models the permeability along the flow direction as follows

$$K = A \frac{(1 - V_f)^3}{V_f^2} \quad (1.8)$$

where  $V_f$  is the fiber volume fraction and  $A$  is an empirical constant. There are other constitutive models in the literature which also relate the permeability of the fabric to fiber volume fraction [11, 12]. Most of these constitutive equations contain empirical coefficients. These constitutive equations may fail to model permeability at high fiber volume fractions.

In experimental characterization of permeability, either change of injection pressure is monitored under constant flow rate boundary condition, or position of flow front is monitored under constant pressure boundary condition. One-dimensional, radial (two-dimensional) or three-dimensional experiments are performed [13, 14].

### **1.5 Method of Process Modeling**

In our research group, characterization of permeability [15] and compaction [1, 13, 16-18] were studied. Process control experiments are also being conducted using the results of compaction and permeability characterization databases [19-21]. A process model is needed for the process control and for planning control actions prior to experiments in complex geometries.

In the literature, Finite Difference Method (FDM) is preferred to solve partial differential equations (PDE) if the domain geometry is simple. In FDM, one replaces derivative terms in differential equations or boundary conditions with finite difference equations (forward, central, or backward differences) resulting in a set of linear equations. Difficulty of modeling with FDM arises when discontinuities are present in the problem [22]. One of the most common discontinuities in LCM process models is due to the variation in material properties such as permeability or thickness. For example, permeability and thickness of a region with additional stiffening material are considerably different than the rest of the fabric, and modeling the sudden change of permeability and/or thickness is troublesome in FDM.

Another difficulty while modeling with FDM arises when non-rectangular geometries are considered [22-24]. In discretization of domain, nodes are used and these nodes should be distributed regularly in FDM for ease. However, for non-rectangular domains, either a jagged boundary needs to be generated which will deviate from the actual shape of the edge, or use of non-uniformly distributed nodes will require using complicated finite difference equations at the boundary.

In FEM, governing equations are the same for all elements. Once the domain is discretized, all the elements are treated the same. Formulation of FEM is more laborious compared to FDM; but it is independent of geometry, so it is preferred for modeling of complex geometries.

Simacek et al. [25] used FDM to solve post-filling stage in VARTM after modifying boundary conditions; and thus to study settling of pressure and thickness distributions. Simulations were performed for rectangular mold geometry with lineal injection and ventilation ports which are placed at opposite sides of the mold. The flow is 1D due to the symmetry of injection and ventilation ports. The initial conditions of pressure and thickness distributions at the beginning of post-filling (i.e., the steady state of the mold filling stage) were directly taken from an experimental data. Differently here in this study, those distributions will also be solved using FEM.

## **1.6 Contribution of this thesis**

The major objective of this study is to model the post-filling stage of VARTM by using material characterization data (permeability and compaction) that were previously constructed in our research group. Before achieving that goal, meaning the post-filling modeling, initially FEM is used to solve the pressure distribution at the end of the mold filling. This is done by considering different case studies. The case studies include single inlet and single exit with geometric symmetry (resulting in a 1D flow) and also complicated inlet and exit conditions resulting in different 2D flows. The accuracy of the

FEM results is investigated by considering global mass conservation in all cases. Pressure distribution and flow rates at injection and ventilation ports are compared with analytical solutions in some cases.

In the second part of the thesis, post-filling modeling of VARTM is studied. To model the post-filling of VARTM, material characterization data (compaction and permeability) of the fabric preform are needed. In [18], an elastic model was used to determine the compaction behavior of a fabric preform which was also used in this study. The elastic model was fit to tens of experiments for the same fabric type and this solution was used as compaction model in this study. In [15], permeability of different fabric types (including the fabric type in [18]) was characterized by performing steady and unsteady experiments at various thicknesses. By using the compaction relationship in [18] and permeability results in [15], the following steps will be taken:

1. The steady pressure distribution at the end of the mold filling stage will be calculated in Sections 3.2 and 3.3 for two different case studies.
2. The adjustments in boundary conditions (which are called control actions) will be modeled by evolving the thickness, permeability and pressure distributions with time. Evolution with time is achieved by explicit finite difference equations in time.
3. The result of the unsteady case (item 2) will be validated by solving the steady distributions corresponding to the boundary condition set used in item 2, and comparing the two results. The correctness of the solution algorithm is validated if the convergence of the unsteady solution (in item 2) matches the result of steady state solution (in this item 3).

## **Chapter 2**

# **FINITE ELEMENT METHOD**

### **2.1 Linear Triangular Elements**

First, in order to solve a differential equation using Finite Element Method (FEM), one should discretize the domain of the problem. Discretization is achieved through generating a mesh over the domain with one or more type of elements. Dimensionality (1D, 2D or 3D) of the problem domain determines the element types. For a one dimensional problem, one can use rod elements with linear, quadratic, or cubic approximation functions inside the element. For two dimensional problems, one can use triangular or quadrilateral elements with linear, quadratic or higher order approximation functions.

Rectangular elements do not conform to curved geometries well when compared to triangular elements [26]. Geometries of the problems in this thesis are two dimensional and flat. Thus, rectangular elements could have been used here; however, triangular elements are used in this thesis to have the ability to work with curved boundaries of future work. Linear approximation functions are used for defining the distribution of properties within the elements (linear triangular elements).

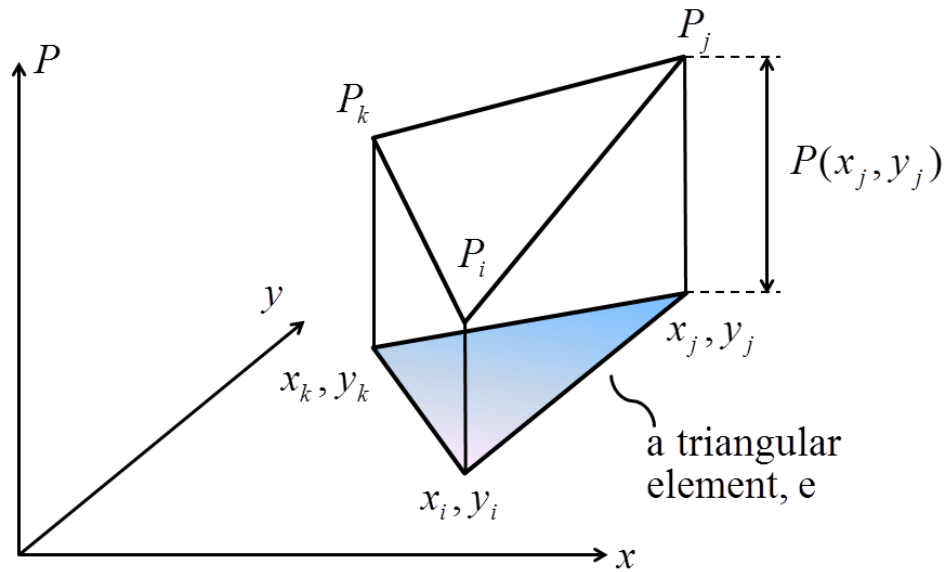


**Figure 2.1** Typical triangular element

Figure 2.1 shows a typical triangular element. The element has three non-collinear nodes. The distribution of the dependent variable (it is pressure,  $P$ , in this study) in a linear triangular element can be approximated as in [27]

$$P^{(e)}(x, y) = a + bx + cy \quad (2.1)$$

where  $a$ ,  $b$ , and  $c$  are constants explained below,  $x$  and  $y$  are the global coordinates. Using Equation (2.1), nodal pressure values are expressed as follows:

$$P_i = a + bx_i + cy_i \quad (2.2)$$

$$P_j = a + bx_j + cy_j \quad (2.3)$$

$$P_k = a + bx_k + cy_k \quad (2.4)$$

From Equations (2.2)-(2.4) one can calculate  $a$ ,  $b$ , and  $c$  as described in [28]

$$a = \frac{1}{2A} [(x_j y_k - x_k y_j)P_i + (x_k y_i - x_i y_k)P_j + (x_i y_j - x_j y_i)P_k] \quad (2.5)$$

$$b = \frac{1}{2A} [(y_j - y_k)P_i + (y_k - y_i)P_j + (y_i - y_j)P_k] \quad (2.6)$$

$$c = \frac{1}{2A} [(x_k - x_j)P_i + (x_i - x_k)P_j + (x_j - x_i)P_k] \quad (2.7)$$

where  $A$  is the area of the triangular element and it is calculated as follows

$$2A = [(y_j - y_k)x_i + (y_k - y_i)x_j + (y_i - y_j)x_k] = 2 \begin{vmatrix} 1 & x_i & y_i \\ 1 & x_j & y_j \\ 1 & x_k & y_k \end{vmatrix}$$

or

$$A = \frac{[(y_j - y_k)x_i + (y_k - y_i)x_j + (y_i - y_j)x_k]}{2} = \begin{vmatrix} 1 & x_i & y_i \\ 1 & x_j & y_j \\ 1 & x_k & y_k \end{vmatrix} \quad (2.8)$$

Substituting  $a$ ,  $b$ , and  $c$  terms in Equations (2.5) - (2.7) into Equation (2.1) and grouping  $P_i$ ,  $P_j$ , and  $P_k$  terms in matrix form yields

$$P^{(e)} = [S_i S_j S_k] \begin{Bmatrix} P_i \\ P_j \\ P_k \end{Bmatrix} \quad (2.9)$$

where  $S_n$  defined as follows



$$S_n = \frac{\alpha_n + \beta_n x + \delta_n y}{2A} \quad \text{for } n = i, j, k$$

(2.10)

and

$$\begin{aligned} \alpha_i &= x_j y_k - x_k y_j & \beta_i &= y_j - y_k & \delta_i &= x_k - x_j \\ \alpha_j &= x_k y_i - x_i y_k & \beta_j &= y_k - y_i & \delta_j &= x_i - x_k \\ \alpha_k &= x_i y_j - x_j y_i & \beta_k &= y_i - y_j & \delta_k &= x_j - x_i \end{aligned} \quad (2.11)$$

## 2.2 Galerkin's Weighted Residual Method

In general, weighted residual methods are based on finding an approximate solution for the governing ordinary or partial differential equations. The approximate solution must satisfy the differential equation as well as the boundary conditions of the given problem. Since the solution is approximate, not exact, substitution of the solution will introduce an error which is also called residual. The aim in the weighted residual methods is to minimize the error introduced by the approximation of solution.

A typical two-dimensional differential equation to be solved by using weighted residual method is given in below

$$A(\phi) - f = 0 \quad (2.12)$$

where  $A$  is a differential operator,  $\phi(x, y)$  is the dependent field variable to be calculated approximately, and  $f(x, y)$  is a given function of independent variables  $x$  and  $y$ .  $\phi$  is defined over a domain  $\Omega$  and this domain is surrounded by the boundary  $\Gamma$ . Boundary  $\Gamma$  conforms to the given boundary conditions of the problem. Approximation of  $\phi$  is represented as  $\phi'$ .  $\phi'$  is a function of independent variables, and it is approximated as

$$\phi \approx \phi' = \sum_1^m S_i C_i \quad (2.13)$$

where  $S_i$  is the linear interpolation function and  $C_i$  is the unknown function of independent variables for the  $i^{\text{th}}$  node.  $m$  is the total number of nodes in the domain, and both  $S_i$  and  $C_i$  are defined for all nodes in the domain. Substituting Equation (2.13) into Equation (2.12) yields

$$A(\phi') - f \equiv R \neq 0 \quad (2.14)$$

where  $R$  is the residual resulted by approximation of the field variable. Weighted residual methods seek to determine the unknown  $C_i$  in such a way that the residual  $R$  is minimized. The minimization is achieved through a weighted summation of residuals over the domain. Hence,  $m$  linearly independent weighting functions are selected to yield

$$\int_{\Omega} [A(\phi') - f] W_i d\Omega = \int_{\Omega} R W_i d\Omega = 0 \quad (2.15)$$

where  $i = 1, 2, \dots, m$ .

There are many possible weighting functions that can be used in this error minimization process. Commonly used weighted residual method is Galerkin's Method. In this method, weighting functions are chosen to be equal to the interpolation functions (see Equation (2.10)) of the elements,  $W_i = S_i$ . Galerkin's Method will be used for error minimization throughout this thesis meaning that interpolation functions of triangular elements,  $S_i$ , will be used as the weighting functions which are calculated using Equations (2.10) and (2.11).

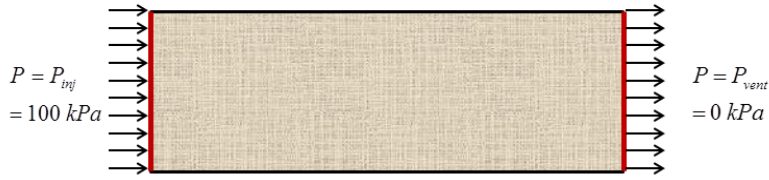
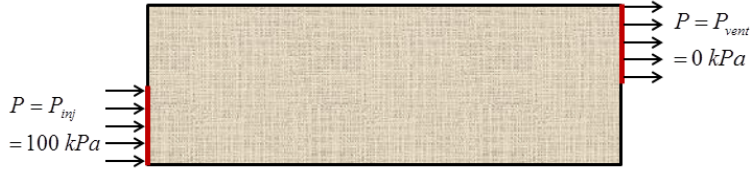
## Chapter 3

### SIMULATIONS OF VARTM

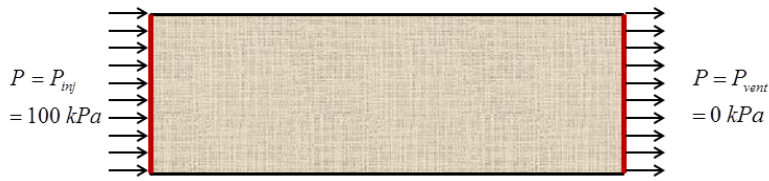
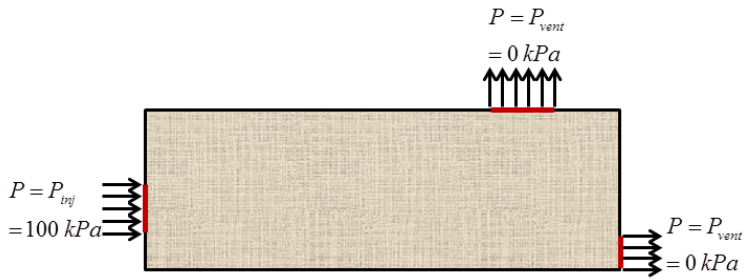
#### 3.1 Overview

In this part of the thesis, simulations are performed for different material properties and for different boundary conditions. Tables 3.1, 3.2 and 3.3 show the boundary conditions and material characterization data for Case 1, Case 2 and Case 3, respectively. Numerical methods of Finite Element Method are implemented using the algorithms described in [28, 29]. The first two cases are studied to validate the correctness of the solution algorithm by comparing the numerical results with analytical solutions available. Then in the third case, the evolution of process variables ( $h$ ,  $K$  and  $P$ ) will be investigated for 1D and 2D flow cases.

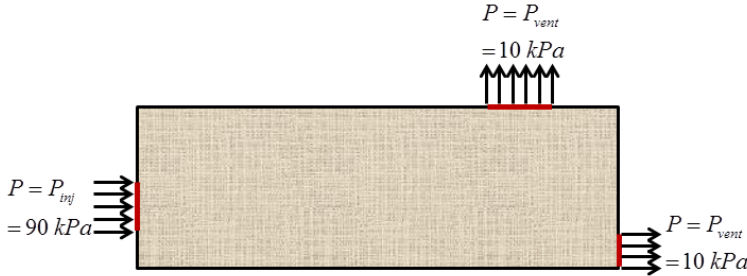
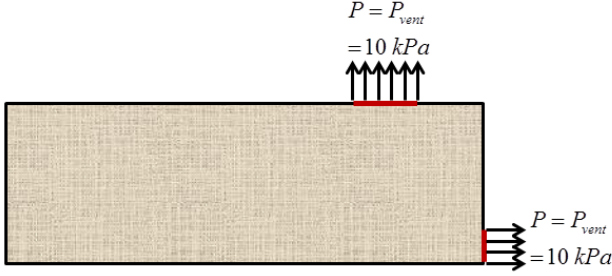
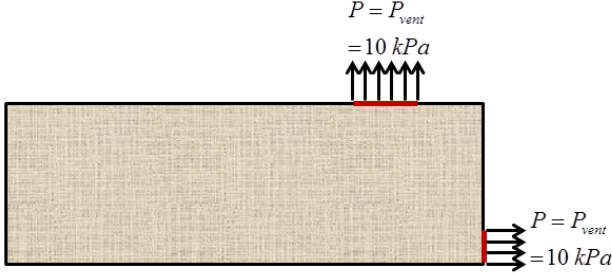
**Table 3.1** Material data and boundary conditions in Case 1

	$L_x = 0.3(m), L_y = 0.1(m), h = 0.003(m), K = 1 \times 10^{-9}(m^2)$
Case #	Boundary Conditions
Case 1-a	 <p style="text-align: center;"> <math>P = P_{inj}</math>  <math>= 100 \text{ kPa}</math> </p> <p style="text-align: center;"> <math>P = P_{vent}</math>  <math>= 0 \text{ kPa}</math> </p>
Case 1-b	 <p style="text-align: center;"> <math>P = P_{inj}</math>  <math>= 100 \text{ kPa}</math> </p> <p style="text-align: center;"> <math>P = P_{vent}</math>  <math>= 0 \text{ kPa}</math> </p>

**Table 3.2** Material data and boundary conditions in Case 2

$L_x = 0.3(m), L_y = 0.1(m), h = 0.003(m), K = 5 \times 10^{-10} - 15 \times 10^{-10} x(m^2)$	
Case #	Boundary Conditions
Case 2-a	 <p>Diagram for Case 2-a: A rectangular material is shown with a textured surface. On the left vertical face, there are eight horizontal arrows pointing to the right, labeled <math>P = P_{inj} = 100 \text{ kPa}</math>. On the right vertical face, there are eight horizontal arrows pointing to the left, labeled <math>P = P_{vent} = 0 \text{ kPa}</math>.</p>
Case 2-b	 <p>Diagram for Case 2-b: A rectangular material is shown with a textured surface. On the left vertical face, there are five horizontal arrows pointing to the right, labeled <math>P = P_{inj} = 100 \text{ kPa}</math>. On the right vertical face, there are five horizontal arrows pointing to the left, labeled <math>P = P_{vent} = 0 \text{ kPa}</math>. On the top horizontal face, there are five vertical arrows pointing upwards, labeled <math>P = P_{vent} = 0 \text{ kPa}</math>.</p>

**Table 3.3** Material data and boundary conditions in Case 3

Case #	Boundary Conditions
Case 3-a	$L_x = 0.3(m), L_y = 0.1(m), V_f = \frac{1}{19.42} \ln\left(\frac{P_c}{2.04}\right), h = \frac{(8)(0.450)}{2540V_f}, K = 5 \times 10^{-10} - 15 \times 10^{-10} x(m^2)$ 
Case 3-b <sup>1</sup> (Evolution of variables with time)	
Case 3-c (Steady state solution)	

<sup>1</sup> The initial conditions of process variables ( $h$ ,  $K$ , and  $P$ ) in Case 3-b are taken from Case 3-a. Upon applying the sudden changes at the boundary (closing the inlet on the left edge), the evolutions of the variables are tracked until a convergence is achieved. This solution is then compared with the solution of Case 3-c.

### 3.2 Solution at the end of mold-filling for constant thickness and permeability

#### 3.2.1 Case 1-a: 1D flow

Here, the solution of pressure distribution in a mold will be studied by using FEM. In order to simulate the pressure distribution at the instant of mold filling, one should solve the continuity equation

$$\frac{\partial \rho}{\partial t} + \nabla \cdot (\rho \vec{u}) = f \quad (3.1)$$

where  $\rho$  is density of fluid,  $\vec{u}$  is velocity vector and  $f$  is the source term which corresponds to the generation of mass per unit volume per unit time. There is no mass generation in this case, so the right-hand side of the equation is set to zero

$$\frac{\partial \rho}{\partial t} + \nabla \cdot (\rho \vec{u}) = 0 \quad (3.2)$$

Fluid is incompressible, so  $\rho$  is constant and does not change with time. Thus, dropping  $\partial \rho / \partial t$  term from Equation (3.2), it takes the following form:

$$\nabla \cdot (\rho \vec{u}) = 0 \quad (3.3)$$

Since  $\rho$  is constant and right-hand side of Equation (3.3) is zero, one can drop  $\rho$  term as well

$$\nabla \cdot (\vec{u}) = 0 \quad (3.4)$$

Darcy's law is an empirical equation describing the flow through porous medium, and it replaces the momentum equation

$$\begin{Bmatrix} u \\ v \end{Bmatrix} = -\frac{1}{\mu} \begin{bmatrix} K_{xx} & K_{xy} \\ K_{yx} & K_{yy} \end{bmatrix} \begin{Bmatrix} \partial P / \partial x \\ \partial P / \partial y \end{Bmatrix} \quad (3.5)$$

Where  $\mu$  is the viscosity of liquid resin,  $[K]$  is the permeability tensor of porous medium, and  $P(x, y)$  is the pressure distribution at the end of mold filling ( $t = t_{fill}$ ). In this study, the principal axes are  $x$  and  $y$  so that

$$K_{xy} = K_{yx} = 0 \quad (3.6)$$

We will consider isotropic fabrics such as random fabrics, so that

$$K_{xx} = K_{yy} \equiv K \quad (3.7)$$

Curing of the resin is out of the scope of this work, so viscosity,  $\mu$ , is assumed to be constant throughout this work. Combining Equations (3.4) and (3.5) yields

$$\begin{aligned} -\frac{K}{\mu} \nabla^2 P &= -\frac{K}{\mu} \left( \frac{\partial^2 P}{\partial x^2} + \frac{\partial^2 P}{\partial y^2} \right) = 0 \\ \text{or} & \\ \frac{K}{\mu} \nabla^2 P &= \frac{K}{\mu} \left( \frac{\partial^2 P}{\partial x^2} + \frac{\partial^2 P}{\partial y^2} \right) = 0 \end{aligned} \quad (3.8)$$

for uniform  $K$  (i.e.  $K \neq K(x, y)$ ). Figure 3.1 shows the dimensions of a typical mold used for the simulation of this study. Figure 3.2 shows all the boundary conditions for the boundaries and governing differential equation for interior of the mold. In this case,  $P_{inj} = 100 \text{ kPa} = 100000 \text{ Pa}$  and  $P_{vent} = 0$ .

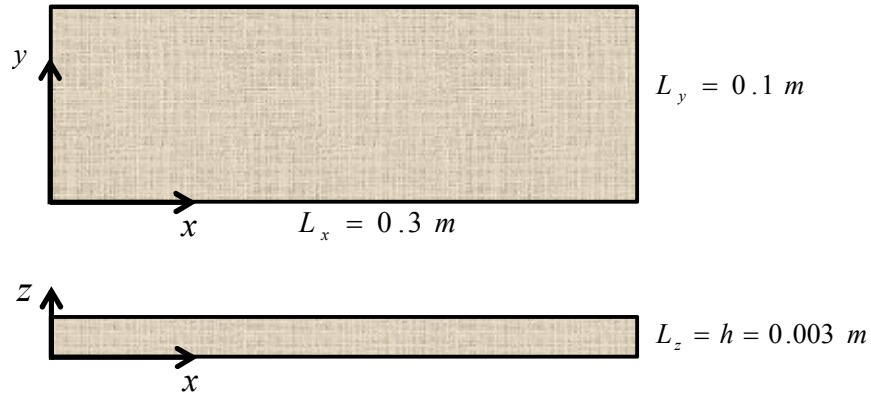


**Figure 3.1** Dimensions of a typical part used for simulations

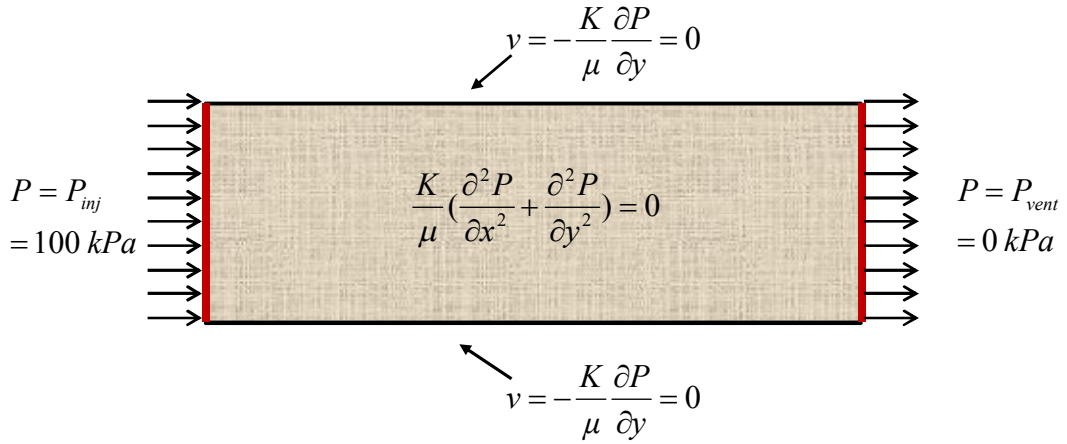


**Figure 3.2** Global boundary conditions for the part

Applying Galerkin's Residual Method, Equation (3.8) takes the following form

$$\int_{\Omega} W_i \left[ \frac{K}{\mu} \nabla^2 P^{(e)} \right] d\Omega = \int_{\Omega} W_i \left[ \frac{K}{\mu} \left( \frac{\partial^2 P^{(e)}}{\partial x^2} + \frac{\partial^2 P^{(e)}}{\partial y^2} \right) \right] d\Omega = 0 \quad (3.9)$$

where domain  $\Omega$  is divided into triangular elements; and pressure distribution inside each element can be written as



$$P^{(e)}(x, y) = P^{(e)} = \sum_1^r S_i(x, y)P_i = [S_i S_j S_k] \begin{Bmatrix} P_i \\ P_j \\ P_k \end{Bmatrix} = [S] \{P\}^{(e)} \quad (3.10)$$

where  $r$  is the number of nodes assigned to that element,  $e$ .

In Section 2.2, approximation of  $\phi(x, y)$ , a dependent field variable, was explained.  $\phi'$  is used for approximation of the field variable  $\phi$ . In this study, approximate solution of pressure distribution,  $P$  is sought.  $P^{(e)}$  is used throughout this study as the approximation of  $P$ , pressure distribution inside an element. In other words,  $P^{(e)}$  term is analogous to the approximation of  $\phi'$  in Equation (2.13).

$$\iint_{\Omega^{(e)}} S_i \left[ \frac{K}{\mu} \left( \frac{\partial^2 P^{(e)}}{\partial x^2} + \frac{\partial^2 P^{(e)}}{\partial y^2} \right) \right] dx dy = 0 \quad (3.11)$$

Equation (3.11) shows the governing equation inside an element where  $W_i = S_i$  as discussed in Section 2.2 and it can be written for other interpolation functions,  $S_j$  and  $S_k$  namely. Combining the three equations, and writing them in compact matrix form, it results in

$$\iint_{\Omega^{(e)}} [S]^T \left[ \frac{K}{\mu} \left( \frac{\partial^2 P^{(e)}}{\partial x^2} + \frac{\partial^2 P^{(e)}}{\partial y^2} \right) \right] dx dy = 0 \quad (3.12)$$

where the transpose of the interpolation functions is given as

$$[S]^T = \begin{Bmatrix} S_i \\ S_j \\ S_k \end{Bmatrix} \quad (3.13)$$

$P^{(e)}$  is first order as discussed in Section 2.1.  $\partial^2 P^{(e)}/\partial x^2$  and  $\partial^2 P^{(e)}/\partial y^2$  are equal to zero since both terms are second derivatives of a linear function. Solving Equation (3.12) does not give a fruitful result, because the second derivatives of linear functions give the redundant result of  $0 = 0$ . To get a meaningful result, second order terms need to be manipulated, and manipulation is achieved through integration by parts as follows:

$$\frac{\partial}{\partial x} \left( [S]^T \frac{\partial P^{(e)}}{\partial x} \right) = [S]^T \frac{\partial^2 P^{(e)}}{\partial x^2} + \frac{\partial [S]^T}{\partial x} \frac{\partial P^{(e)}}{\partial x} \quad (3.14)$$

$$\frac{\partial}{\partial y} \left( [S]^T \frac{\partial P^{(e)}}{\partial y} \right) = [S]^T \frac{\partial^2 P^{(e)}}{\partial y^2} + \frac{\partial [S]^T}{\partial y} \frac{\partial P^{(e)}}{\partial y} \quad (3.15)$$

which can be re-written as

$$[S]^T \frac{\partial^2 P^{(e)}}{\partial x^2} = \frac{\partial}{\partial x} \left( [S]^T \frac{\partial P^{(e)}}{\partial x} \right) - \frac{\partial [S]^T}{\partial x} \frac{\partial P^{(e)}}{\partial x} \quad (3.16)$$

$$[S]^T \frac{\partial^2 P^{(e)}}{\partial y^2} = \frac{\partial}{\partial y} \left( [S]^T \frac{\partial P^{(e)}}{\partial y} \right) - \frac{\partial [S]^T}{\partial y} \frac{\partial P^{(e)}}{\partial y} \quad (3.17)$$

Substituting Equations (3.16) and (3.17) into Equation (3.12) yields

$$\iint_{\Omega^{(e)}} \left[ \frac{K}{\mu} \left( \frac{\partial}{\partial x} \left( [S]^T \frac{\partial P^{(e)}}{\partial x} \right) - \frac{\partial [S]^T}{\partial x} \frac{\partial P^{(e)}}{\partial x} \right) + \frac{\partial}{\partial y} \left( [S]^T \frac{\partial P^{(e)}}{\partial y} \right) - \frac{\partial [S]^T}{\partial y} \frac{\partial P^{(e)}}{\partial y} \right) dx dy = 0 \quad (3.18)$$

By applying Green's theorem, the area integrals can be converted to line integrals as follows

$$\iint_{\Omega^{(e)}} \frac{\partial}{\partial x} \left( [S]^T \frac{\partial P^{(e)}}{\partial x} \right) dx dy = \int_{\Gamma} \left( [S]^T \frac{\partial P^{(e)}}{\partial x} n_x \right) d\Gamma \quad (3.19)$$

$$\iint_{\Omega^{(e)}} \frac{\partial}{\partial y} \left( [S]^T \frac{\partial P^{(e)}}{\partial y} \right) dx dy = \int_{\Gamma} \left( [S]^T \frac{\partial P^{(e)}}{\partial y} n_y \right) d\Gamma \quad (3.20)$$

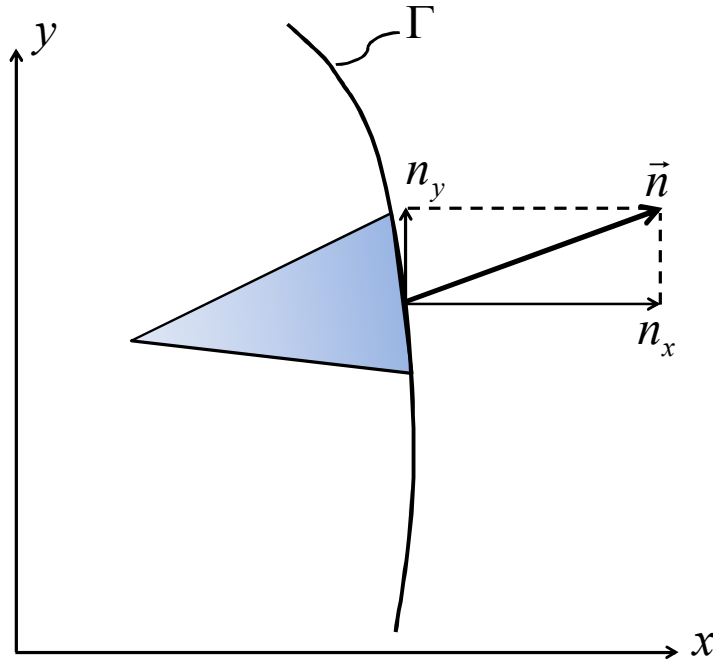


**Figure 3.3** Unit normal vector of a triangular element at global boundary

where  $n_x$  and  $n_y$  are the two components of unit normal vector to the boundary  $\Gamma$  shown in Figure 3.3. Unit normal vector  $\vec{n}$  to the boundary is as follows

$$\vec{n} = n_x \vec{i} + n_y \vec{j} \quad (3.21)$$

Substituting Equations (3.19) and (3.20) into Equation (3.18) yields

$$\begin{aligned} & \iint_{\Omega^{(e)}} \left[ \frac{K}{\mu} \left( \frac{\partial[S]^T}{\partial x} \frac{\partial P^{(e)}}{\partial x} + \frac{\partial[S]^T}{\partial y} \frac{\partial P^{(e)}}{\partial y} \right) \right] dx dy \\ & - \int_{\Gamma} \left[ \frac{K}{\mu} \left( [S]^T \frac{\partial P^{(e)}}{\partial x} n_x + [S]^T \frac{\partial P^{(e)}}{\partial y} n_y \right) \right] d\Gamma = 0 \end{aligned} \quad (3.22)$$

The first term of the area integral in Equation (3.22),  $\iint_{\Omega^{(e)}} \frac{\partial[S]^T}{\partial x} \frac{\partial P^{(e)}}{\partial x} dx dy$ , is calculated by expressing  $\frac{\partial[S]^T}{\partial x}$  and  $\frac{\partial P^{(e)}}{\partial x}$  as follows

$$\frac{\partial[S]^T}{\partial x} = \frac{\partial}{\partial x} \begin{Bmatrix} S_i \\ S_j \\ S_k \end{Bmatrix} = \frac{1}{2A} \begin{Bmatrix} \beta_i \\ \beta_j \\ \beta_k \end{Bmatrix} \quad (3.23)$$

and

$$\frac{\partial P^{(e)}}{\partial x} = \frac{\partial}{\partial x} [S_i S_j S_k] \begin{Bmatrix} P_i \\ P_j \\ P_k \end{Bmatrix} = \frac{1}{2A} [\beta_i \beta_j \beta_k] \begin{Bmatrix} P_i \\ P_j \\ P_k \end{Bmatrix} \quad (3.24)$$

Substitution of Equations (3.23) and (3.24) into  $\iint_{\Omega^{(e)}} \frac{\partial[S]^T}{\partial x} \frac{\partial P^{(e)}}{\partial x} dx dy$  yields

$$\iint_{\Omega^{(e)}} \frac{1}{4A^2} \begin{Bmatrix} \beta_i \\ \beta_j \\ \beta_k \end{Bmatrix} [\beta_i \beta_j \beta_k] \begin{Bmatrix} P_i \\ P_j \\ P_k \end{Bmatrix} dx dy = \iint_{\Omega^{(e)}} \frac{1}{4A^2} \begin{bmatrix} \beta_i^2 & \beta_i \beta_j & \beta_i \beta_k \\ \beta_i \beta_j & \beta_j^2 & \beta_j \beta_k \\ \beta_i \beta_k & \beta_j \beta_k & \beta_k^2 \end{bmatrix} \begin{Bmatrix} P_i \\ P_j \\ P_k \end{Bmatrix} dx dy \quad (3.25)$$

Entities in the integral in Equation (3.25) are independent of both  $x$  and  $y$ , in other words these entities are constants. Hence, Equation (3.25) can be re-written as

$$\begin{aligned} \frac{1}{4A^2} \begin{bmatrix} \beta_i^2 & \beta_i \beta_j & \beta_i \beta_k \\ \beta_i \beta_j & \beta_j^2 & \beta_j \beta_k \\ \beta_i \beta_k & \beta_j \beta_k & \beta_k^2 \end{bmatrix} \begin{Bmatrix} P_i \\ P_j \\ P_k \end{Bmatrix} \iint_{\Omega^{(e)}} dx dy &= \frac{1}{4A^2} \begin{bmatrix} \beta_i^2 & \beta_i \beta_j & \beta_i \beta_k \\ \beta_i \beta_j & \beta_j^2 & \beta_j \beta_k \\ \beta_i \beta_k & \beta_j \beta_k & \beta_k^2 \end{bmatrix} \begin{Bmatrix} P_i \\ P_j \\ P_k \end{Bmatrix} A \\ &= \frac{1}{4A} \begin{bmatrix} \beta_i^2 & \beta_i \beta_j & \beta_i \beta_k \\ \beta_i \beta_j & \beta_j^2 & \beta_j \beta_k \\ \beta_i \beta_k & \beta_j \beta_k & \beta_k^2 \end{bmatrix} \begin{Bmatrix} P_i \\ P_j \\ P_k \end{Bmatrix} \end{aligned} \quad (3.26)$$

since  $\iint_{\Omega^{(e)}} dx dy = A$ .

Second term of the area integral in Equation (3.22),  $\iint_{\Omega^{(e)}} \frac{\partial [S]^T}{\partial y} \frac{\partial P^{(e)}}{\partial y} dx dy$ , is calculated by expressing  $\frac{\partial [S]^T}{\partial y}$  and  $\frac{\partial P^{(e)}}{\partial y}$  as follows

$$\frac{\partial [S]^T}{\partial y} = \frac{\partial}{\partial y} \begin{bmatrix} S_i \\ S_j \\ S_k \end{bmatrix} = \frac{1}{2A} \begin{Bmatrix} \delta_i \\ \delta_j \\ \delta_k \end{Bmatrix} \quad (3.27)$$

and

$$\frac{\partial P^{(e)}}{\partial y} = \frac{\partial}{\partial y} [S_i S_j S_k] \begin{Bmatrix} P_i \\ P_j \\ P_k \end{Bmatrix} = \frac{1}{2A} [\delta_i \delta_j \delta_k] \begin{Bmatrix} P_i \\ P_j \\ P_k \end{Bmatrix} \quad (3.28)$$

Substitution of Equation (3.27) and Equation (3.28) into  $\iint_{\Omega^{(e)}} \frac{\partial [S]^T}{\partial y} \frac{\partial P^{(e)}}{\partial y} dx dy$  yields

$$\iint_{\Omega^{(e)}} \frac{1}{4A^2} \begin{Bmatrix} \delta_i \\ \delta_j \\ \delta_k \end{Bmatrix} [\delta_i \delta_j \delta_k] \begin{Bmatrix} P_i \\ P_j \\ P_k \end{Bmatrix} dx dy = \iint_{\Omega^{(e)}} \frac{1}{4A^2} \begin{bmatrix} \delta_i^2 & \delta_i \delta_j & \delta_i \delta_k \\ \delta_i \delta_j & \delta_j^2 & \delta_j \delta_k \\ \delta_i \delta_k & \delta_j \delta_k & \delta_k^2 \end{bmatrix} \begin{Bmatrix} P_i \\ P_j \\ P_k \end{Bmatrix} dx dy \quad (3.29)$$

Entities in the integral in Equation (3.29) are independent of both  $x$  and  $y$  as in Equation (3.27). Hence, Equation (3.29) can be re-written as

$$\begin{aligned} \frac{1}{4A^2} \begin{bmatrix} \delta_i^2 & \delta_i \delta_j & \delta_i \delta_k \\ \delta_i \delta_j & \delta_j^2 & \delta_j \delta_k \\ \delta_i \delta_k & \delta_j \delta_k & \delta_k^2 \end{bmatrix} \begin{Bmatrix} P_i \\ P_j \\ P_k \end{Bmatrix} \iint_{\Omega^{(e)}} dx dy &= \frac{1}{4A^2} \begin{bmatrix} \delta_i^2 & \delta_i \delta_j & \delta_i \delta_k \\ \delta_i \delta_j & \delta_j^2 & \delta_j \delta_k \\ \delta_i \delta_k & \delta_j \delta_k & \delta_k^2 \end{bmatrix} \begin{Bmatrix} P_i \\ P_j \\ P_k \end{Bmatrix} A \\ &= \frac{1}{4A} \begin{bmatrix} \delta_i^2 & \delta_i \delta_j & \delta_i \delta_k \\ \delta_i \delta_j & \delta_j^2 & \delta_j \delta_k \\ \delta_i \delta_k & \delta_j \delta_k & \delta_k^2 \end{bmatrix} \begin{Bmatrix} P_i \\ P_j \\ P_k \end{Bmatrix} \end{aligned} \quad (3.30)$$

The global stiffness matrix for any element is obtained by substituting Equations (3.25) and (3.30) into Equation (3.22)

$$C^{(e)} = \frac{K}{\mu} \frac{1}{4A} \left( \begin{bmatrix} \beta_i^2 & \beta_i \beta_j & \beta_i \beta_k \\ \beta_i \beta_j & \beta_j^2 & \beta_j \beta_k \\ \beta_i \beta_k & \beta_j \beta_k & \beta_k^2 \end{bmatrix} + \begin{bmatrix} \delta_i^2 & \delta_i \delta_j & \delta_i \delta_k \\ \delta_i \delta_j & \delta_j^2 & \delta_j \delta_k \\ \delta_i \delta_k & \delta_j \delta_k & \delta_k^2 \end{bmatrix} \right) \quad (3.31)$$

shows the global boundary conditions for this case. Left edge of the part is an injection port and the right edge of the part is a ventilation port. Boundary conditions at injection and ventilation ports are convective boundary condition type. A typical convective boundary condition for a triangular element is schematically shown in Figure 3.4 where  $q$  is flux per unit volume.

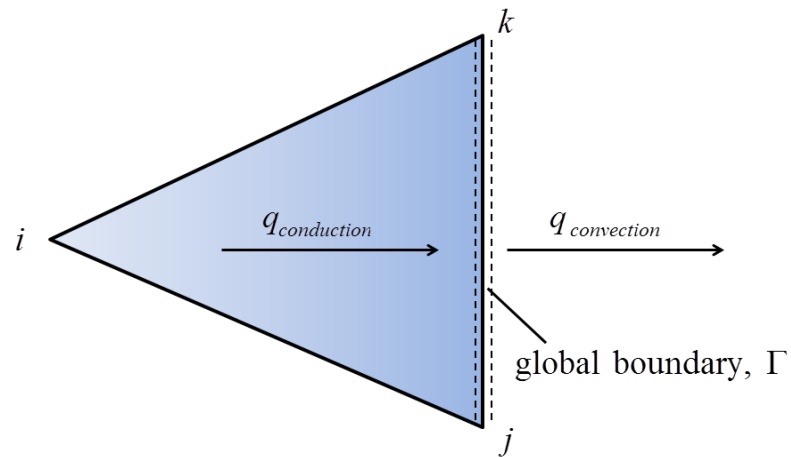


**Figure 3.4** Triangular element with convective boundary condition

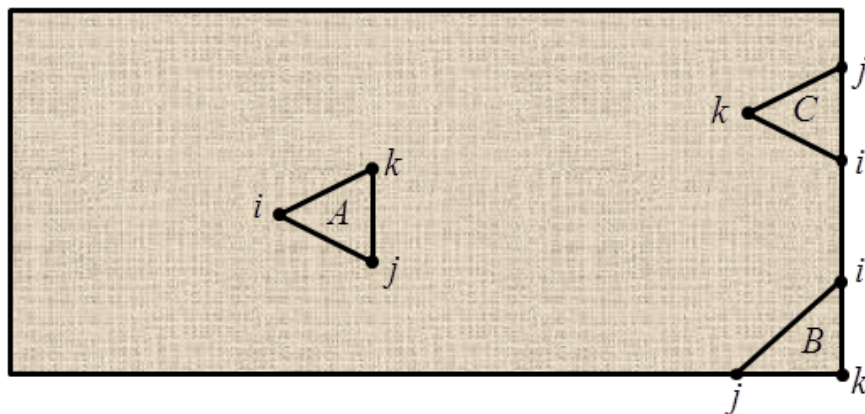


**Figure 3.5** Three elements with different convective boundaries

Convective boundary condition along the edges of a triangular element is shown below by following the reference [28]

$$C^{(e)} = \frac{ql_{ij}}{6} \begin{bmatrix} 2 & 1 & 0 \\ 1 & 2 & 0 \\ 0 & 0 & 0 \end{bmatrix} \quad (3.32)$$

$$C^{(e)} = \frac{ql_{jk}}{6} \begin{bmatrix} 0 & 0 & 0 \\ 0 & 2 & 1 \\ 0 & 1 & 2 \end{bmatrix} \quad (3.33)$$

$$C^{(e)} = \frac{ql_{ki}}{6} \begin{bmatrix} 2 & 0 & 1 \\ 0 & 0 & 0 \\ 1 & 0 & 2 \end{bmatrix} \quad (3.34)$$

where convective boundary condition can be present at one edge or at two edges, or it may not be present at all as shown in Figure 3.5. Triangular element  $C$  in Figure 3.5 has one edge with convective boundary condition, namely  $C_{ij}$ . So, Equation (3.32) gives the convection

$$C^{(e)} = \frac{ql_{ij}}{6} \begin{bmatrix} 2 & 1 & 0 \\ 1 & 2 & 0 \\ 0 & 0 & 0 \end{bmatrix} \quad \text{for element } C.$$

Element  $B$ , in the same figure has convective boundary condition at two edges, namely  $B_{jk}$  and  $B_{ki}$ . Hence, total convection from this element is equal to sum of Equations (3.33) and (3.34)

$$C^{(e)} = \frac{ql_{jk}}{6} \begin{bmatrix} 0 & 0 & 0 \\ 0 & 2 & 1 \\ 0 & 1 & 2 \end{bmatrix} + \frac{ql_{ki}}{6} \begin{bmatrix} 2 & 0 & 1 \\ 0 & 0 & 0 \\ 1 & 0 & 2 \end{bmatrix} \quad \text{for element } B.$$



Element  $A$  in Figure 3.5 has no edge with convective boundary condition, so convection from this element is equal to zero

$$C^{(e)} = 0 \quad \text{for element } A.$$

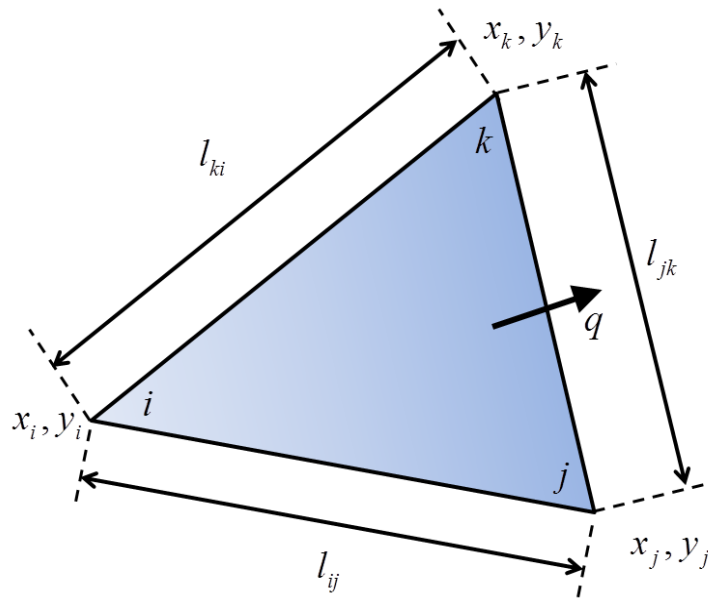


**Figure 3.6** Convective boundary condition at the edge of an element

$l_{ij}$ ,  $l_{jk}$ , and  $l_{ki}$  are shown in Figure 3.6. The flux  $q$  is equal to

$$q = \left. \begin{array}{l} \frac{Q_{inj}}{wh}, \text{ at injection boundary} \\ \frac{Q_{vent}}{wh}, \text{ at ventilation boundary} \\ 0, \text{ elsewhere} \end{array} \right\} \quad (3.35)$$

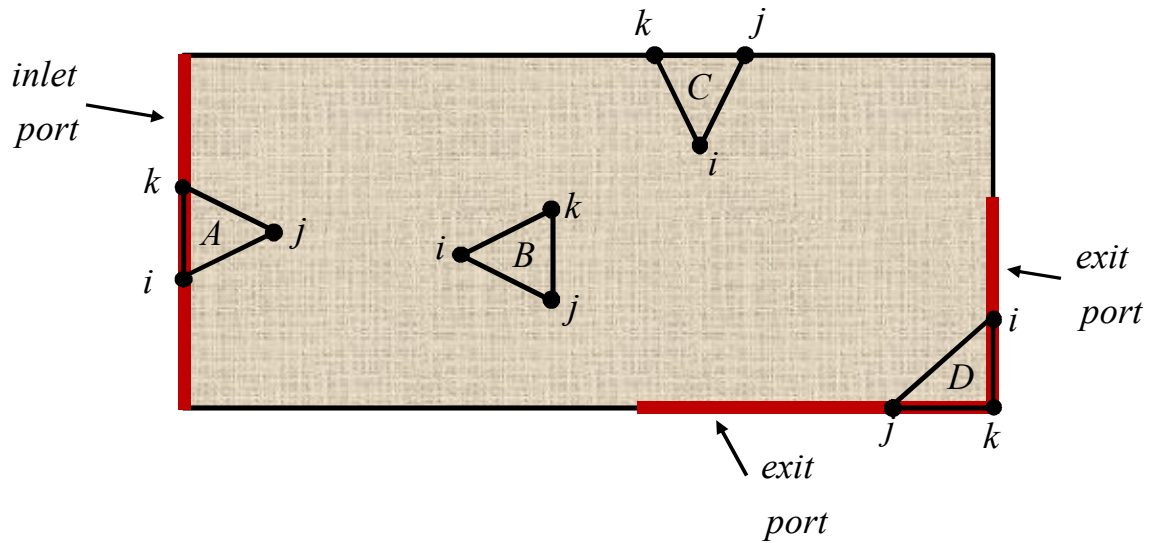


**Figure 3.7** Four separate elements in the domain

After assembling the global stiffness matrix, one should solve

$$[C]\{P\} = \{F\} \quad (3.36)$$

to obtain the pressure for all nodes.  $[C]$  is the global stiffness matrix and it is  $m \times m$  square matrix where  $m$  is the number of nodes used in the complete mesh.  $\{P\}$  and  $\{F\}$  are  $m \times 1$  column vectors.

$\{F\}$  is the load vector and it is calculated as shown in reference [28]

$$F^{(e)} = \frac{ql_{ij}}{2} \begin{Bmatrix} 1 \\ 1 \\ 0 \end{Bmatrix} \quad (3.37)$$

$$F^{(e)} = \frac{ql_{jk}}{2} \begin{Bmatrix} 0 \\ 1 \\ 1 \end{Bmatrix} \quad (3.38)$$

$$F^{(e)} = \frac{ql_{ki}}{2} \begin{Bmatrix} 1 \\ 0 \\ 1 \end{Bmatrix} \quad (3.39)$$

and it is zero everywhere except along the injection and ventilation boundaries. Figure 3.7 shows different elements which have different load vectors,  $\{F\}$ . Element A has an edge, namely  $A_{ki}$  edge, overlapping with the inlet port. Hence, load vector for this element is calculated using Equation (3.39). Element D has two edges ( $D_{jk}$ ,  $D_{ki}$ ) overlapping with the exit port, so the load vector for this element is the sum of Equations (3.38) and (3.39)

$$F^{(e)} = \frac{ql_{jk}}{2} \begin{Bmatrix} 0 \\ 1 \\ 1 \end{Bmatrix} + \frac{ql_{ki}}{2} \begin{Bmatrix} 1 \\ 0 \\ 1 \end{Bmatrix} \quad \text{for the element } D.$$

Elements B and C have no edges on either inlet or exit port, so load vectors of these elements are zero

$$F^{(e)} = 0 \quad \text{for elements } B \text{ and } C.$$

In this thesis, MATLAB and its built-in functions are used for computations. After calculating the stiffness and load matrices, the next step is to implement the calculations in MATLAB and solve the nodal pressures. The geometry is defined with dimensions and boundary conditions given in Figures 3.1 and 3.2 using MATLAB's *pdetool* toolbox. For generating mesh, *initmesh* function of MATLAB is used. *initmesh* function uses the algorithm described in [30] and Figure 3.8 shows the domain after the mesh generation. One can refine the generated mesh by using *refinemesh* function of MATLAB as seen in

Figure 3.9. One can generate a regular mesh on a rectangular geometry using triangular elements with MATLAB's *poimesh* function as seen in Figure 3.10. Domain is divided into 112 elements in Figure 3.8, 448 elements in Figure 3.9, and 600 elements in Figure 3.10.

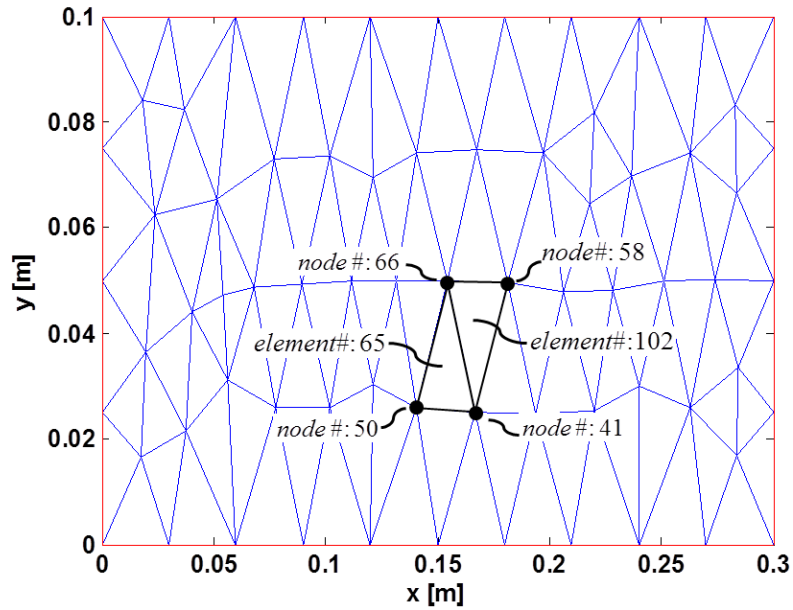


**Figure 3.8** The domain with mesh generated using *initmesh* function  
(several nodes and elements are shown for clarity purpose)

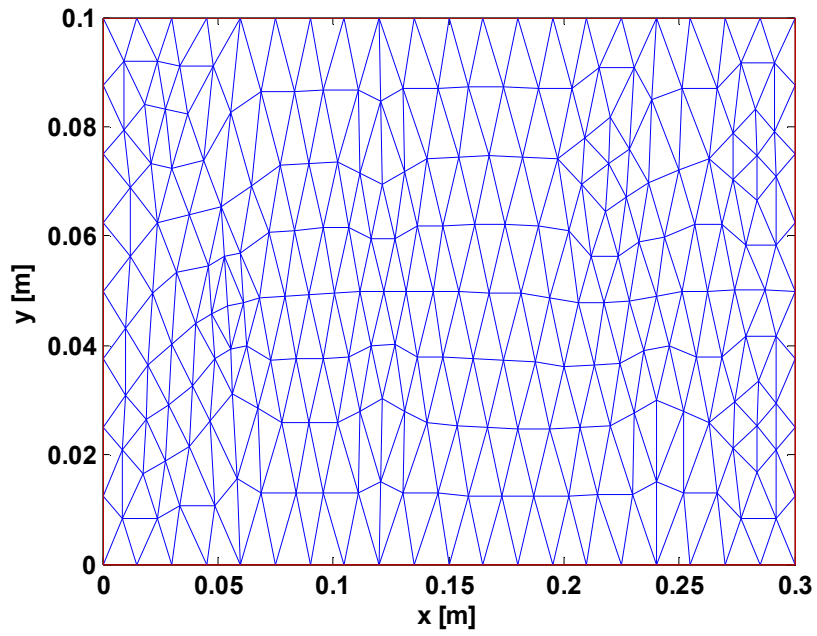


**Figure 3.9** Refined random triangular elements

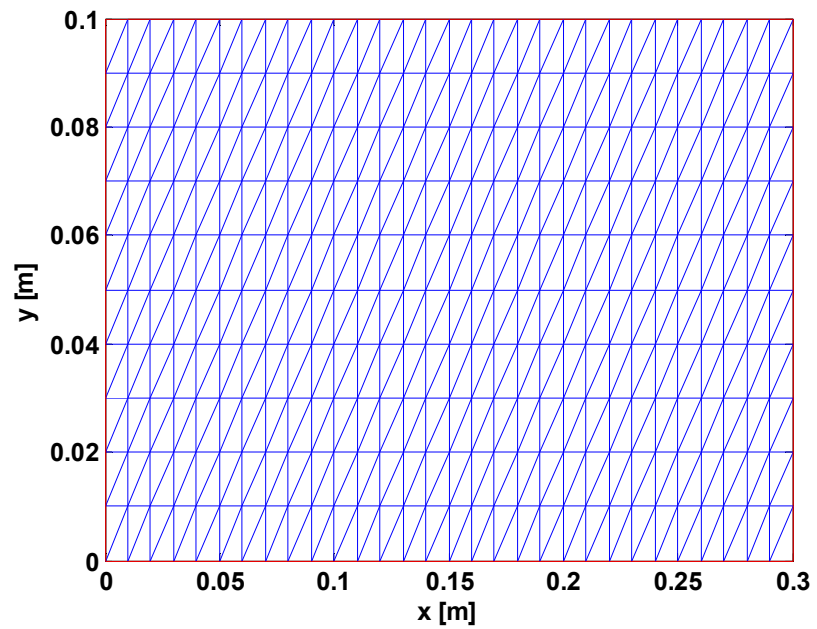
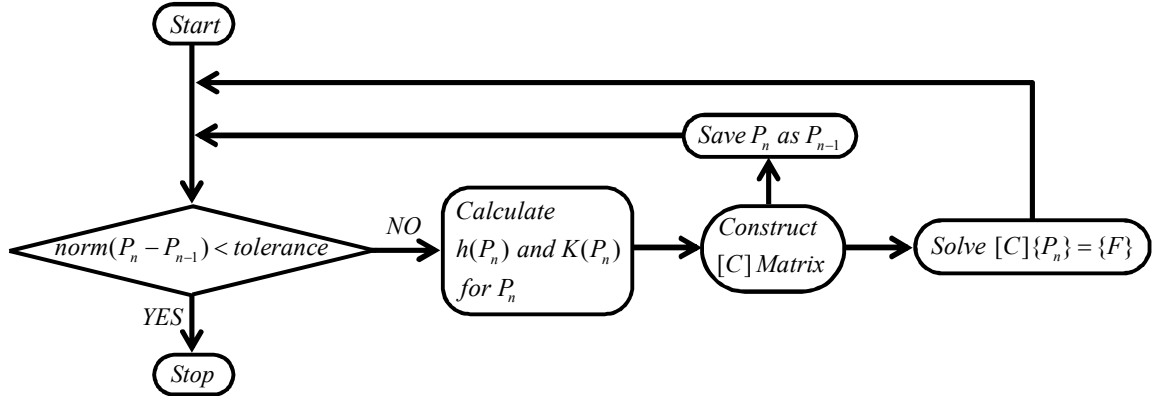


**Figure 3.10** Regular triangular elements

Iterative Scheme used in Steady Solution



Final step of the solution is to assemble the global stiffness matrix,  $[C]$  and the load vector,  $\{F\}$ . Global stiffness matrix is assembled using Equations (3.32) – (3.35). The load vector is assembled using Equations (3.37) – (3.39); and nodal pressures are solved using MATLAB. As discussed above, there are  $m$  nodes in the system and  $m$  unknown nodal pressures. The system of equations to be solved is shown in Equation (3.36) and there are  $m$  independent equations for  $m$  unknowns. Thus, the system can be solved directly (and uniquely) by using MATLAB’s backslash “\” operator as follows:

$$[C]\{P\} = \{F\} \Rightarrow \{P\} = [C] \setminus \{F\} \quad (3.40)$$

$[C]$  is a sparse matrix with a size of  $m \times m$ . MATLAB’s “\” operator uses the algorithms described in [31] for solving a sparse matrix system. The uniqueness of the solution is guaranteed if the rank of  $[C]$  is of order  $m$ ; and this is satisfied if all nodal points are distinct, (i.e., not overlapping). Since the variables  $P$ ,  $h$  and  $K$  are coupled, the solution of them is determined by using an iterative approach. The algorithm of that iterative scheme is illustrated in the flow chart above.

Figures 3.11 and 3.12 show the pressure distributions in the part calculated using MATLAB.

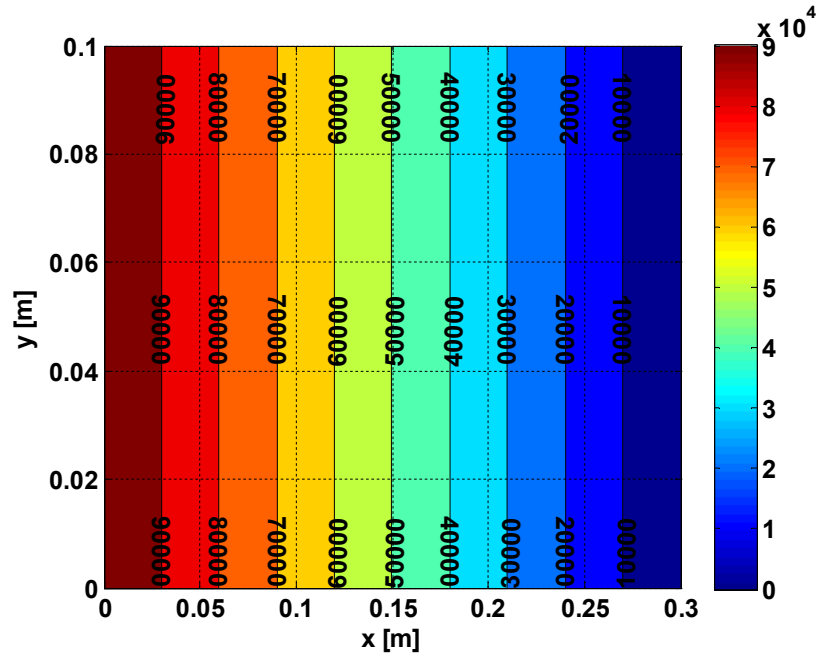


**Figure 3.11** Pressure distribution in the mold

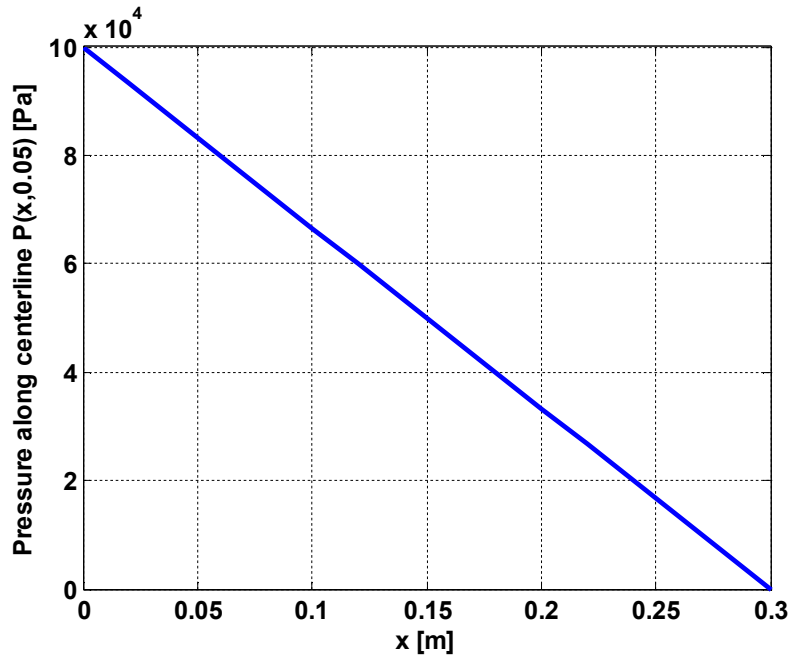


**Figure 3.12** Pressure distribution along  $y = 0.05$  m

To validate the correctness of the numerical result and determine the accuracy of it, the numerical results will be compared with the analytical result which is explained below.

The boundary conditions are  $P = 100$  kPa along the left edge (which is called a line injection), and  $P = P_{vacuum} = 0$  along the right edge (which is called a line ventilation). Due to the simple geometry and symmetry of this problem, a 1D flow is expected for this problem. Since  $u = -(K/\mu)dP/dx$ ,  $P(x)$  should be a linearly decreasing function; and it is calculated so.

The governing differential equation is as follows:

$$\frac{K}{\mu} \left( \frac{\partial^2 P}{\partial x^2} + \frac{\partial^2 P}{\partial y^2} \right) = 0 \quad (3.41)$$



After dropping  $\partial^2 P/\partial y^2$  term from Equation (3.41) due to 1D flow (i.e.,  $P \neq f(y)$ ), equation takes the following form

$$\frac{K}{\mu} \left( \frac{\partial^2 P}{\partial x^2} \right) = 0 \quad (3.42)$$

and the partial differential equation becomes an ordinary differential equation:

$$\frac{K}{\mu} \left( \frac{d^2 P}{dx^2} \right) = 0 \quad (3.43)$$

Permeability and viscosity are constant, so Equation (3.43) reduces to

$$\left( \frac{d^2 P}{dx^2} \right) = 0 \quad (3.44)$$

Integrating Equation (3.44) twice yields

$$P = C_1 x + C_2 \quad (3.45)$$

$C_1$  and  $C_2$  are calculated using boundary conditions of the problem,  $P(x = 0) = P_{inj} = 100$  kPa and  $P(x=0.3)=P_{vent} = 0$ . Solving for  $C_1$  and  $C_2$  yields

$$P = \frac{-1000000}{3} x + 100000 \quad (3.46)$$

where  $x$  is in [m] and  $P$  is in [Pa]. In this case, steady flow inside the part is solved. Hence the following equation must be satisfied

$$Q_{inj} = Q_{vent} = A \left( -\frac{K}{\mu} \frac{dP}{dx} \right) \quad (3.47)$$

Substituting Equation (3.46) into Equation (3.47), one gets

$$\begin{aligned} Q_{inj} = Q_{vent} &= A \left( -\frac{K}{\mu} \frac{dP}{dx} \right) \\ &= [(L_y)(L_z)] \left[ -\frac{K}{\mu} \frac{\partial}{\partial x} \left( \frac{-1000000}{3} x + 100000 \right) \right] \\ &= [(0.1m)(0.003m)] \left[ -\left( \frac{1 \times 10^{-9} m^2}{0.1 Pa.s} \right) \left( \frac{-1000000}{3} Pa/m \right) \right] \\ &= 1 \times 10^{-6} m^3 / s \end{aligned} \quad (3.48)$$

Post-processing the pressure distribution solution of FEM, flow rate at injection and ventilation ports are calculated. Both of them are in agreement with the result of analytical solution given by Equation (3.48). Accuracy of the numerical solution is in the order of floating-point relative accuracy, machine epsilon. It can be concluded that the error is most likely due to rounding in floating-point arithmetic. The velocity field is shown in Figure 3.13, and it is 1D, again in agreement with the analytical solution.

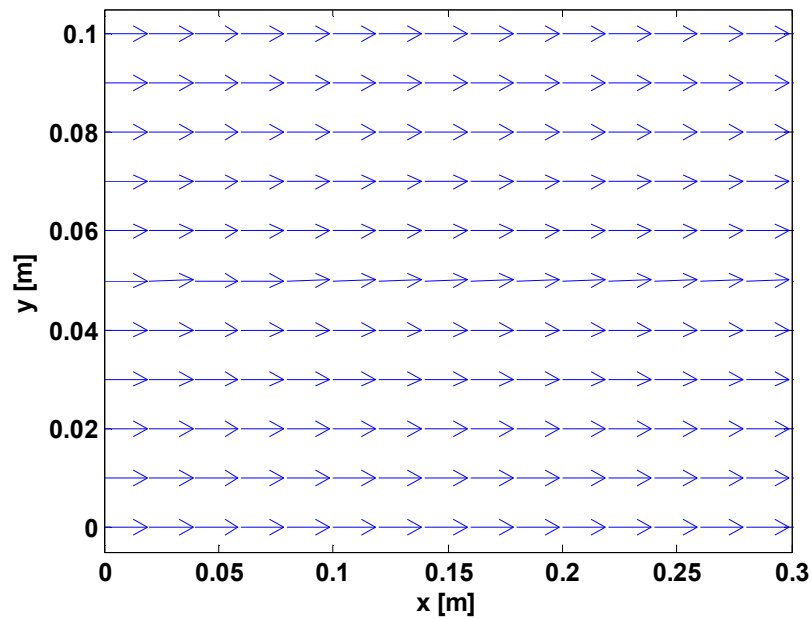


**Figure 3.13** Velocity field in the mold

### 3.2.2 Case 1-b: 2D flow

To validate the solution procedure, another simulation was performed after slightly modifying the boundary conditions as shown in Figure 3.14. Pressure distribution and velocity field are shown in Figures 3.15 and 3.16, respectively. It is difficult to get an analytical solution for this 2D flow case. The accuracy of the numerical solution was checked by comparing the inlet and exit flow rates. The inlet and exit flow rates are calculated by post-processing the MATLAB solution for nodal pressures. Five significant digits for the resin entering and leaving the mold are equal,  $Q_{inj} = Q_{vent} = 0.83721 \text{ cc/s}$ . In more detail, the accuracy of solution for injection and ventilation is in the order of machine epsilon.

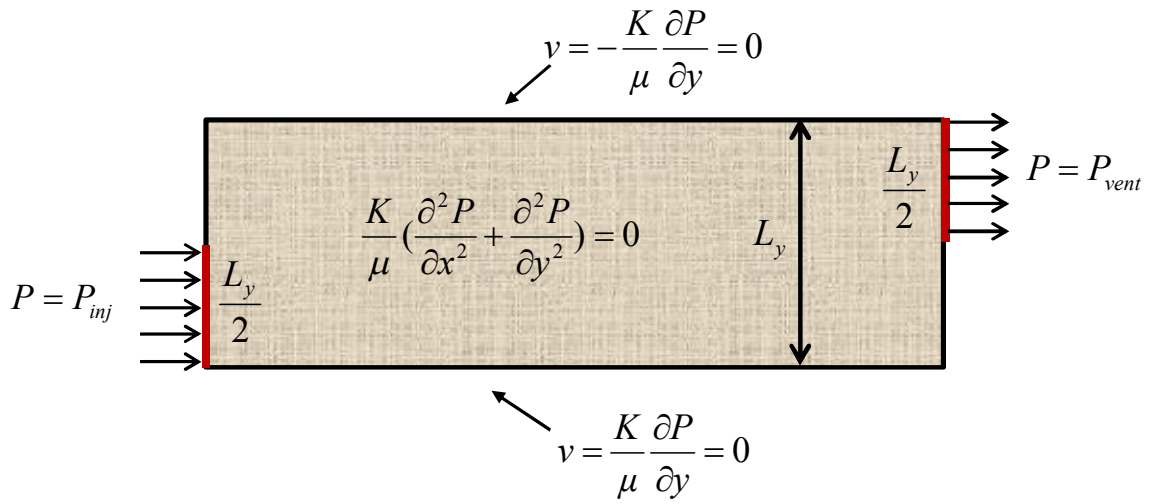


Figure 3.14 Global boundary conditions for the part

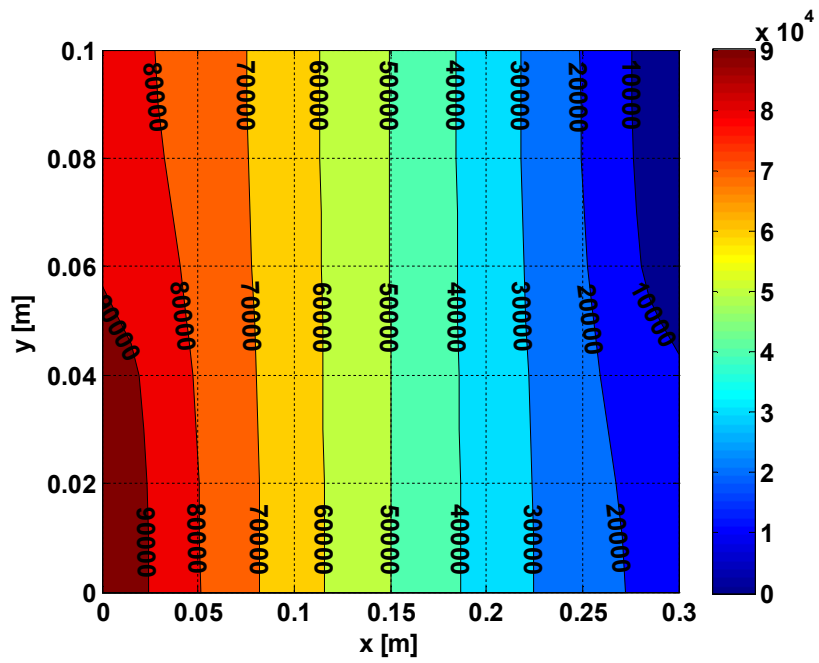
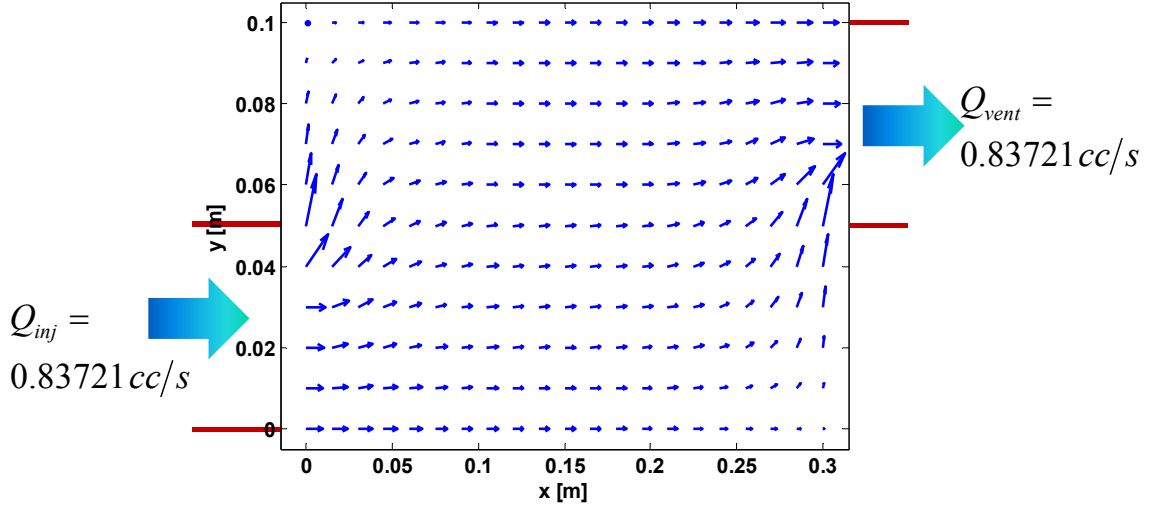


Figure 3.15 Pressure distribution in the mold



**Figure 3.16** Velocity field in the mold

### 3.3 Solution at the end of mold-filling for constant thickness and variable permeability

#### 3.3.1 Case 2-a: 1D flow

In this case, distributions of pressure and velocity components  $u$  and  $v$  will be calculated using FEM. The mold is the same as the one used in Section 3.2 except that the permeability of the porous medium,  $K$  varies spatially here, i.e.  $K = K(x)$ . It was assumed to be constant in Case 1-a, b, which is commonly assumed in RTM applications if  $h$  is constant. In this case,  $K$  is taken as a function of position as follows

$$K_{xx} = K_{yy} = K(x) = 5 \times 10^{-10} - 15 \times 10^{-10} x \quad (3.49)$$

where  $x$  is in  $[m]$  and  $K$  is in  $[m^2]$ . This corresponds to the fabric variation along  $x$ -direction as in [32] which could be due to the bending of mold plates and thus non-constant permeability,  $K \neq constant$  and  $K = K(x)$ . FEM analysis given earlier between Equations (3.1) and (3.8) is valid for this case except the following modification. This modification is

due to the variability of  $K(x)$  in this case, as expected. Equation (3.8) shows the governing equation for Case 1-a, b:

$$\frac{K}{\mu} \nabla^2 P = \frac{K}{\mu} \left( \frac{\partial^2 P}{\partial x^2} + \frac{\partial^2 P}{\partial y^2} \right) = 0 \quad (3.8)$$

while it is modified as follows to incorporate the variability of  $K$

$$\frac{1}{\mu} \nabla \cdot (K \nabla \cdot P) = \frac{1}{\mu} \left( \frac{\partial}{\partial x} \left( K \frac{\partial P}{\partial x} \right) + \frac{\partial}{\partial y} \left( K \frac{\partial P}{\partial y} \right) \right) = 0 \quad (3.50)$$

Equation (3.31) stated the global stiffness for Cases 1-a and 1-b (corresponds to Equation (3.8)) and it was as follows:

$$C^{(e)} = \frac{K}{\mu} \frac{1}{4A} \left( \begin{bmatrix} \beta_i^2 & \beta_i \beta_j & \beta_i \beta_k \\ \beta_i \beta_j & \beta_j^2 & \beta_j \beta_k \\ \beta_i \beta_k & \beta_j \beta_k & \beta_k^2 \end{bmatrix} + \begin{bmatrix} \delta_i^2 & \delta_i \delta_j & \delta_i \delta_k \\ \delta_i \delta_j & \delta_j^2 & \delta_j \delta_k \\ \delta_i \delta_k & \delta_j \delta_k & \delta_k^2 \end{bmatrix} \right) \quad (3.31)$$

Equation (3.31) is modified to account the variation in  $K = K(x)$  as follows:

$$C^{(e)} = \frac{K^{(e)}}{\mu} \frac{1}{4A} \left( \begin{bmatrix} \beta_i^2 & \beta_i \beta_j & \beta_i \beta_k \\ \beta_i \beta_j & \beta_j^2 & \beta_j \beta_k \\ \beta_i \beta_k & \beta_j \beta_k & \beta_k^2 \end{bmatrix} + \begin{bmatrix} \delta_i^2 & \delta_i \delta_j & \delta_i \delta_k \\ \delta_i \delta_j & \delta_j^2 & \delta_j \delta_k \\ \delta_i \delta_k & \delta_j \delta_k & \delta_k^2 \end{bmatrix} \right) \quad (3.51)$$

where  $K^{(e)}$  is the permeability inside the element  $e$ .  $K^{(e)}$  is calculated as follows:

$$K^{(e)} = \frac{K_i + K_j + K_k}{3} \quad (3.52)$$

which corresponds to the permeability at the centroid of the element  $e$ , as shown in Figure 3.17 .

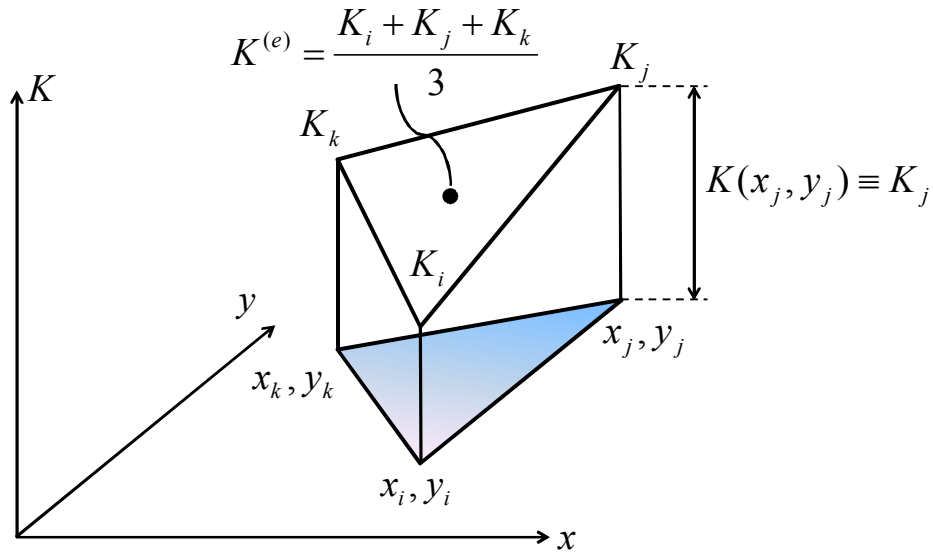


**Figure 3.17** Permeability distribution inside a triangular element

Mold dimensions were given in Figure 3.1, and governing equation at the interior of the part and boundary conditions are as shown Figure 3.18. Due to the lineal injection and ventilation ports, the flow is 1D in this case as in Case 1-a. The simulated pressure isocurves in Figure 3.19 verifies this expectation and Figure 3.20 shows the pressure distribution along  $y = 0.05\text{m}$ . To further check the validity of the FEM analysis and solution, the numerical results were compared with the results of analytical solution which is given below.

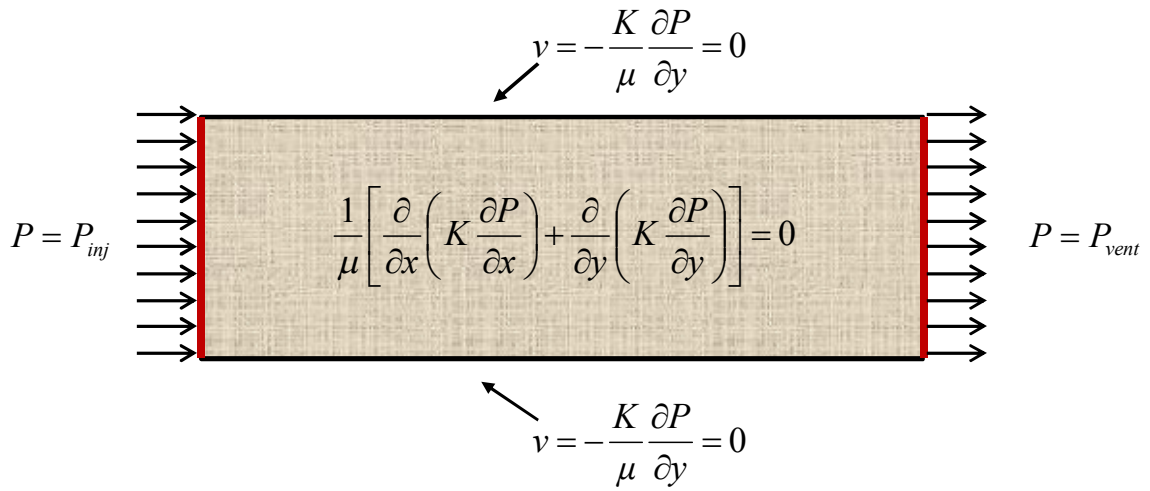


Figure 3.18 Global boundary conditions for the part

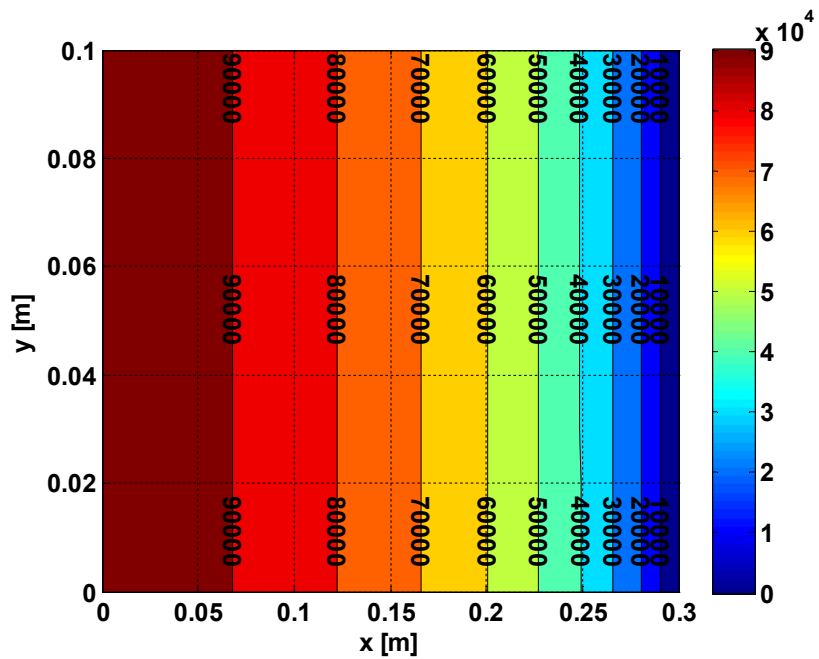
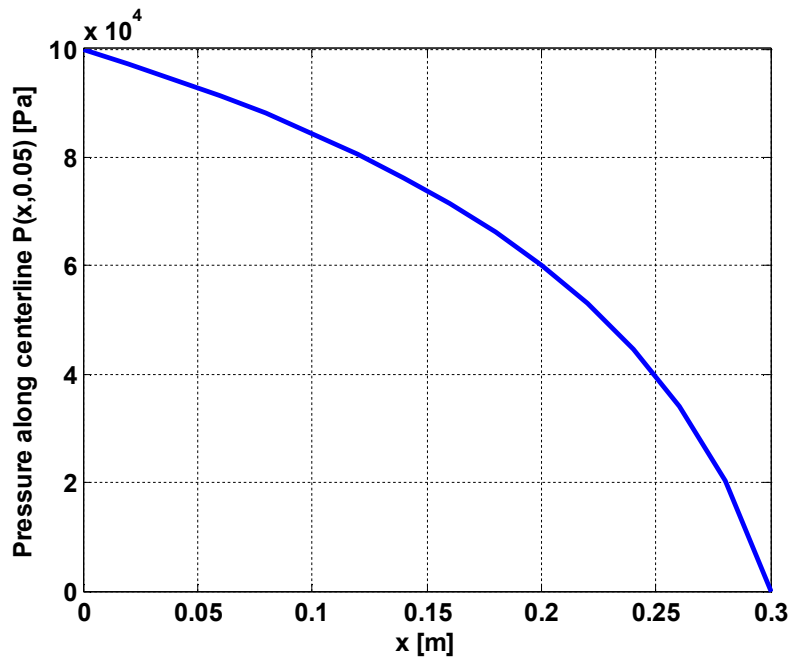


Figure 3.19 Pressure distribution in the mold





**Figure 3.20** Pressure distribution along  $y = 0.05$  m

Darcy's Law relates the velocity to the pressure gradient:

$$u = -\frac{K}{\mu} \frac{dP}{dx} \quad (3.53)$$

for 1D flow. Multiplying both sides with cross-sectional area yields the flow rate

$$Q = Au = -A \frac{K}{\mu} \frac{dP}{dx} \quad (3.54)$$

which is constant for any cross-section along x-axis due to 1D flow and constant  $h$ .

Rearranging Equation (3.54) yields:

$$\frac{dP}{dx} = -\frac{\mu Q}{A} \frac{1}{K} \quad (3.55)$$

Substituting Equation (3.49) into Equation (3.55) yields

$$\frac{dP}{dx} = -\frac{\mu Q}{A} \frac{1}{5 \times 10^{-10} - 15 \times 10^{-10} x} \quad (3.56)$$

Integrating both sides of Equation (3.56) results in

$$\int_0^x \frac{dP}{dx} dx = -\int_0^x \frac{\mu Q}{A} \frac{1}{5 \times 10^{-10} - 15 \times 10^{-10} x} dx \quad (3.57)$$

Let  $u = 5 \times 10^{-10} - 15 \times 10^{-10} x$ , then  $dx = 15 \times 10^{-10} du$ . Then

$$\int_0^x \frac{dP}{dx} dx = -\frac{\mu Q}{A} \int_0^x \frac{1}{u} (-15 \times 10^{10} du) = \mu Q (15 \times 10^{10}) \int_0^x \frac{1}{u} du \quad (3.58)$$

and

$$P(x) - P(0) = \frac{\mu Q (15 \times 10^{10})}{A} [\ln(u)]_0^x = \frac{\mu Q (15 \times 10^{10})}{A} \left[ \ln(5 \times 10^{-10} - 15 \times 10^{-10} x) \right]_0^x \quad (3.59)$$

where  $P(0) = P_{inj} = 100 \text{ kPa}$  and  $P(L_x) = P(0.3) = P_{vent} = 0$ . Rewriting Equation (3.59) yields

$$P(x) = \frac{\mu Q (15 \times 10^{10})}{A} \ln \left( \frac{5 \times 10^{-10} - 15 \times 10^{-10} x}{5 \times 10^{-10}} \right) + P_{inj} \quad (3.60)$$

The exit flow rate at the ventilation port ( $x = L_x = 0.3m$ ) is calculated using Equation (3.60)

$$P_{vent} = \frac{\mu Q (15 \times 10^{10})}{A} \ln \left( \frac{5 \times 10^{-10} - 15 \times 10^{-10} 0.3}{5 \times 10^{-10}} \right) + P_{inj} \quad (3.61)$$

re-written as:

$$0 = \frac{\mu Q (15 \times 10^{10})}{A} \ln \left[ (5 \times 10^{-10} - (15 \times 10^{-10})(0.3))(5 \times 10^{10}) \right] + 100000 \quad (3.62)$$

where viscosity of liquid resin,  $\mu$ , is set to  $0.1 Pa.s$ . Hence

$$\begin{aligned} Q &= -10^5 \frac{15 \times 10^{-10}}{0.1 Pa.s} [(0.1)(0.003)] \left[ \ln \left[ (5 \times 10^{-10} - (15 \times 10^{-10})(0.3))(5 \times 10^{10}) \right] \right]^{-1} \\ &= 0.195 cc/s \end{aligned} \quad (3.63)$$

Being able to calculate the flow rate at inlet/exit ports analytically allows us to check the correctness of the solution algorithm of the FEM solution by comparing these flow rates with the FEM's results. Both solutions for pressure distributions along  $y = 0.05m$  are seen in Figure 3.21. Analytical solution for pressure distribution is obtained by substituting result of Equation (3.63) into Equation (3.60) and solving Equation (3.60) for  $0 < x < 0.3m$ . A mesh with  $N = 300$  elements consisting of regularly distributed 12 nodes in x-direction and 12 nodes in y-direction was used for numerical solution of pressure distribution. Even for this coarse mesh, numerical solution fits well to analytical solution. To further investigate the effect of number of elements,  $Q$  is calculated by varying  $N$ . As seen from Figure 3.22, the error decays logarithmically as  $N$  increases. The analytical solution in Figure 3.21 is obtained as explained above. Velocity field in Figure 3.24 is 1D, which is in agreement with the analytical solution. Figure 3.23 shows the relation between

maximum percentage error and number of elements in logarithmic scale. As seen from the figure, the error decreases logarithmically as N increases.

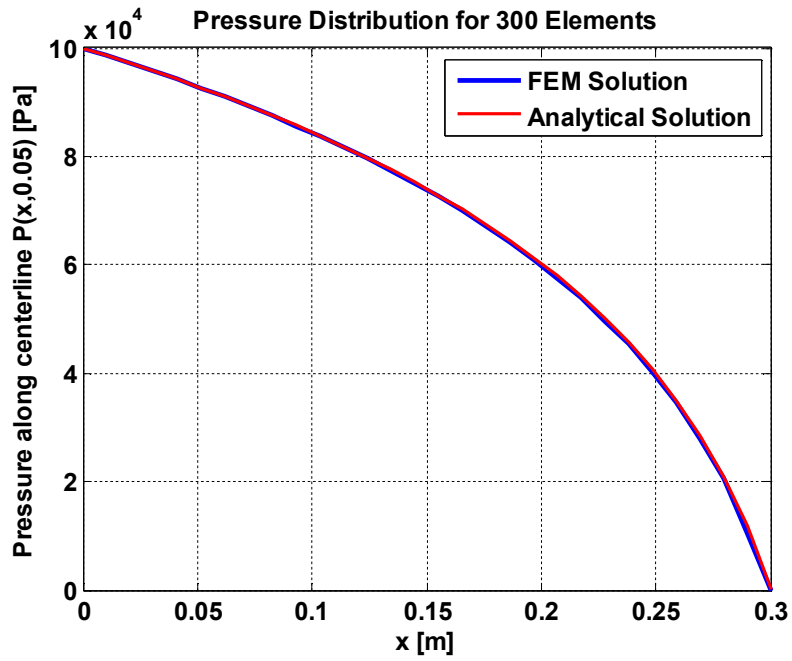


Figure 3.21 Pressure distribution along  $y = 0.05$  m

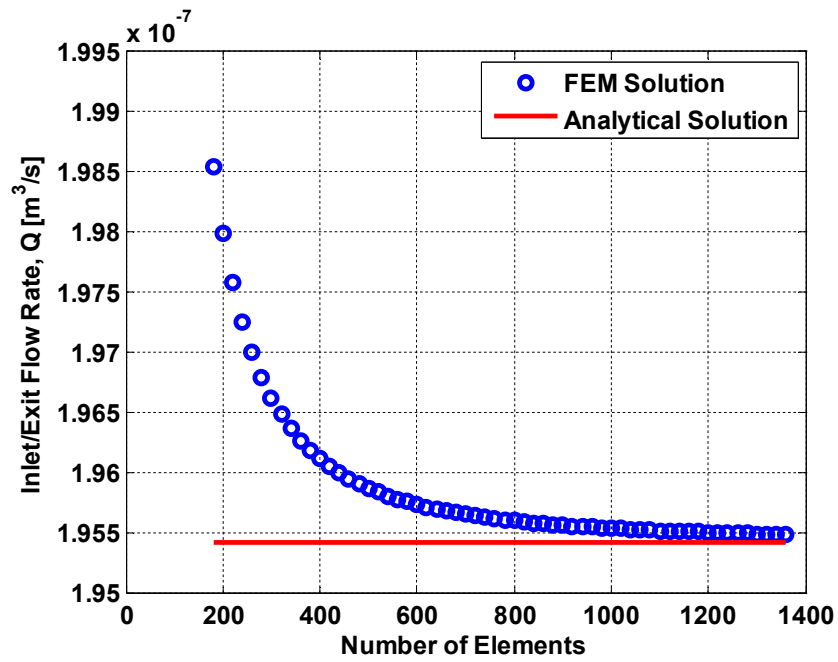


Figure 3.22 Effect of number of elements on flow rate

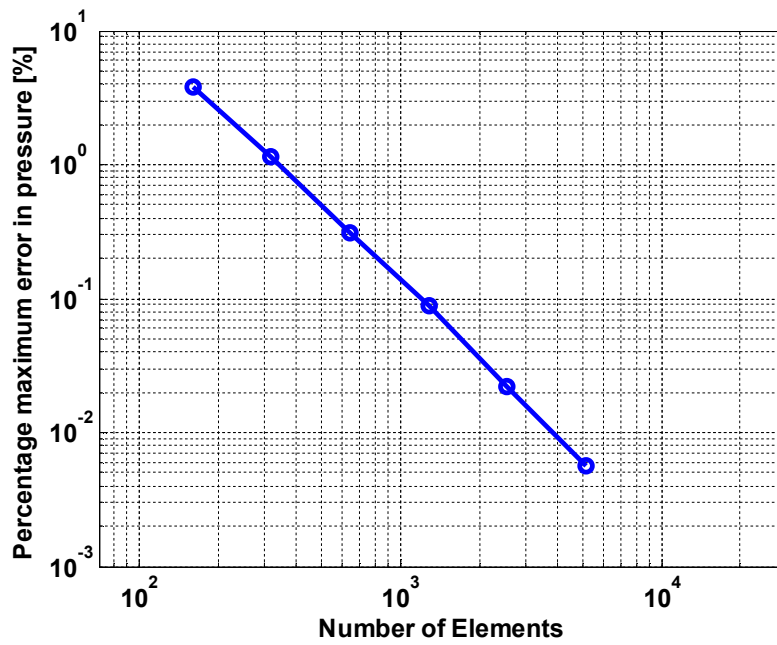
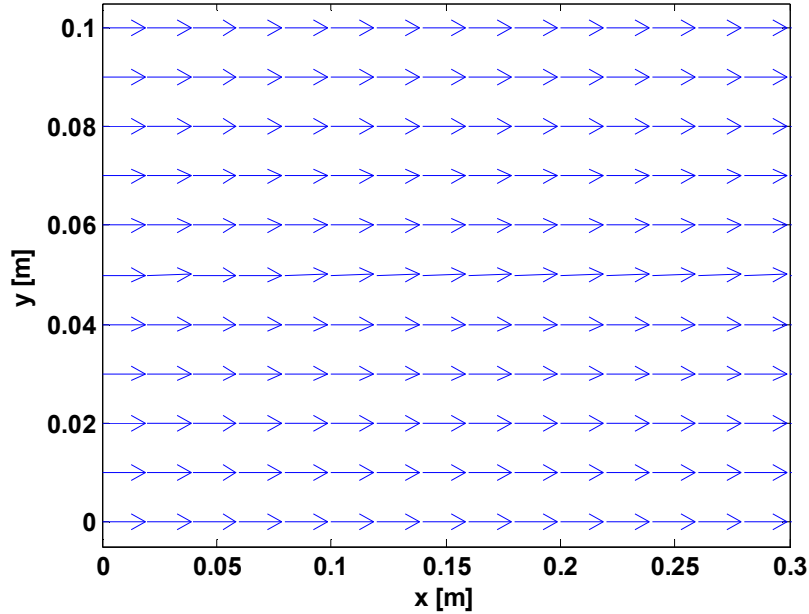


Figure 3.23 Effect of number of elements on error in pressure



**Figure 3.24** Velocity field in the mold

### 3.3.2 Case 2-b: 2D flow

Boundary conditions are modified as shown in Figure 3.25, and simulation is repeated for updated boundary conditions to validate the FEM analysis and the solution. It is easy to predict that the flow will be 2D, so analytical solution to this case is difficult to get. Instead, validity of this modified case will be checked by comparing the flow rates at inlet and exit ports and to see if global mass conservation is satisfied. Numerical results of FEM for flow rates at inlet and exit ports are calculated by post-processing the nodal pressures (seen in Figure 3.26). Figure 3.27 shows the velocity field in the mold and flow rates at inlet and exit ports. As seen from Figure 3.27, five significant digits for inlet flow rate and sum of exit flow rates are equal,  $Q_{inj} = Q_{vent,1} + Q_{vent,2} = 0.25116 \text{ cc/s}$ . Also, accuracy of the inlet and exit flow rates is on the order of machine accuracy.  $Q_{vent,1}$  is about five times larger than  $Q_{vent,2}$ , and this difference is attributed to pressure gradient at the exit ports. As seen in Figure 3.25, exit port on the upper side of the mold is closer to the inlet port when compared to the exit port on the right side of the mold. Pressures on the exit

ports are equal,  $Q_{vent,2}$ , so the port with smaller distance to the source has a higher pressure gradient and higher flow rate than the other port.

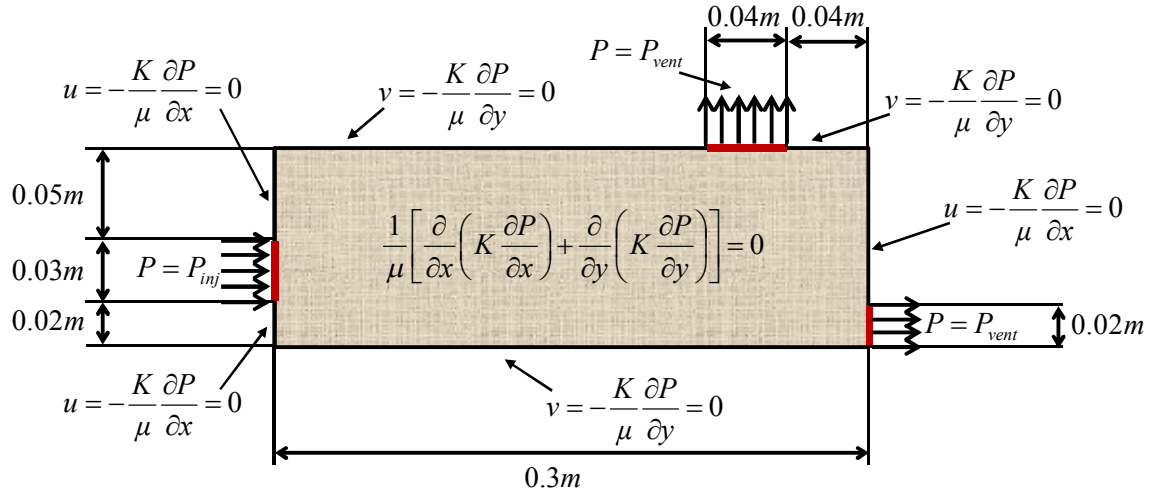


Figure 3.25 Differential equation and global boundary conditions for the part

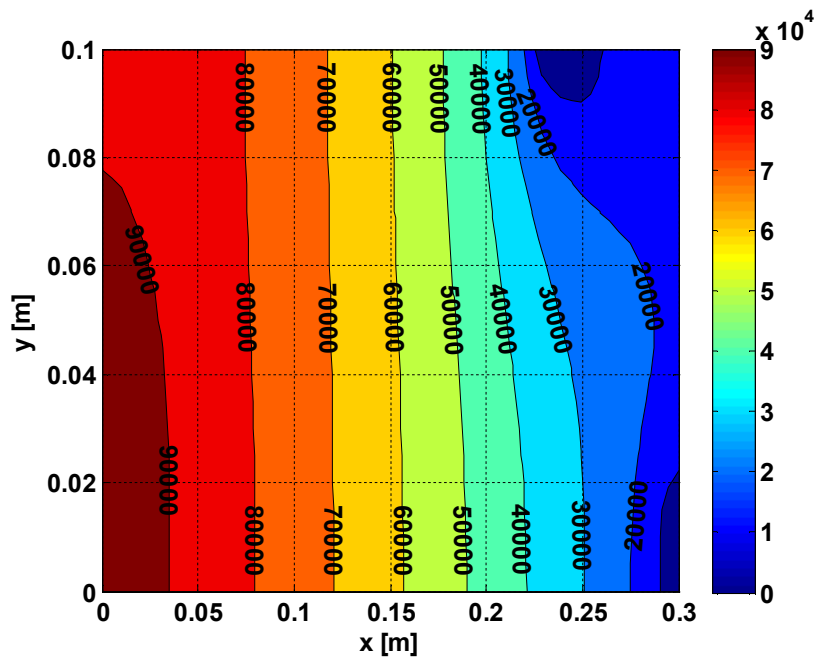


Figure 3.26 Pressure distribution in the mold

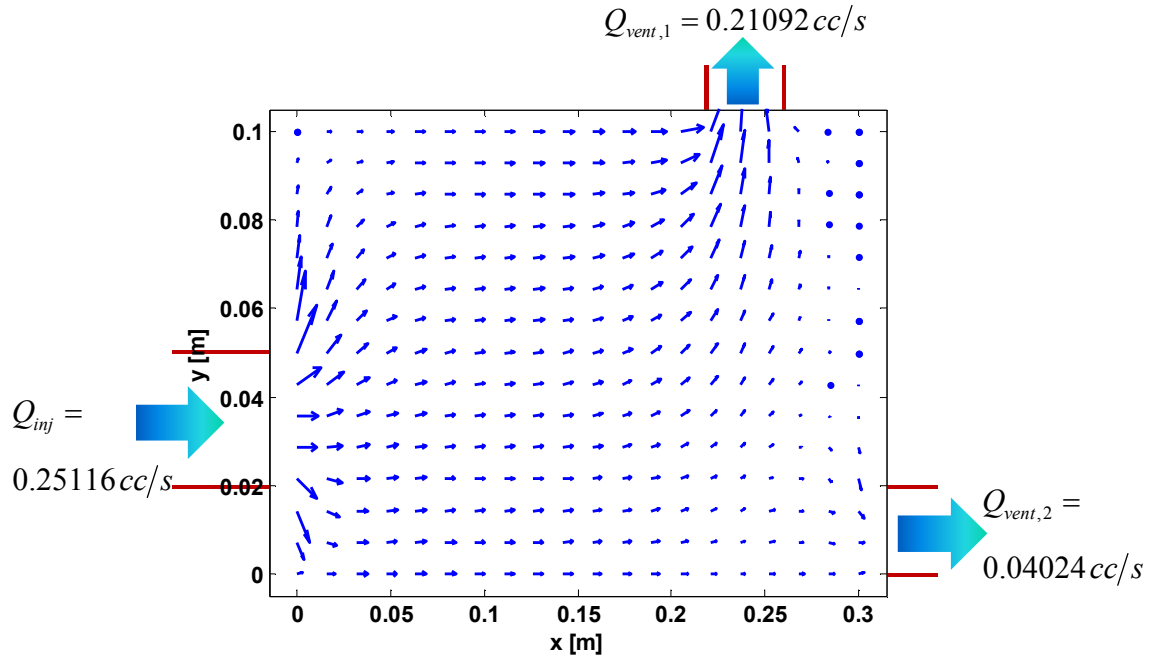


Figure 3.27 Velocity field in the mold

### 3.4 Solution for variable thickness and variable permeability

#### 3.4.1 Case 3-a: Solution at the end of mold-filling

In this part of the study, distribution of pressure in the mold, and velocity components  $u$  and  $v$  will be calculated using FEM. In previous cases, permeability of porous medium ( $K$ ) and thickness of fabric ( $h$ ) were either constant or varied spatially, i.e.  $K=K(x)$ . Compaction of fabric is usually modeled using empirical models [2-5], and in this study, compaction behavior is given by curve-fitting to the experimental data given in [18]. The form of equation to relate the thickness and compaction pressure is as follows:

$$P_c = Ae^{BV_f} \quad (3.64)$$

which can be re-written as

$$V_f = \frac{1}{B}[-\ln A + \ln P_c] \quad (3.65)$$



where  $P_c$  is compaction pressure

$$P_c = P_{atm} - P \quad (3.66)$$

where  $P_{atm}$  and  $P$  are the atmospheric pressure and the resin pressure.  $V_f$  is the fiber volume fraction which is calculated as follows

$$V_f = \frac{\rho_{sup,preform}}{\rho_{fiber}} \frac{1}{h} = \frac{n\rho_{sup,fabric}}{\rho_{fiber}} \frac{1}{h} \quad (3.67)$$

which can be re-written as

$$h = \frac{n\rho_{sup,fabric}}{\rho_{fiber}} \frac{1}{V_f} \quad (3.68)$$

where  $\rho_{sup,fabric}$  is superficial density of one layer of fabric,  $\rho_{fiber}$  is bulk density of fiber,  $n$  is the number of fabric layers and  $h$  is the thickness of preform. For eight layers of random fabric used in [18]:

$$h = \frac{(8)(0.450)}{2540} \frac{1}{V_f} \quad (3.69)$$

where  $h$  is in  $[m]$ . Coefficients given in Equation (3.65) are calculated by curve-fitting to experimental data given in [18] which result in the following

$$V_f = \frac{1}{19.42} [-\ln(2.04) + \ln(P_c)] = \frac{1}{19.42} \left[ \ln\left(\frac{P_c}{2.04}\right) \right] \quad (3.70)$$

Combining Equations (3.69) and (3.70) yields

$$h = \frac{(8)(0.450)}{2540} \frac{19.42}{\ln\left(\frac{P_c}{2.04}\right)} \quad (3.71)$$

Permeability of the fabric,  $K$ , is dependent on fiber volume fraction, and it is usually modeled by curve-fitting to experimental data. In this study, it is modeled by curve-fitting to the experimental data given in [15]. The form of equation to relate the permeability,  $K$ , and fiber volume fraction,  $V_f$  is as follows:

$$K = Ce^{DV_f} \quad (3.72)$$

The same fabric type was used in both [15] and [18], so

$$V_f = \frac{(8)(0.450)}{2540} \frac{1}{h} \quad (3.73)$$

is valid for eight layers of random fabric. Curve-fitting to the experimental data in [15] yields

$$K = (2.73 \times 10^{-9}) e^{-8.59V_f} \quad (3.74)$$

Case 3 consists of three main parts. In the first part, steady solution for boundary conditions given in Figure 3.28 will be obtained. In the second part, boundary conditions will be modified as shown in Figure 3.31; and in the third part, steady nodal pressures will be solved for the boundary conditions given in Figure 3.31.

To begin with the first part of the case, one should solve the continuity equation to simulate the pressure distribution and the other variables (thickness, permeability, and velocity components) dependent on pressure. One can begin with the continuity equation

$$\frac{\partial \rho}{\partial t} + \nabla \cdot (\rho \bar{u}) = f \quad (3.75)$$

Differential equation given in Equation (3.75) is solved in an infinitesimal volume. Multiplying both sides by  $dV$  yields

$$\frac{\partial}{\partial t}(\rho dV) + \nabla \cdot (\rho \bar{u} dV) = F \quad (3.76)$$

where  $dV = dx dy dz$  and  $F = f dV$ . In previous cases,  $dV$  was fixed meaning that its dimensions were constant. Hence, we could take  $dV$  out of the differential equation and then drop it from equation. In this case,  $dV$  is not constant; so we should consider the variability of  $dV$  during modeling and calculations. There is no mass generation in this case, so the right-hand side of Equation (3.76) is set to zero

$$\frac{\partial}{\partial t}(\rho dV) + \nabla \cdot (\rho \bar{u} dV) = 0 \quad (3.77)$$

which can be re-written as

$$\frac{\partial}{\partial t}(\rho h dx dy) + \nabla \cdot (\rho \bar{u} h dx dy) = \left[ \frac{\partial}{\partial t}(\rho h) + \nabla \cdot (\rho \bar{u} h) \right] dx dy = 0 \quad (3.78)$$

Here, thickness ( $h$ ) corresponds to  $dz$ ;  $dx$  and  $dy$  are length and width of the control volume, respectively. In this case,  $dx$  and  $dy$  are constants. We can drop  $dx$  and  $dy$  from Equation (3.78)

$$\left[ \frac{\partial}{\partial t}(\rho h) + \nabla \cdot (\rho h \bar{u}) \right] = 0 \quad (3.79)$$

The fluid is incompressible, so  $\rho$  is constant and its change with time is equal to 0. Dropping  $\partial\rho/\partial t$  term from Equation (3.79), it takes the following form:

$$\nabla \cdot (\rho h \bar{u}) = 0 \quad (3.80)$$

Since  $\rho$  is constant, and right-hand side of Equation (3.80) is zero, one can also drop  $\rho$  term, and it becomes:

$$\nabla \cdot (h \bar{u}) = 0 \quad (3.81)$$

Darcy's law describes 2D flow through a porous medium as follows:

$$\begin{Bmatrix} u \\ v \end{Bmatrix} = -\frac{1}{\mu} \begin{bmatrix} K_{xx} & K_{xy} \\ K_{yx} & K_{yy} \end{bmatrix} \begin{Bmatrix} \partial P / \partial x \\ \partial P / \partial y \end{Bmatrix} \quad (3.82)$$

where  $\mu$  is the viscosity of liquid resin,  $[K]$  is the permeability tensor of porous medium, and  $P(x, y)$  is the pressure distribution at the end of the mold filling (at  $t = t_{fill}$ ). As in the previous cases, the principal axes are  $x$  and  $y$  so that:

$$K_{xy} = K_{yx} = 0 \quad (3.83)$$

and random fabric which is isotropic is considered in this study; thus

$$K_{xx} = K_{yy} \equiv K \quad (3.84)$$

and  $\mu$  is constant as in previous cases. Combining Equations (3.81) and (3.82) yields

$$-\frac{1}{\mu} \nabla \cdot (Kh \nabla P) = -\frac{1}{\mu} \nabla \cdot \left( Kh \frac{\partial P}{\partial x} + Kh \frac{\partial P}{\partial y} \right) = 0$$

or (3.85)

$$\frac{1}{\mu} \nabla \cdot (Kh \nabla P) = \frac{1}{\mu} \left( \frac{\partial}{\partial x} \left[ Kh \frac{\partial P}{\partial x} \right] + \frac{\partial}{\partial y} \left[ Kh \frac{\partial P}{\partial y} \right] \right) = 0$$

Dimensions of the mold used in this case are the same as the previous cases. The boundary conditions are given in Figure 3.28 where  $P_{inj} = 90 \text{ kPa} = 90000 \text{ Pa}$  and  $P_{vent} = 10 \text{ kPa} = 10000 \text{ Pa}$ .

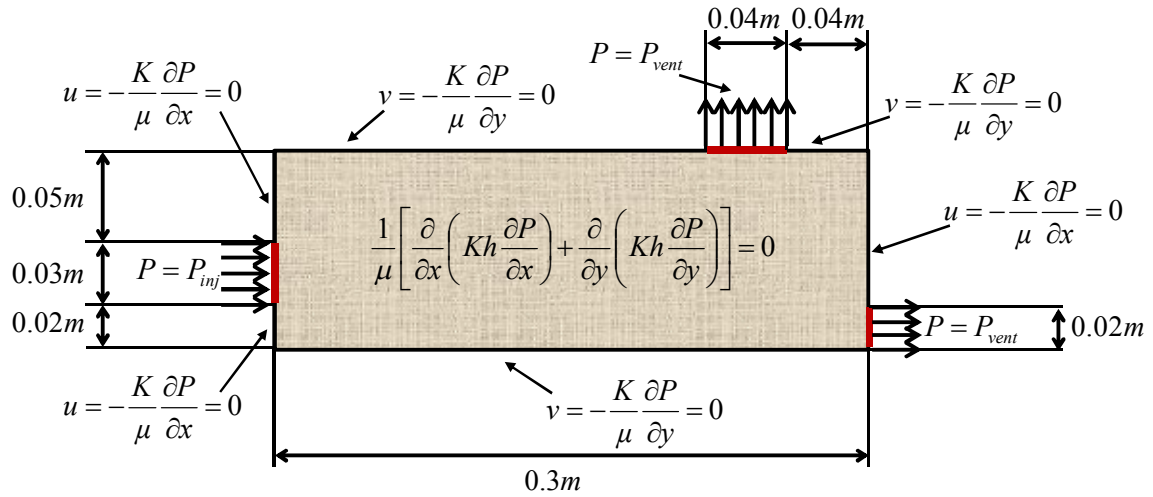


**Figure 3.28** Global boundary conditions for the part

In previous cases,  $h$  was constant and right-hand sides of the governing equations were equal to 0; so we dropped  $h$  term from the equations. In this case,  $h$  is a function of  $x$  as  $h(x)$  and we incorporate  $h$  terms in a similar way to incorporating  $K$  term in Section 3.3. Equation (3.8) shows the governing equation for constant  $K$  and constant  $h$  case and equation (3.50) shows the governing equation for variable  $K$  and constant  $h$  case. Equation (3.85) is the governing equation for this case and it is similar to Equation (3.50) except that it is also multiplied by  $h$ . Equation (3.51) gives the global stiffness matrix for variable  $K$  and constant  $h$  case and it is slightly modified to incorporate the variability of  $h$  as follows

$$C^{(e)} = \frac{h^{(e)}K^{(e)}}{\mu} \frac{1}{4A} \left( \begin{bmatrix} \beta_i^2 & \beta_i\beta_j & \beta_i\beta_k \\ \beta_i\beta_j & \beta_j^2 & \beta_j\beta_k \\ \beta_i\beta_k & \beta_j\beta_k & \beta_k^2 \end{bmatrix} + \begin{bmatrix} \delta_i^2 & \delta_i\delta_j & \delta_i\delta_k \\ \delta_i\delta_j & \delta_j^2 & \delta_j\delta_k \\ \delta_i\delta_k & \delta_j\delta_k & \delta_k^2 \end{bmatrix} \right) \quad (3.86)$$

where  $h^{(e)}$  and  $K^{(e)}$  are thickness and permeability at the centroid of the element  $e$ , respectively.

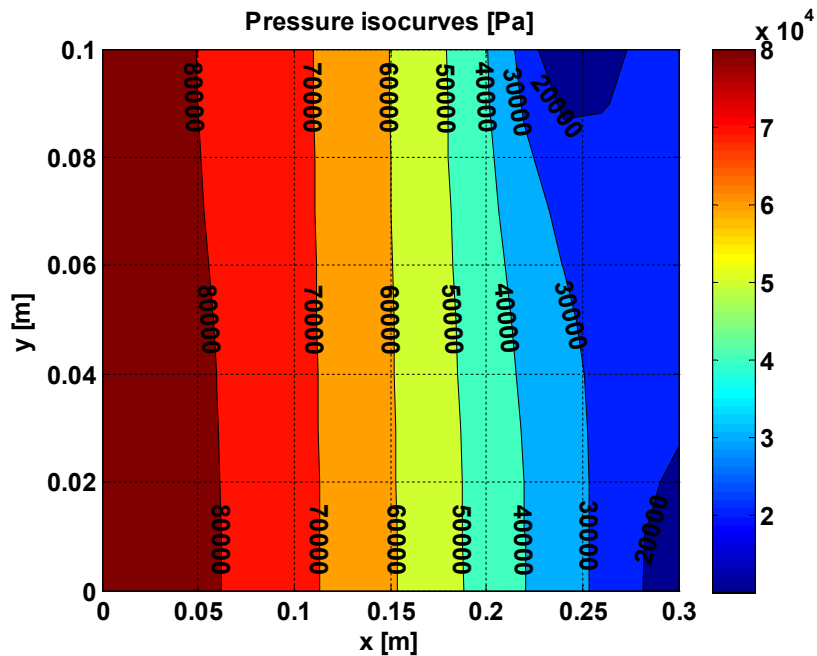
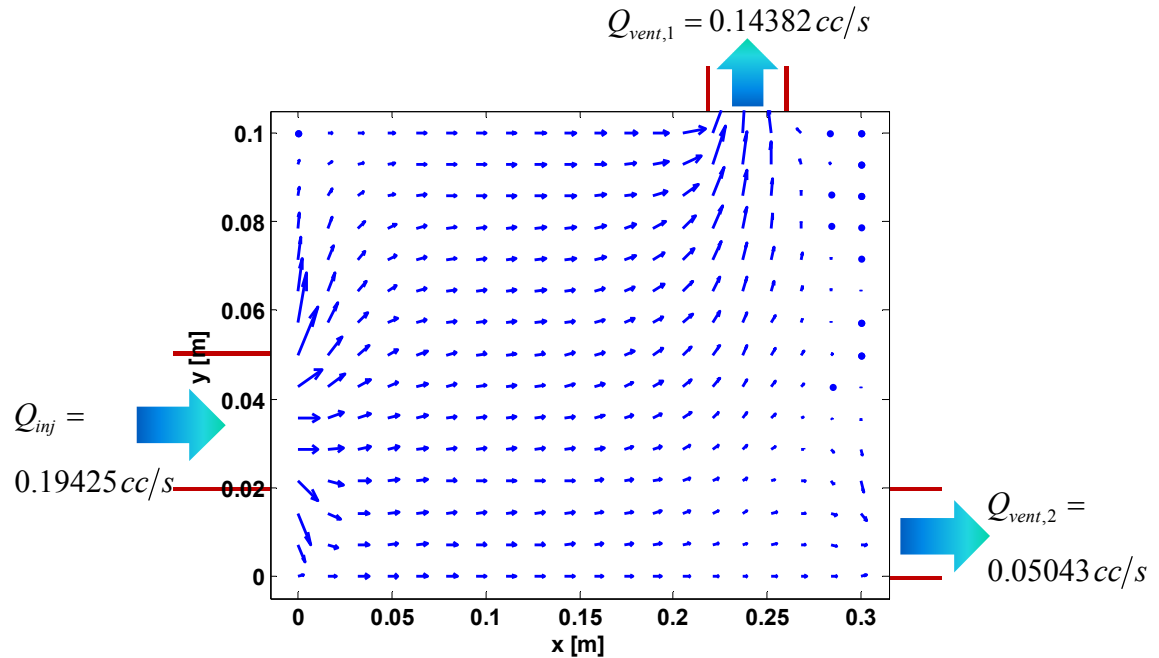


Figure 3.29 Pressure distribution in the mold



**Figure 3.30** Velocity field in the mold

As seen in Figure 3.29, pressure gradient at the exit port on the upper side of the mold is steeper than the gradient at the other exit port. Figure 3.30 shows the velocity field in the mold and flow rates at the inlet and exit ports.  $Q_{vent,1}$  is about three times larger than  $Q_{vent,2}$ , in agreement with the pressure gradient difference between the exit ports. Also, the sum of the exit flow rates is equal to the inlet flow rate with an accuracy of five significant digits. The accuracy is in the order of machine accuracy as in the previous cases.

### 3.4.2 Case 3-b: Evolution of solution with time due to change in boundary conditions

Control actions are commonly applied in VARTM [19] to decrease the thickness variation along the part are common. Control actions are usually taken by modifying the pressures at inlet and exit port or simply by closing some of them. In this part, a typical control action is simulated (see Figure 3.31). The inlet port at the left side of the mold is

closed and pressure at the exit ports remained the same,  $10\text{ kPa}$ . Closing of the inlet port(s) and applying vacuum from exit ports is called bleeding in VARTM. Evolution of pressure, thickness, and permeability throughout the part is observed during bleeding. The code is run to simulate the first 1200 seconds after the boundary condition is updated.

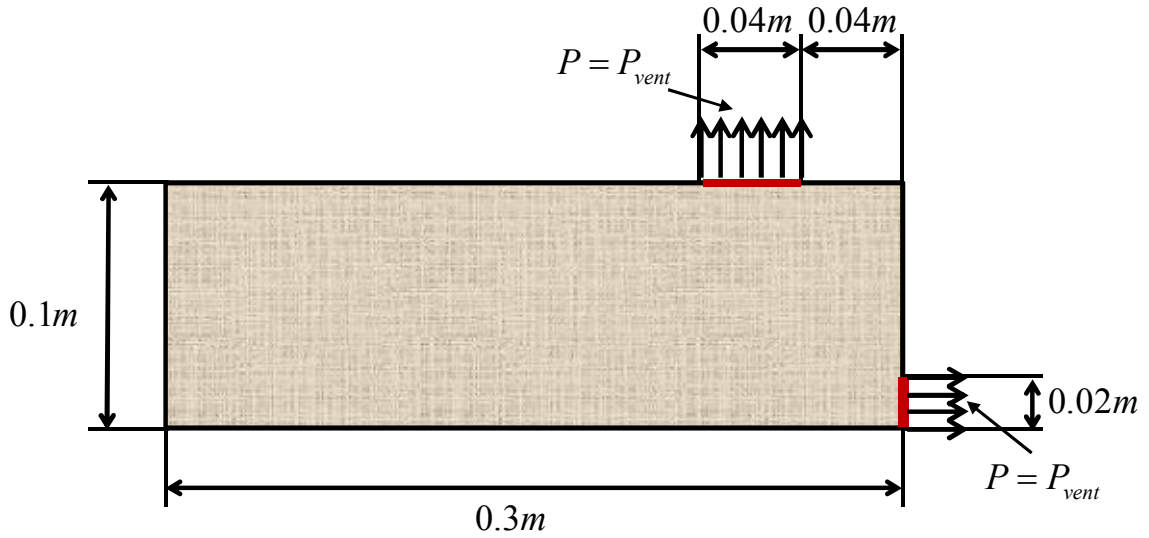


**Figure 3.31** Global boundary conditions for the part

To simulate the evolution of pressure and other parameters, one should solve the continuity equation. One can start the solution with

$$\frac{\partial}{\partial t}(\rho h dx dy) + \nabla \cdot (\rho \vec{u} h dx dy) = \left[ \frac{\partial}{\partial t}(\rho h) + \nabla \cdot (\rho h \vec{u}) \right] dx dy = 0 \quad (3.78)$$

where  $dV = dx dy dz$ . Thickness ( $h$ ) corresponds to  $dz$ ;  $dx$  and  $dy$  are length and width of the part, respectively. In this case,  $dx$  and  $dy$  are constants. We can drop  $dx$  and  $dy$  from Equation (3.78) and re-write it as

$$\frac{\partial}{\partial t}(\rho h) + \nabla \cdot (\rho h \vec{u}) = 0 \quad (3.87)$$



Fluid is incompressible, so  $\rho$  is constant and we can re-write Equation (3.87) as

$$\frac{\partial}{\partial t}(\rho h) + \nabla \cdot (\rho h \bar{u}) = \rho \left[ \frac{\partial h}{\partial t} + \nabla \cdot (h \bar{u}) \right] = 0 \quad (3.88)$$

Since  $\rho$  is constant and right-hand side of Equation (3.88) is zero, one can drop  $\rho$  term and the equation becomes

$$\frac{\partial h}{\partial t} + \nabla \cdot (h \bar{u}) = 0 \quad (3.89)$$

Utilizing chain rule for time derivative term in Equation (3.89), it can be written as

$$\frac{\partial h}{\partial P} \frac{\partial P}{\partial t} + \nabla \cdot (h \bar{u}) = 0 \quad (3.90)$$

where  $\frac{\partial h}{\partial P}$  can be calculated by taking derivative of Equation (3.71) with respect to  $P$ , and it yields

$$\frac{\partial h}{\partial P} = \frac{(8)(0.450)(19.42)}{2540} \frac{1}{\left( \ln \left( \frac{P_c}{2.04} \right) \right)^2} \frac{1}{P_c} \quad (3.91)$$

As discussed in Section 3.2, the system of equations to be solved is in the form of  $[C]\{P\} = \{F\}$  for the solution of pressure at the instant of mold filling.  $\{F\}$  is the load vector and it is zero everywhere except along the injection and ventilation boundaries; and it can be calculated using Equations (3.37) - (3.39). In this part of Case 3, evolution of pressure is solved using the governing equation

$$[\dot{C}]\{\dot{P}\} + [C]\{P\} = \{F\} \quad (3.92)$$

where  $[C]$  is the global stiffness matrix

$$C^{(e)} = \frac{h^{(e)}K^{(e)}}{\mu} \frac{1}{4A} \left( \begin{bmatrix} \beta_i^2 & \beta_i\beta_j & \beta_i\beta_k \\ \beta_i\beta_j & \beta_j^2 & \beta_j\beta_k \\ \beta_i\beta_k & \beta_j\beta_k & \beta_k^2 \end{bmatrix} + \begin{bmatrix} \delta_i^2 & \delta_i\delta_j & \delta_i\delta_k \\ \delta_i\delta_j & \delta_j^2 & \delta_j\delta_k \\ \delta_i\delta_k & \delta_j\delta_k & \delta_k^2 \end{bmatrix} \right) \quad (3.86)$$

is valid for this case due to variability of thickness and permeability.  $\dot{C}^{(e)}$  is usually called the capacitance matrix and it is calculated as follows

$$\dot{C}^{(e)} = \frac{\partial h^{(e)}}{\partial P} L = \frac{\partial h^{(e)}}{\partial P} \frac{A}{3} \begin{bmatrix} 1 & 0 & 0 \\ 0 & 1 & 0 \\ 0 & 0 & 1 \end{bmatrix} \quad (3.93)$$

where  $\frac{\partial h^{(e)}}{\partial P}$  is the derivative of thickness with respect to pressure at the centroid of the

element  $e$ .  $\frac{\partial h^{(e)}}{\partial P}$  is calculated as follows;

$$\frac{\partial h^{(e)}}{\partial P} = \frac{\left(\frac{\partial h}{\partial P}\right)_i + \left(\frac{\partial h}{\partial P}\right)_j + \left(\frac{\partial h}{\partial P}\right)_k}{3} \quad (3.94)$$

and derivative of thickness with respect to pressure at the nodes of the element is calculated using Equation (3.91). In Equation (3.93), lumped capacitance matrix, namely  $L$

$$L = \frac{A}{3} \begin{bmatrix} 1 & 0 & 0 \\ 0 & 1 & 0 \\ 0 & 0 & 1 \end{bmatrix} \quad (3.95)$$

for a triangular element is used where the capacitance is equally divided between three nodes as discussed in [29].

System of equations given below

$$[\dot{C}]\{\dot{P}\} + [C]\{P\} = \{F\} \quad (3.92)$$

is solved explicitly at each time increment using Euler Method. The approximation for  $\{\dot{P}\}$  is as follows

$$\{\dot{P}\}_n \cong \frac{\{P\}_{n+1} - \{P\}_n}{\Delta t} \quad (3.96)$$

where  $n = 1, 2, 3, \dots, N$  and  $\{P\}_n$  is the pressure at the  $n^{\text{th}}$  time increment. At the  $n^{\text{th}}$  time increment, we can re-write Equation (3.92) as

$$[\dot{C}]\{\dot{P}\}_n + [C]\{P\}_n = \{F\}_n \quad (3.97)$$

Substituting Equation (3.96) into Equation (3.97) yields

$$[\dot{C}] \frac{\{P\}_{n+1} - \{P\}_n}{\Delta t} + [C]\{P\}_n = \{F\}_n \quad (3.98)$$

which can be re-written as

$$[\dot{C}] \frac{\{P\}_{n+1}}{\Delta t} = \{F\}_n - [C]\{P\}_n + [\dot{C}] \frac{\{P\}_n}{\Delta t} \quad (3.99)$$

Multiplying both sides by  $\Delta t$  results in

$$[\dot{C}]\{P\}_{n+1} = \{F\}_n \Delta t - [C]\{P\}_n \Delta t + [\dot{C}]\{P\}_n \quad (3.100)$$

and re-writing Equation (3.100) gives

$$[\dot{C}]\{P\}_{n+1} = \{F\}_n \Delta t + (-[C]\Delta t + [\dot{C}])\{P\}_n \quad (3.101)$$

Right-hand side of the Equation (3.101) is known for any instant;  $\{P\}_{n+1}$  is directly calculated by utilizing the solution sequence for explicit algorithm given in [29]. The disadvantage for the explicit algorithm is that  $\Delta t$  should be chosen carefully to ensure the stability of the solution. Choosing smaller  $\Delta t$  gives finer results in terms of converging to the exact solution, but smaller  $\Delta t$  means more computation. On the contrary, larger  $\Delta t$  decreases the computational load; but very large  $\Delta t$  may cause the solution to become unstable. To achieve the minimum computational load without causing the solution to become unstable, critical time step size,  $\Delta t_{cr}$  is calculated. The procedure to determine  $\Delta t_{cr}$  is given in [29] and it is summarized below

$$\Delta t_{cr} = \frac{2}{\lambda_{max}} \quad (3.102)$$

where  $\lambda_{max}$  is the maximum eigenvalue of the system. Eigenvalues of the system,  $\lambda_i$ , are calculated as follows

$$\lambda_i = \frac{C_{ii}^*}{\dot{C}_{ii}^*} \quad (3.103)$$

where  $C_{ii}^*$  and  $\dot{C}_{ii}^*$  are calculated as follows

$$\{\Phi\}_i^T [C] \{\Phi\}_i = C_{ii}^* \quad (3.104)$$

$$\{\Phi\}_i^T [\dot{C}] \{\Phi\}_i = \dot{C}_{ii}^*$$

Here,  $\{\Phi\}_i$  are the eigenvectors of the system corresponding to eigenvalues  $\lambda_i$ .  $[C]$  is the global stiffness matrix and  $[\dot{C}]$  is the global capacitance matrix. Both global matrices are  $m \times m$  square matrices and thus  $i = 1, 2, 3, \dots, m$  in Equations (3.103) and (3.104).

The algorithm described between Equations (3.87) and (3.104) is used for simulating the evolution of pressure and other variables. Figures 3.32 and 3.33 show the pressure distribution at different instants. Figure 3.34 shows the pressure distribution at  $t=1200$  seconds (corresponding to the pressure distribution at the end of simulation) and as seen from that figure; the maximum pressure at this instant is slightly higher than  $10 \text{ kPa}$ . The expected behavior of pressure is to settle at  $10 \text{ kPa}$  at steady state, which is equal to the pressure at ventilation ports. To be more accurate about the settling time, four points, namely A, B, C, and D are marked as seen in Figure 3.35, and evolution of pressure at these four points is recorded throughout the simulation. Figure 3.36 shows the evolution of pressure at these four points. As seen from that figure, pressure settles at all these four points around  $t = 1000 \text{ s}$ , which also shows that result is in agreement with the pressure distribution in Figure 3.34.

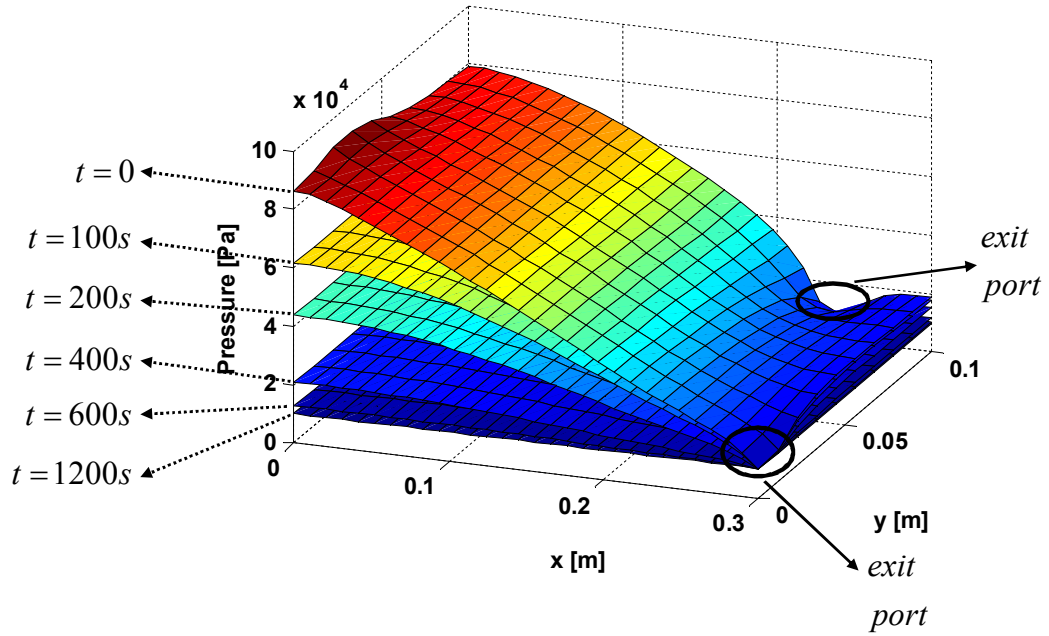


Figure 3.32 Pressure distribution at different instants

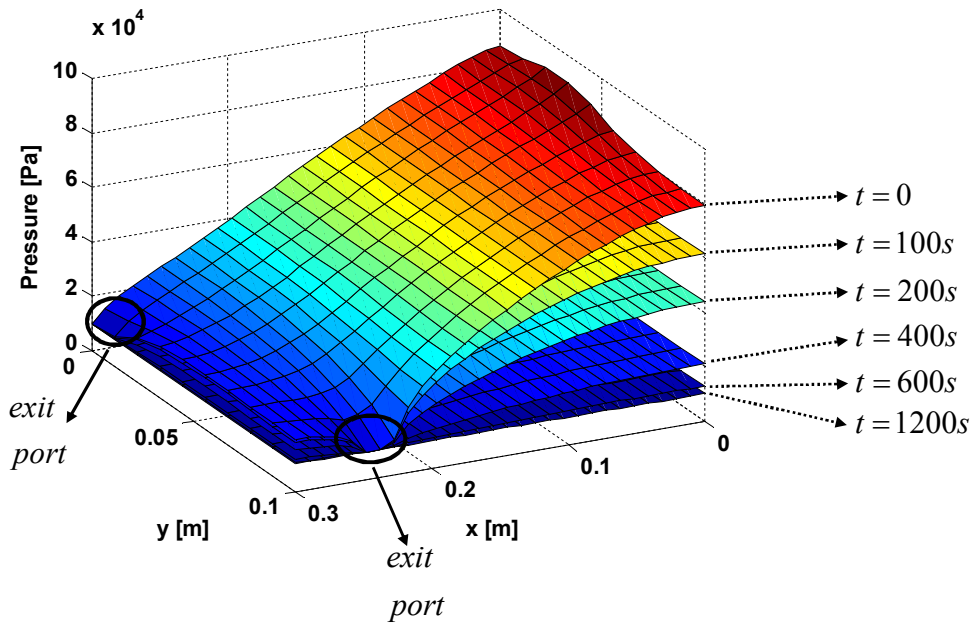


Figure 3.33 Pressure distribution at different instants from another angle

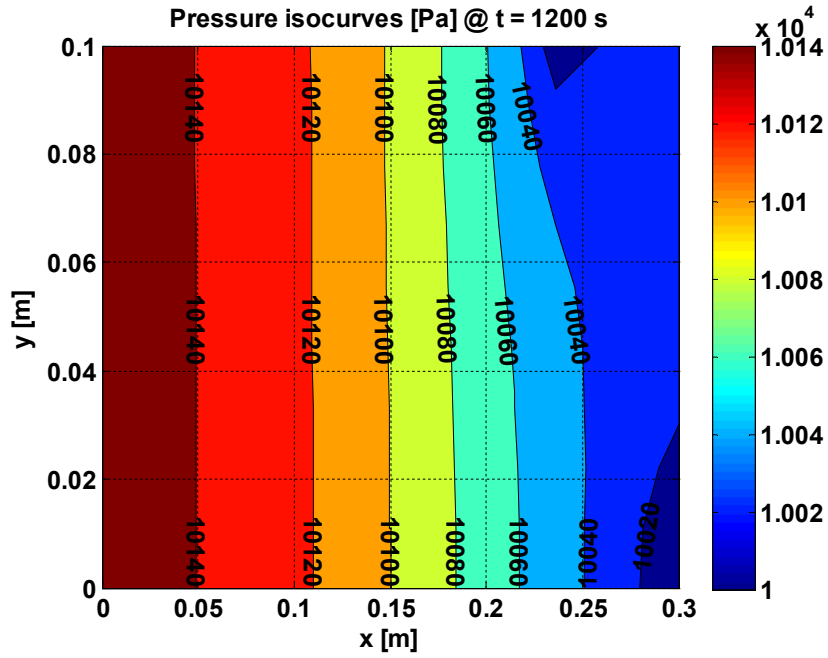


Figure 3.34 Pressure distribution in the mold at  $t = 1200$  s

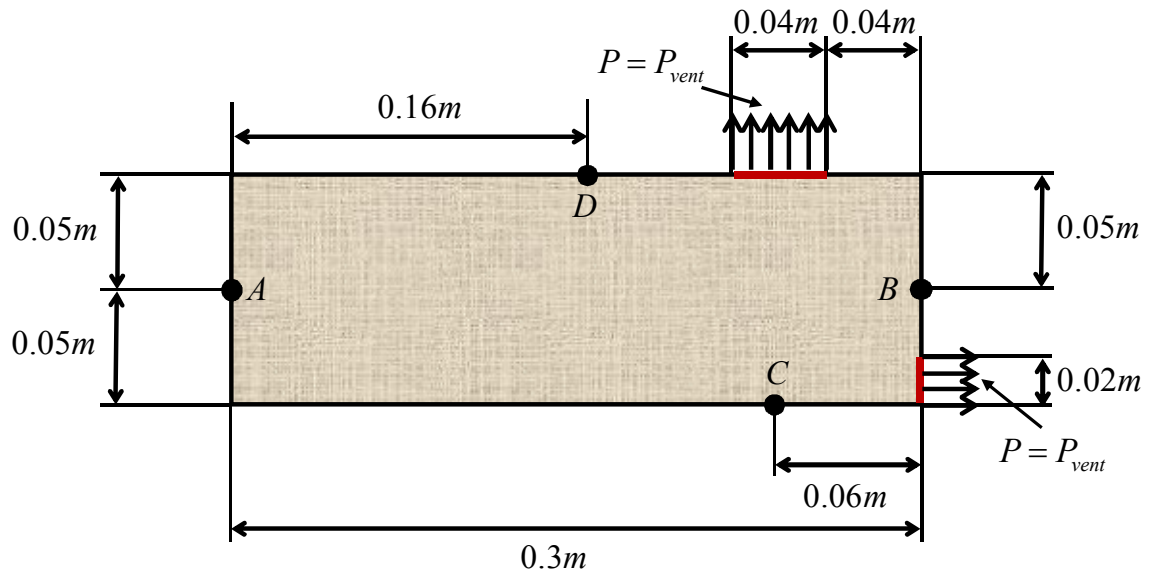
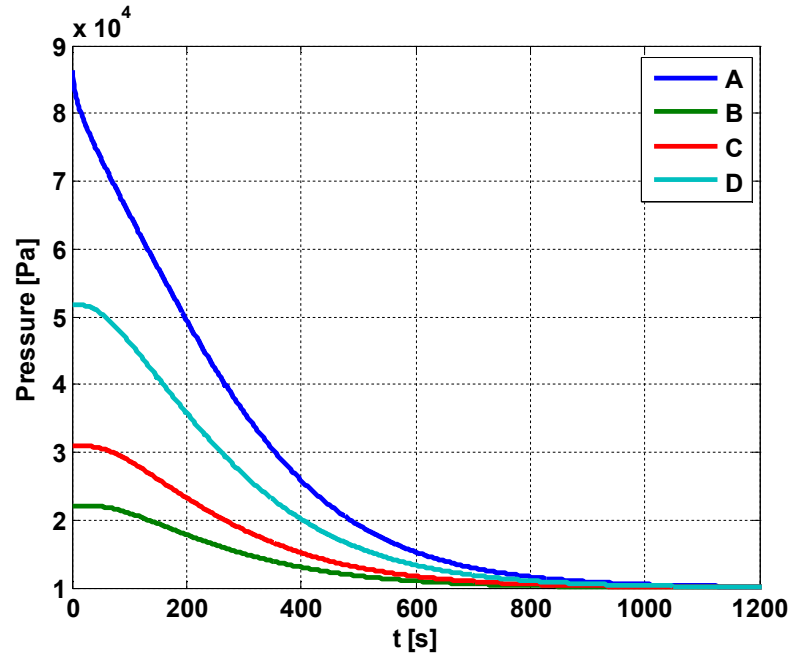


Figure 3.35 Positions of A, B, C, and D points



**Figure 3.36** Evolution of pressure at A, B, C, and D points

Bleeding is performed in order to decrease the thickness variation in the part by ejecting the excess resin through ventilation ports. In other words, volume of resin in the mold decreases until settling, which occurs around  $t = 1000$  s.  $V_{mold}$  in Figure 3.37 is the volume of the mold and it settles about  $t = 1000$  s, which is in agreement with our expectation as discussed earlier.  $V_{out}$  shows the total amount of resin leaving the mold and increases until about  $t = 1000$  s. There is no inlet port in this case, so there is no resin entering the system. Thus, we expect that sum of the volume of resin leaving the mold and volume remaining in the mold should be constant (considering the global conservation of mass)

$$V_{mold} + V_{out} = V_{tot} = \text{constant} \quad (3.105)$$



$V_{tot}$  is shown in Figure 3.37 and in Figure 3.38 in more detail for 300 elements. As seen in Figure 3.38, the total volume changes though it is expected to be constant. To discover the source of this error, the simulation is repeated for 600, and 1200 elements. In Figure 3.39, percentage errors for 300, 600, and 1200 elements are shown. As seen from the figure, error decreases as element number increases, and this indicates that error is attributed to linearization of pressure, thickness, and permeability inside the elements during discretization. Also, it should be noted that the problem of mass conservation is reported in [33, 34] to be a common issue in this numerical approach.

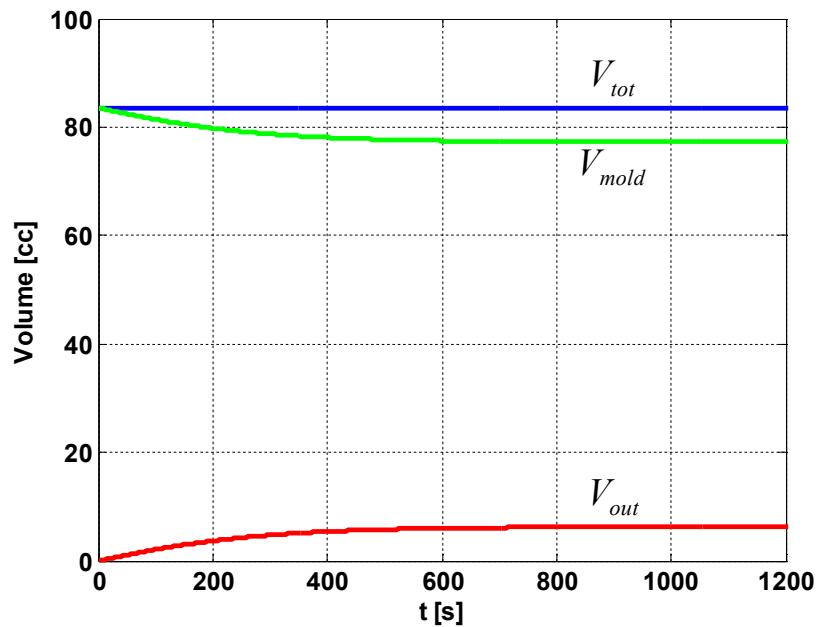


**Figure 3.37** Change of volume in and out of the mold by using 300 elements

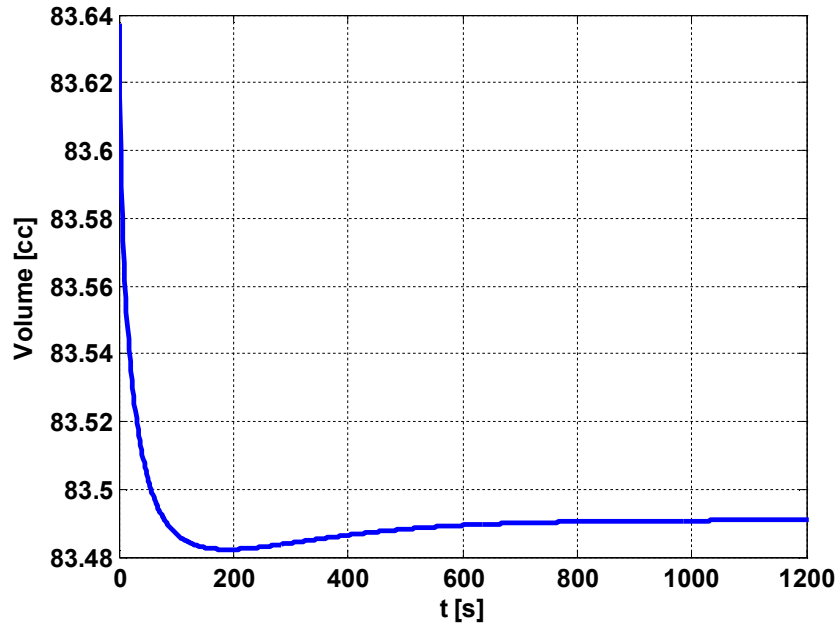


Figure 3.38 Change of total volume by using 300 elements

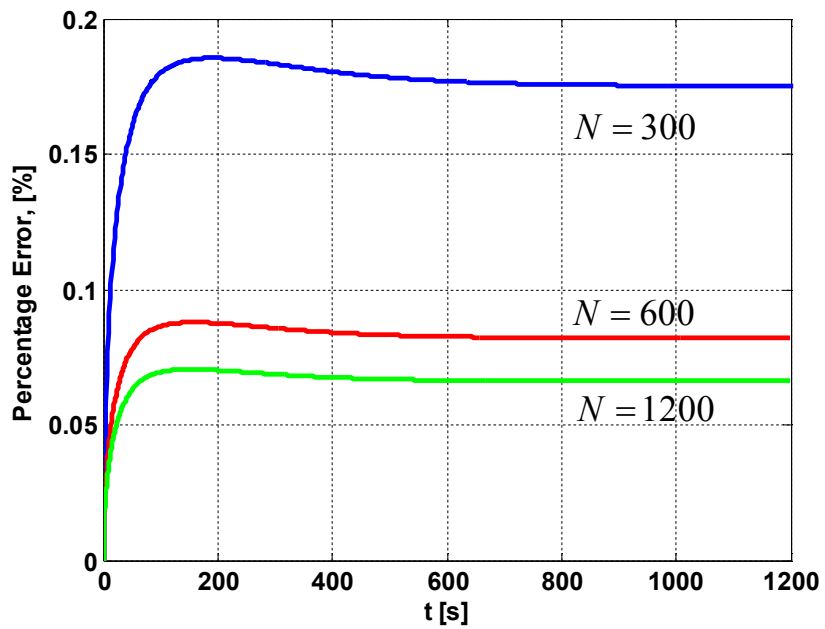


Figure 3.39 Percentage error by using 300, 600, and 1200 elements

**3.4.3 Case 3-c: Steady state solution for new boundary conditions**

In this part of the study, steady state solution is obtained for boundary conditions shown in Figure 3.31. There is no inlet port in this case meaning that solution of this case corresponds to the end of bleeding which is explained in the previous case. Since pressure in the exit ports is equal to each other as seen in Figure 3.31, we expect the pressure to be equal everywhere in the mold at steady state as  $t \rightarrow \infty$ . Pressure distribution for these boundary conditions is shown in Figure 3.40; and pressure is equal to pressure at exit ports, 10 kPa, which is in agreement with our expectation. Solution is numerical, so there is a minor difference between pressure values at different nodes and the difference is in the order of  $10^{-12}$  while machine epsilon is  $2.2204 \times 10^{-16}$ . To further check the correctness of the algorithm we can compare the volume of the mold for the steady case and for the end of the previous case (at  $t = 1200$  s). Volume at the end of previous case is calculated as 77.211 cc. In this steady case, the volume is calculated as 77.210 cc meaning that the variation is 0.001%. The minor variation is due to the difference in pressure distributions between at the end of Case 3-b and this case (Case 3-c) which are shown in Figures 3.34 and 3.40 respectively.

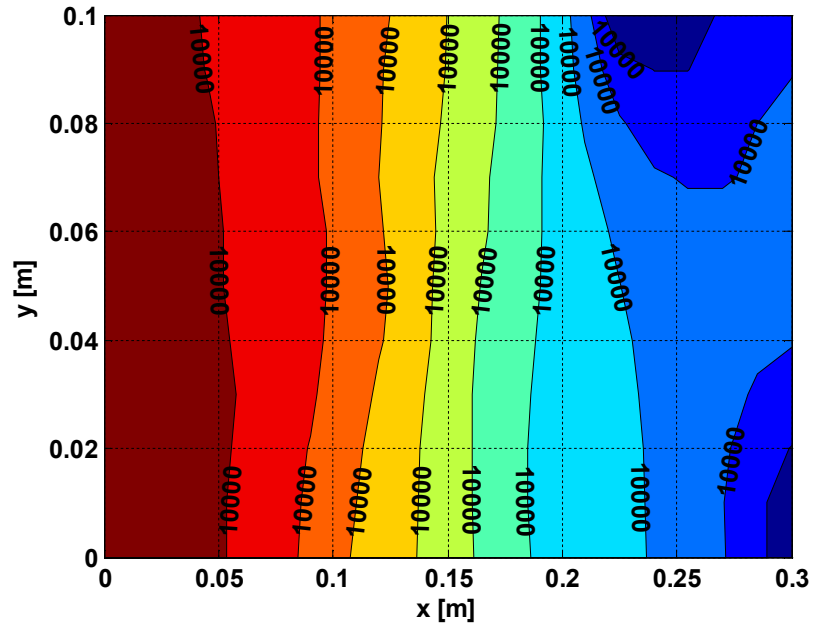


Figure 3.40 Pressure distribution in the mold

## Chapter 4

### SUMMARY AND CONCLUSIONS

In the first part of this study (Cases 1 and 2), pressure distribution at the end of mold filling ( $t = t_{fill}$ ) was simulated for different cases. Simulations were repeated for different boundary conditions. Global mass conservation was used to validate the model, and in all of these cases, mass was conserved with accuracies which are approximately equal to machine accuracy, i.e. inlet and exit flow rates were equal. In some of these cases, results were also compared with analytical solutions of pressure distribution and flow rates for 1D flow. In those cases, pressure distribution curves overlapped with pressure distribution of analytical solution and flow rates were equal for numerical and analytical solutions.

In the second part (Case 3), post-filling of VARTM was studied. Material characterization data obtained in our research laboratory, permeability data in [15] and compaction data in [18], were incorporated into FEM model. Steady solution of pressure distribution was obtained for end of mold-filling. Then, boundary conditions were updated (simulating a control action in VARTM) and evolution of pressure, thickness and permeability were recorded for a sufficient amount of time. The expected result was the convergence of solution to steady solution due to the new boundary conditions, and yes, the solution converged to a steady state solution as expected. Global mass conservation was also checked to validate the solution. Mass conservation had an error of 0.2% even by using a coarse mesh with 300 elements. The error could be further decreased by increasing number of elements, which showed that error was due to the linear approximation of variables ( $h$ ,  $K$ , and  $P$ ) in an element.

Future work of this study is explained in this part. In this study, solution at the end of the mold filling and post-filling are done. However, flow propagation should also be

modeled to have a complete model of VARTM. The only element type used in FEM is linear triangular element, meaning that any function is distributed linearly in the element. To have a more realistic model, other element types, i.e. quadratic triangular elements (or six node triangular elements) should also be incorporated. Time integration is modeled using an explicit time-marching scheme which is conditionally stable. If time increment is selected to be higher than a critical value, non-physical oscillations occur, and the solution does not converge. Using an implicit method may increase the computational load, but stability of the solution will be ensured. Verifying the simulation results by comparing the results with experiments and repeating the simulations for non-rectangular mold geometries also remain as a matter of future work.

## BIBLIOGRAPHY

1. Yenilmez, B. and E.M. Sozer, *Compaction of e-glass fabric preforms in the Vacuum Infusion Process, A: Characterization experiments*. Composites Part A: Applied Science and Manufacturing, 2009. **40**(4): p. 499-510.
2. Gutowski, T.G., T. Morigaki, and Zhong Cai, *The Consolidation of Laminate Composites*. Journal of Composite Materials, 1987. **21**(2): p. 172-188.
3. H. Magnus Andersson, T.S.L., B. Rikard Gebart,, *Numerical model for vacuum infusion manufacturing of polymer composites*. International Journal of Numerical Methods for Heat & Fluid Flow, 2003. **13**(3): p. 383 - 394.
4. Robitaille, F. and R. Gauvin, *Compaction of textile reinforcements for composites manufacturing. III: Reorganization of the fiber network*. Polymer Composites, 1999. **20**(1): p. 48-61.
5. Joubaud, L., V. Achim, and F. Trochu, *Numerical simulation of resin infusion and reinforcement consolidation under flexible cover*. Polymer Composites, 2005. **26**(4): p. 417-427.
6. Kelly, P.A., *A viscoelastic model for the compaction of fibrous materials*. Journal of The Textile Institute, 2011. **102**(8): p. 689-699.
7. Kelly, P.A., R. Umer, and S. Bickerton, *Viscoelastic response of dry and wet fibrous materials during infusion processes*. Composites Part A: Applied Science and Manufacturing, 2006. **37**(6): p. 868-873.
8. Govignon, Q., S. Bickerton, and P.A. Kelly, *Simulation of the reinforcement compaction and resin flow during the complete resin infusion process*. Composites Part A: Applied Science and Manufacturing, 2010. **41**(1): p. 45-57.
9. Advani S.G., S.E.M., *Process modeling in composites manufacturing*. 2nd ed. 2010: Marcel Dekker Inc.
10. Correia, N.C., et al., *Analysis of the vacuum infusion moulding process: I. Analytical formulation*. Composites Part A: Applied Science and Manufacturing, 2005. **36**(12): p. 1645-1656.
11. Gebart, B.R., *Permeability of Unidirectional Reinforcements for RTM*. Journal of Composite Materials, 1992. **26**(8): p. 1100-1133.
12. M. V. Brusckhe, S.G.A., *Flow of generalized Newtonian fluids across a periodic array of cylinders*. Journal of Rheology, 1993. **37**(3): p. 479-498.
13. Yenilmez, B., M. Senan, and E. Murat Sozer, *Variation of part thickness and compaction pressure in vacuum infusion process*. Composites Science and Technology, 2009. **69**(11-12): p. 1710-1719.
14. Nedanov, P.B. and S.G. Advani, *A Method to Determine 3D Permeability of Fibrous Reinforcements*. Journal of Composite Materials, 2002. **36**(2): p. 241-254.
15. Sarioğlu, A., *Permeability Measurement Experiments for Fabric Preform Using LCM Processes*, in *Mechanical Engineering*. 2012, Koc University: Istanbul.
16. Yenilmez, B. and E.M. Sozer, *Compaction of E-glass fabric preforms in the vacuum infusion process: (a) use of characterization database in a model and (b) experiments*. Journal of Composite Materials, 2012. **To be published**.

## BIBLIOGRAPHY

---

17. Haboğlu, M.R., *Strain rate controlled compaction characterization of e-glass fabrics and investigation of the effects of process parameters on the results*, in *Mechanical Engineering*. 2012, Koc University: Istanbul.
18. Yenilmez, B., *Vacuum Infusion (VI) Process Modeling and Material Characterization with Viscoelastic Compaction Models*, in *Mechanical Engineering*. 2012, Koc University: Istanbul.
19. Yenilmez, B., et al., *Minimizing Thickness Variation In The Vacuum Infusion (VI) Process*. *Advanced Composite Letters*, 2011. **20**(06): p. 161-172.
20. Yalçınkaya, M.A., *Effect of Part Thickness Variation on the Mold Filling in Vacuum Infusion Process*, in *Mechanical Engineering*. 2012, Koc University: Istanbul.
21. Akyol, T., *Minimizing Thickness Variation in the Vacuum Infusion (VI) Process*, in *Mechanical Engineering*. 2012, Koc University: Istanbul.
22. Rao, H.S.G., *Finite Element Method Vs. Classical Methods*. 2007: New Age International (P) Limited.
23. Chung, T.J., *Computational Fluid Dynamics*. 2010: Cambridge University Press.
24. Desai, Y.M., *Finite Element Method With Applications in Engineering*. 2011: Pearson Education India.
25. Simacek, P., et al., *Post-filling flow in vacuum assisted resin transfer molding processes: Theoretical analysis*. *Composites Part A: Applied Science and Manufacturing*, 2009. **40**(6–7): p. 913-924.
26. Zienkiewicz, O.C., Taylor, R.L., *The Finite Element Method*. Vol. 1-The Basis. 2000: Elsevier.
27. Reddy, J.N., *An Introduction to the Finite Element Method*. 3rd ed. 2006, New York: McGraw-Hill.
28. Moaveni, S., *Finite Element Analysis: Theory and Applications with ANSYS*. 2nd ed. 2003: Prentice Hall.
29. Huebner, K.H., et al., *The Finite Element Method for Engineers*. 4th ed. 2001: John Wiley & sons.
30. George, P.L., *Automatic Mesh Generation — Application to Finite Element Methods*. 1991: Wiley.
31. Davis, T.A., *Direct Methods for Sparse Linear Systems*. *Fundamentals of Algorithms*. 2006. 228.
32. Bickerton, S., et al., *Fabric structure and mold curvature effects on preform permeability and mold filling in the RTM process. Part II. Predictions and comparisons with experiments*. *Composites Part A: Applied Science and Manufacturing*, 2000. **31**(5): p. 439-458.
33. Samir, J., J. Echaabi, and M. Hattabi, *Numerical algorithm and adaptive meshing for simulation the effect of variation thickness in resin transfer molding process*. *Composites Part B: Engineering*, 2011. **42**(5): p. 1015-1028.
34. Phelan, F.R., *Simulation of the injection process in resin transfer molding*. *Polymer Composites*, 1997. **18**(4): p. 460-476.



**VITA**

BARIŞ ÇAĞLAR was born in Istanbul, Turkey on March 15, 1987. He received his B.Sc. degree in Mechanical Engineering from Koc University, Istanbul in 2010. Since then, he has enrolled in the M.Sc program in Mechanical Engineering at Koc University, Istanbul with full TUBITAK scholarship, as both a teaching and research assistant. His most recent thesis, “Post-filling Modeling of Vacuum Assisted Resin Transfer Molding” acts as a complement to his numerous related works in the field. He published a journal paper in *Advanced Composites Letters*. Upon completion of his Masters Degree, Barış plans to study further, with a view to achieving a Ph.D.

**APPENDIX A**  
**Thickness and Permeability Distributions for Studied Cases**

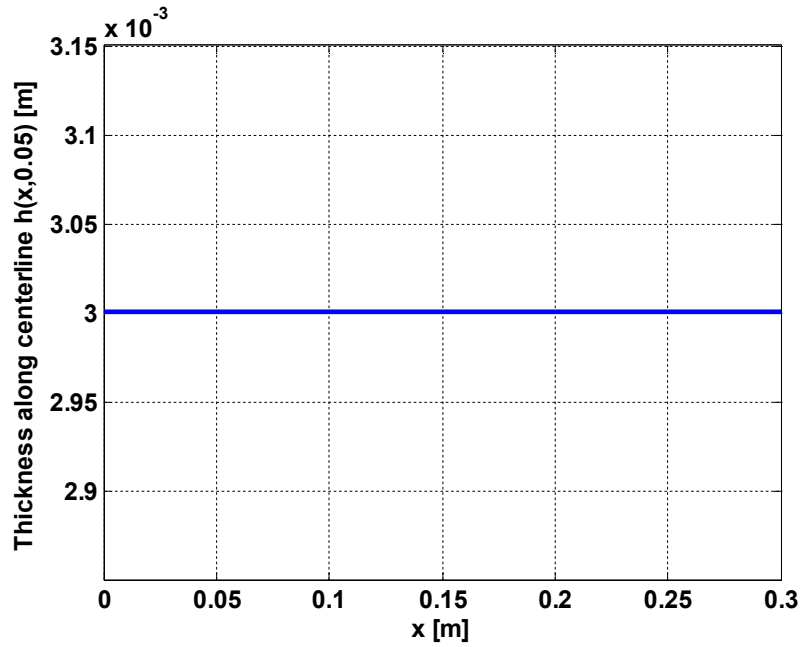


Figure A.1 Input thickness (in [m]) distribution along  $y = 0.05$ m for Cases 1-a and 1-b

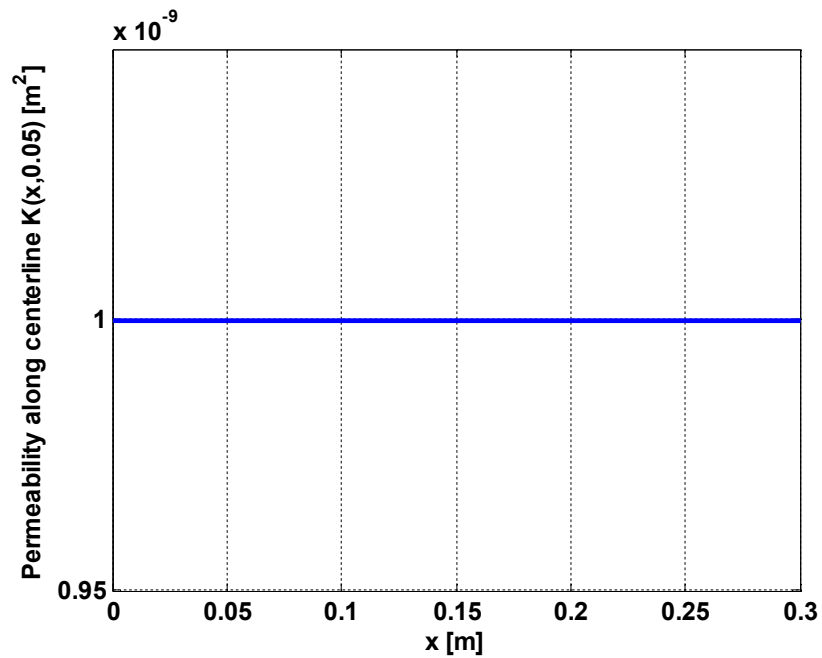


Figure A.2 Input permeability (in [ $m^2$ ]) distribution along  $y = 0.05$ m for Cases 1-a and 1-b

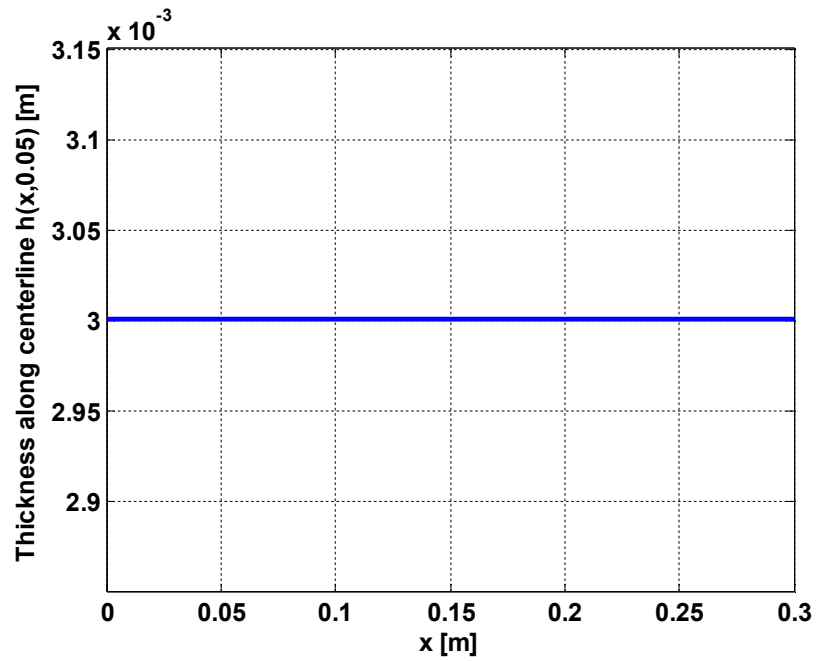


Figure A.3 Input thickness (in [m]) distribution along  $y = 0.05$ m for Cases 2-a and 2-b

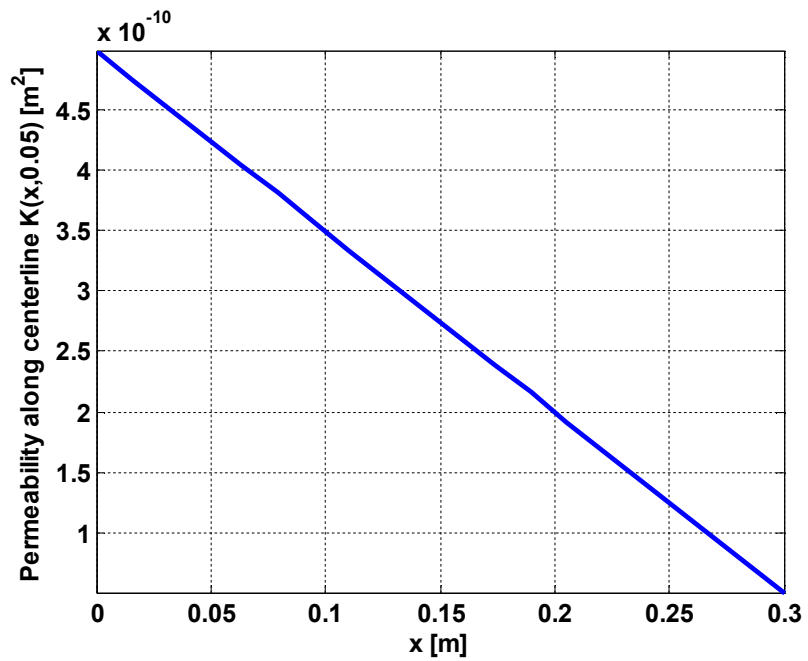


Figure A.4 Input permeability (in [m<sup>2</sup>]) distribution along  $y = 0.05$ m for Cases 2-a and 2-b

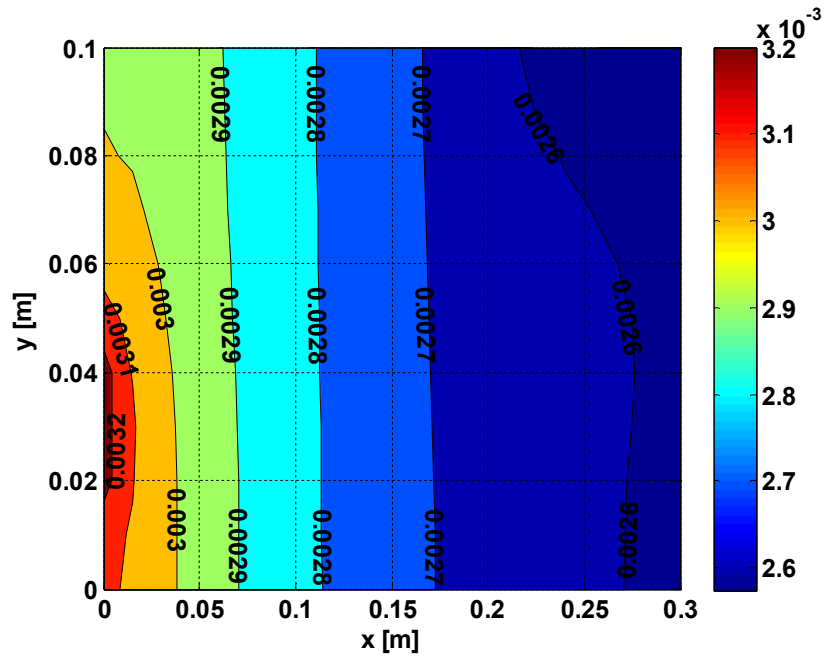


Figure A.5 Simulated thickness (in [m]) distribution for Case 3-a

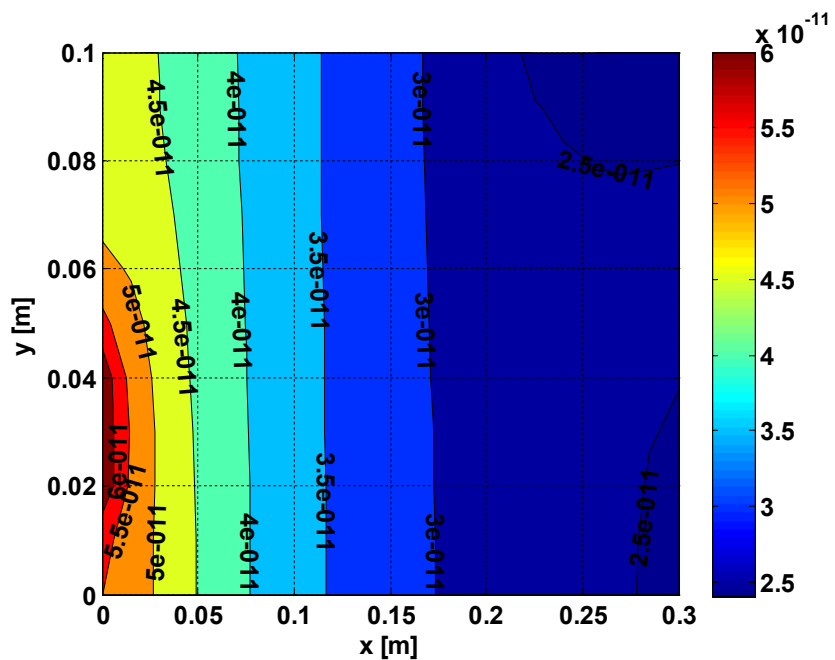
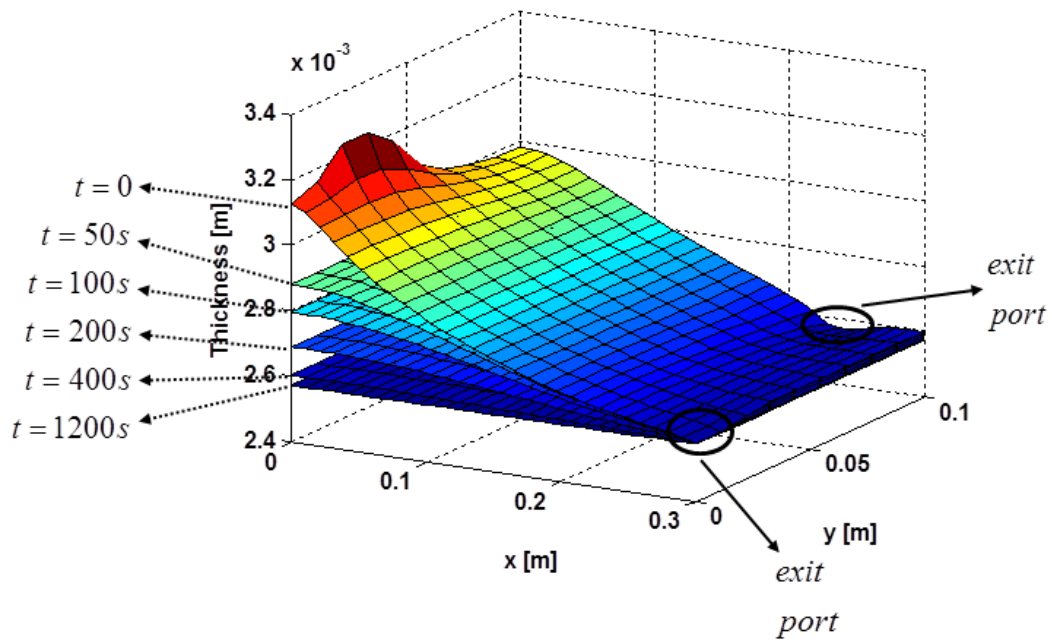
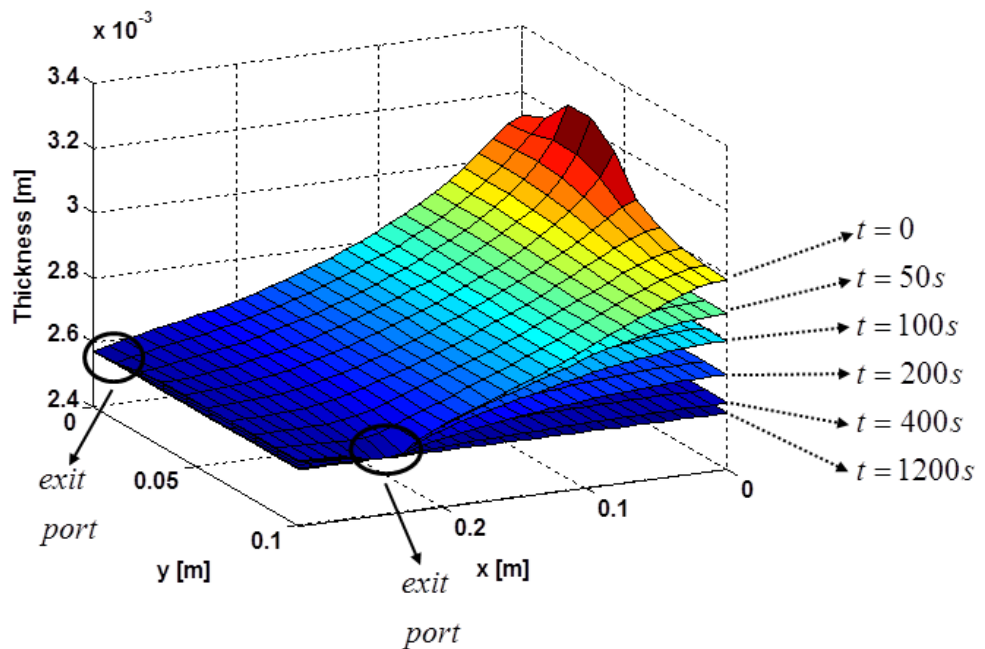


Figure A.6 Simulated permeability (in [m<sup>2</sup>]) distribution for Case 3-a



**Figure A.7** Simulated thickness (in [m]) distribution at different instants for Case 3-b



**Figure A.8** Simulated thickness (in [m]) distribution at different instants for Case 3-b from another angle

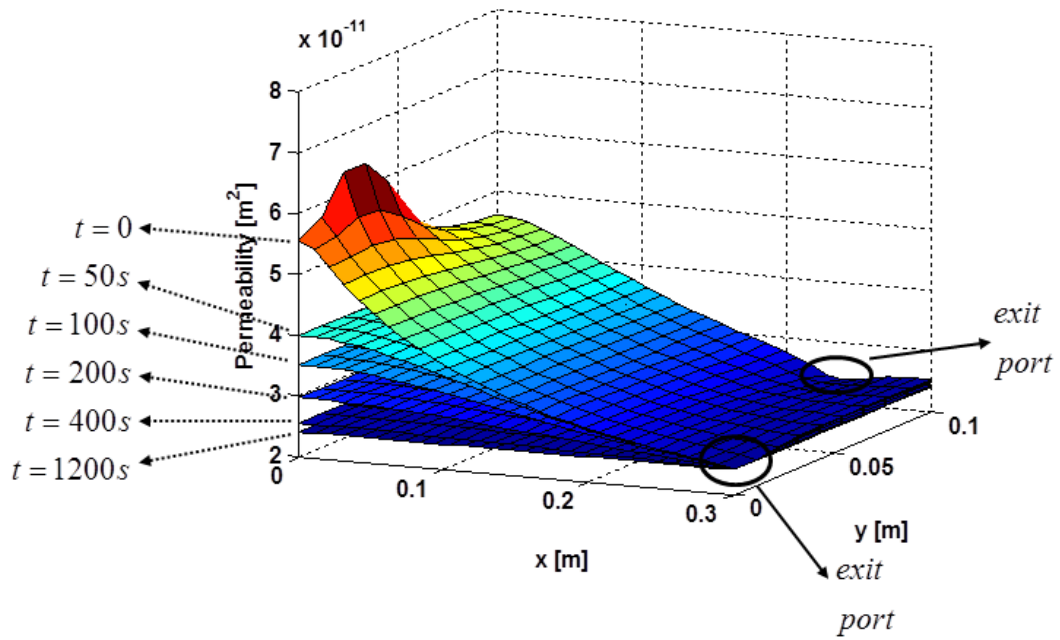


**Figure A.9** Simulated permeability (in  $\text{m}^2$ ) distribution at different instants for Case 3-b

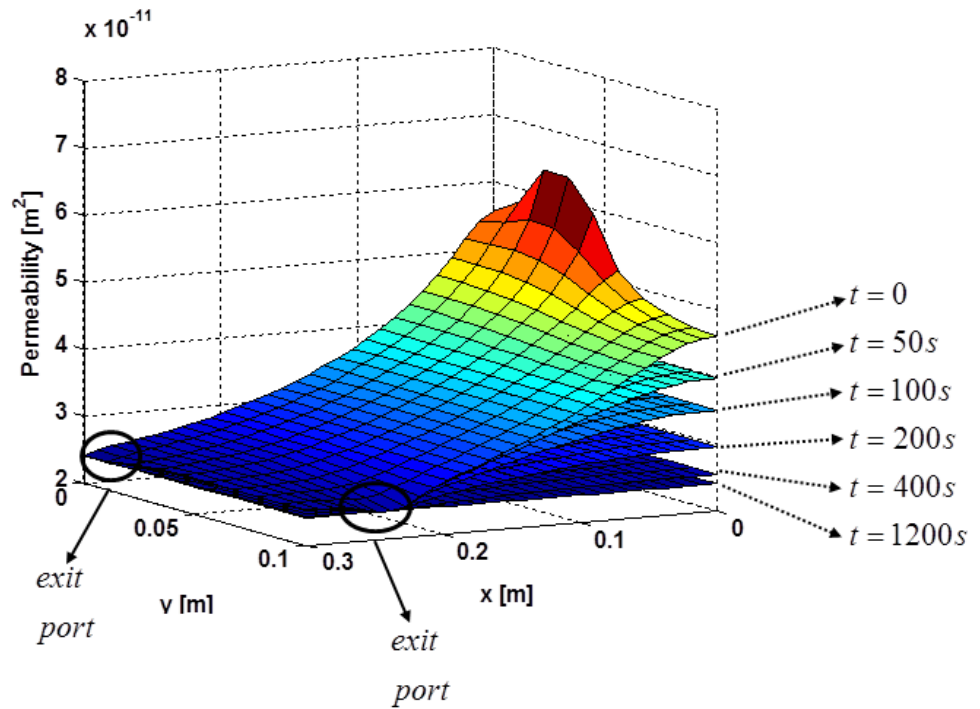


**Figure A.10** Simulated permeability (in  $\text{m}^2$ ) distribution at different instants for Case 3-b from another angle

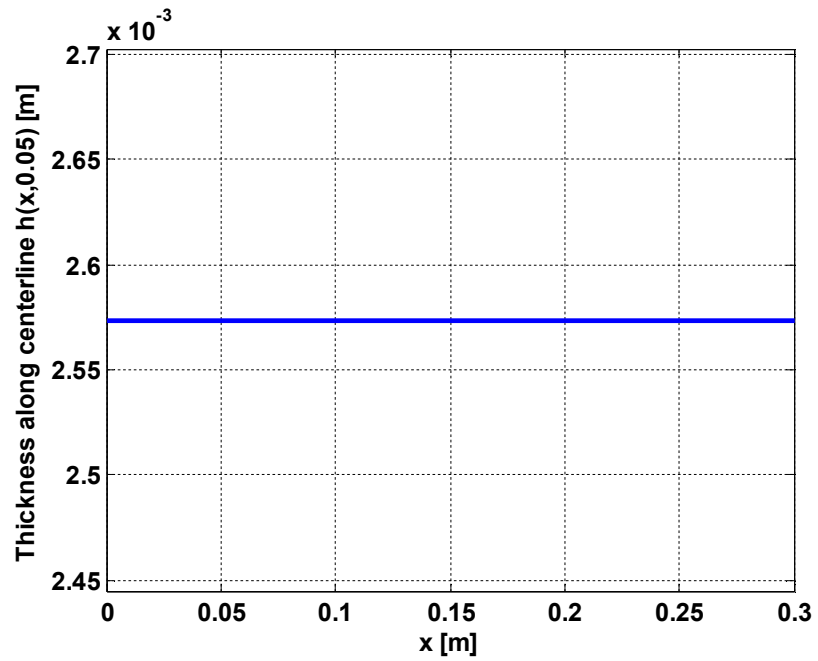


Figure A.11 Simulated thickness (in [m]) distribution along  $y = 0.05$ m for Case 3-c

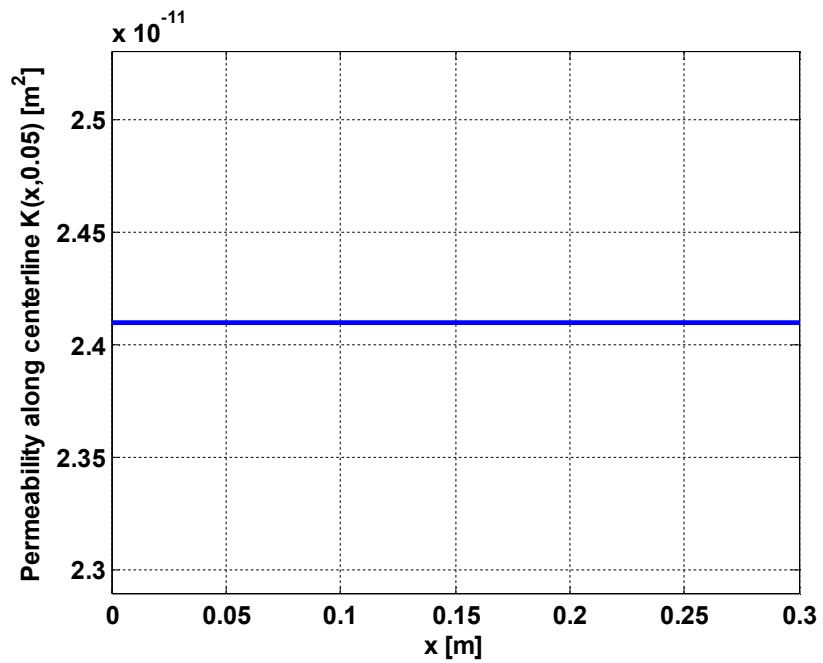


Figure A.12 Simulated permeability (in [m<sup>2</sup>]) distribution along  $y = 0.05$ m for Case 3-c



**APPENDIX B**  
**MATLAB Code for Solution of Steady Cases**

**Steady.m**

```
function Steady()
%Functions used in this code are constructed to solve Case 3-a
%and they can be modified to solve
%other cases (Case 1, Case 2, and Case 3-c))

clear all
close all
clc
%%SOLUTION OF Case 3-a

%%VARIABLES
%Lx: length of mold
%Ly: width of mold
%Nx: number of rectangles in x direction (rectangles are divided
%diagonally to form triangular elements)

%Ny: number of elements in y direction
%meshp, meshe, mesht: see help of poimesh for details
%node_x: coordinates of nodes in x direction
%node_y: coordinates of nodes in y direction
%node_num: number of nodes
%elem_conn: element connectivity matrix, contains the indices of the
%corner points of triangular element

%elem_num: number of elements
%p: array of nodal pressures [Pa]
%P_inj: pressure at injection port(s)
%P_vent: pressure at ventilation port(s)
%mu: viscosity [Pa.s]
%Inj_index: indices of nodes at injection port(s)
%Ven_index: indices of nodes at ventilation port(s)
%Boun_index: indices of nodes at injection and ventilation ports
%Boun_values: pressure at nodes at injection and ventilation ports
%area: array of areas of elements
%S_n: see Equation (2.10) for details
%C: global stiffness matrix
%h_node: thickness of nodes
%Knxx = Knyy (isotropic fabric): permeability of nodes
%f: load vector (RHS of C*P = F)
%p_prev: nodal pressures at previous iteration
```

## APPENDIX B

---

```
load geometry %Geometry file is loaded from current folder, it is created
%using pdetool it contains two matrices (boun, geom)

Lx = 0.3;
Ly = 0.1;
Nx = 30;
Ny = 20;

[meshp, meshe, mesht] = poimesh(geom,Nx,Ny); %mesh generation with
%regular triangular elements
%(use initmesh for Delaunay triangulation algorithm)

figure
pdemesh(meshp, meshe, mesht) %displaying the meshed geometry

node_x = meshp(1,:);
node_y = meshp(2,:);
node_num = size(meshp,2);

elem_conn = mesht(1:3,:);
elem_num = size(mesht,2);

p = ones(node_num,1);

P_inj = 90e3;
P_vent = 10e3;
mu = 0.1;

Inj_index = find(node_x == 0);%indices corresponding to injection port
are
%found, in this case left side of the mold geometry

Ven_index = find(node_x == Lx ); %indices corresponding to injection port
%are found, in this case left side of the mold geometry

Boun_index = [Inj_index, Ven_index]';
Boun_values = [P_inj+0*Inj_index, P_vent+0*Ven_index ]';

area = zeros(1,elem_num);
S_n = zeros(elem_num,3,3);

for i = 1:elem_num
    %this for loop is for generating the interpolation functions
    %(see Section 2.1)

    %n1, n2, n3: indices of corner points of element
    %x1, x2, x3: global coordinates of corner points in x direction
    %y1, y2, y3: global coordinates of corner points in x direction
    %a1, a2, a3: see Equation (2.11)
    %b1, b2, b3: see Equation (2.11)
    %c1, c2, c3: see Equation (2.11)
```

## APPENDIX B

---

```
n1 = elem_conn(i,1);
n2 = elem_conn(i,2);
n3 = elem_conn(i,3);

x1 = node_x(n1);    y1 = node_y(n1);
x2 = node_x(n2);    y2 = node_y(n2);
x3 = node_x(n3);    y3 = node_y(n3);

area(i) = 0.5*(x1*(y2-y3)+x2*(y3-y1)+x3*(y1-y2));

a1 = x2*y3-x3*y2;    b1 = y2-y3; c1 = x3-x2;
a2 = x3*y1-x1*y3;    b2 = y3-y1; c2 = x1-x3;
a3 = x1*y2-x2*y1;    b3 = y1-y2; c3 = x2-x1;

S_n(i,(:, :)) = (0.5/area(i)) * [ a1 b1 c1 ; ...
    a2 b2 c2 ; ...
    a3 b3 c3 ];
end

p_prev = inf;

while norm(p-p_prev)>1e-3
    %this iterative loop solves the pressure until norm of two iterations
    %is smaller than 0.001. pressure values are updated by calculating
    %the thickness and permeability at each node and solving P = C\F
    after
        %modifying C with new thickness and permeability values

        C = sparse(zeros(node_num,node_num));

        h_node = Hfun(p);%thickness at nodes are calculated by using function
        %Hfun described at the end of code

        Knxx = Kfun(h_node);%permeability at nodes are calculated by using
        %function Kfun described at the end of code

        Knyy = Knxx;%isotropic fabric

        for k = 1:elem_num
            %this for loop constructs the stiffness matrix for each element
            %n: index of element
            %Kxx = Kyy: permeability at the centroid of the element
            %(see Equation (3.52))

            %h: thickness at the centroid of the element

            n = elem_conn(k, :);
            Kxx = mean(Knxx(n));
            Kyy = mean(Knyy(n));
```

## APPENDIX B

---

```
h = mean(h_node(n));

dx = 2 * area(k) * S_n(k,:,2);
%dx'*dx gives 3x3 matrix of beta terms in Equation (3.86)
%it can be used for Case 1 and Case 2 as well

dy = 2 * area(k) * S_n(k,:,3);
%dy'*dy gives 3x3 matrix of gamma terms in Equation (3.86)
%it can be used for Case 1 and Case 2 as well

C(n,n) = C(n,n) + ( ( dx'* dx * Kxx + dy'* dy * Kyy ) * h ...
) / 4 / area(k) / mu ;
%stiffness matrix of element is added to global stiffness matrix

end

%lines below is for modifying the load vector in a way that only
%indices corresponding to injection or ventilation nodes are non-zero
%procedure is explained in detail in
%Programing the Finite Element Method with Matlab
%by Jack Chessa

f = zeros(node_num,1);
bcwt=trace(C)/node_num;
f=f-C(:,Boun_index)*Boun_values;
C(:,Boun_index)=0;
C(Boun_index,:)=0;
C(Boun_index,Boun_index)=bcwt*speye(length(Boun_index));
f(Boun_index)=bcwt*Boun_values;

p_prev = p;

p = C\f;
%solution of pressure
end

%workspace is saved to use for post-processing and to use nodal pressures
%as initial conditions for evolution of solution with time
save steady

function [h] = Hfun(P)
%compaction model used in Case 3-a (see Equation (3.71))
h = (8*450/2540)*(19.42./log((1e5-P)/2.04))/1000;

function [K] = Kfun(h)
%permeability model used in Case 3-a (see Equations (3.73) and (3.74))
Vf = (8*450/2540)./h/1000;
K= 2.7314e-9*exp(-8.59*Vf);
```

## APPENDIX C

## MATLAB Code for Evolution of Solution with Time

**Evolution.m**

```
function Evolution()

clear all
close all
clc
%%SOLUTION OF Case 3-b

%%VARIABLES
%Ven_index: indices of nodes at ventilation port(s) (loaded from
workspace)
%P_vent: pressure at ventilation port(s) (loaded from workspace)
%dt: time step size in seconds
%t: time in seconds
%t_fin: simulation will continue until time reaches to this value
%P_array: nodal pressures are saved to this matrix at desired time steps
%C: global stiffness matrix
%C_dot: global lumped mass matrix
%h_node: thickness of nodes
%dhdpn: derivative of thickness with respect to pressure
%(calculated at nodes)

%Knx = Knxy (isotropic fabric): permeability of nodes
%elem_num: number of elements (loaded from workspace)
%elem_conn: element connectivity matrix, contains the indices of the
%corner points of triangular element (loaded from workspace)

%S_n: see Equation (2.10) for details (loaded from workspace)

load steady
%solution of Case 3-a is loaded since nodal pressures will be used
%as initial condition and some of the other variables will be used as
well

dt =1e-5;%dt is initialized arbitrarily

Boun_index = Ven_index';%boundary conditions are modified here
%to correspond to closing of injection port
Boun_values = [P_vent+0*Ven_index]';

P_array = zeros(25000,node_num);
t_array = zeros(25000,1);
```

## APPENDIX C

---

```
t = 0;

t_fin = 2000;

while t<t_fin
    %this loop solves the pressure at nodes explicitly at each time step

    C = sparse(zeros(node_num,node_num));
    C_dot = sparse(zeros(node_num,node_num));

    h_node = Hfun(p);%thickness at nodes are calculated by using function
    %Hfun described at the end of code

    dhdpn = dHdPfun(p);%derivative of thickness with respect to pressure
    %at nodes. They are calculated by using function dHdPfun described
    %at the end of code

    Knxx = Kfun(h_node);%permeability at nodes are calculated by using
    %function Kfun described at the end of code

    Knyy = Knxx;

    for k = 1:elem_num
        %this for loop constructs the stiffness matrix for each element
        %n: index of element
        %Kxx = Kyy: permeability at the centroid of the element
        %(see Equation (3.52))

        %h: thickness at the centroid of the element
        %dhdp: derivative of thickness with respect to pressure at the
        %centroid of the element

        n = elem_conn(k,:);
        Kxx = mean(Knxx(n));
        Kyy = mean(Knyy(n));
        h = mean(h_node(n));
        dhdp = mean(dhdpn(n));

        dx = 2 * area(k) * S_n(k,:,2);
        dy = 2 * area(k) * S_n(k,:,3);

        C(n,n) = C(n,n) + ( ( dx'* dx * Kxx + dy'* dy * Kyy ) * h
...
        ) / 4 / area(k) / mu ;

        C_dot(n,n) = C_dot(n,n) + [1 0 0
        0 1 0
        0 0 1]*dhdp*area(k)/3;

    end

    %lines below is for time integration explained in detail
```

## APPENDIX C

---

```
%in The Finite Element Method for Engineers
%by Huebner et al.

R_bar = (-dt*C+C_dot)*p+dt*f; %see Equation (3.101) for details
dp = C_dot\R_bar - p;
p = p + dp;
p(Boun_index) = Boun_values;
f = ( C_dot*dp + C*p ) * dt;
%
%
t = t + dt;

check_num = 10;%dt is modified whenever the number of increments
%is a multiples of check_num, in this case 10

if mod(counter,check_num)==0
    %dt (time step size) is modified in the lines below using the
    %algorithm described between Eqautions (3.96) and (3.104)

    %lambda: array of eigenvalues
    %eVec: eigenvectors of the system
    %eVal: eigenvalues of the system. lambda and eVal are equal to
    %each other but both ways are used during calculations

    lambda = zeros(node_num,1);

    [eVec, eVal] = eig(full(C),full(C_dot));

    for i = 1:node_num
        lambda(i) =
eVec(:,i)'\*C*eVec(:,i)/(eVec(:,i)'\*C_dot*eVec(:,i));
    end
    lambda(Boun_index) = 0;
    dt = 0.90*2/max(lambda);
    %max(lambda) gives the critical time step size and it in this
case
    %dt is set to 0.9 of the critical time step size

    P_array(counter/check_num,:) = p;
    t_array(counter/check_num) = t;
    %nodal pressures anda current time are saved to corresponding
    %matrices

end

counter = counter +1;

end

%workspace is saved to use for post-processing
```

## APPENDIX C

---

save evolution

```
function [h] = Hfun(P)
%compaction model used in Case 3-a (see Equation (3.71))
h = (8*450/2540)*(19.42./log((1e5-P)/2.04))/1000;

function [K] = Kfun(h)
%permeability model used in Case 3-a (see Equations (3.73) and (3.74))
Vf = (8*450/2540)./h/1000;
K= 2.7314e-9*exp(-8.59*Vf);

function [dHdP] = dHdPfun(P)
%derivative of thickness with respect to pressure (see Equation (3.91))
dHdP = 8*450*19.42/2540/1000*(log((1e5-P)/2.04).^(-2))./(1e5-P);
```